

THE INFINITELY LONG YAGI ARRAY  
OF CONCENTRIC CIRCULAR LOOPS

---

A Dissertation  
Presented to  
the Faculty of the Department of Electrical Engineering  
University of Houston

---

In Partial Fulfillment  
of the Requirements for the Degree  
Doctor of Philosophy

---

By  
George Wadih Raffoul  
May, 1976

## ACKNOWLEDGEMENT

The author wishes to express his sincere appreciation to Dr. L. C. Shen for his advice and guidance. He also wants to thank the members of his committee for their constructive comments and criticism. The support of the Electrical Engineering Department and the National Science Foundation\* is gratefully acknowledged. Appreciation is also extended to Mrs. Trace Faulkner for her careful typing of the manuscript. Special thanks are due to my wife Kathleen, and daughters Alice and Julie for their constant loyalty and devotion.

---

\* Grants No. GK-32133 and ENG-74-13705

THE INFINITELY LONG YAGI ARRAY  
OF CONCENTRIC CIRCULAR LOOPS

---

An Abstract of  
A Dissertation  
Presented to  
the Faculty of the Department of Electrical Engineering  
University of Houston

---

In Partial Fulfillment  
of the Requirements for the Degree  
Doctor of Philosophy

---

By  
George Wadih Raffoul  
May, 1976

## ABSTRACT

An analysis of wave propagation on an infinitely long Yagi array of concentric circular loops is presented. A dispersion relation is derived and numerically solved for the phase velocity of the wave. For the first propagating mode, the concentric array of loops is found to possess two distinct passbands separated by a stop band. The first passband corresponds to the near resonance of the outer loop, while the second passband corresponds to the near resonance of the inner loop. The width of each of the pass- and stop- bands is a function of the ratio of radii  $b_2/b_1$ . In the first passband, the outer loop carries a minimum of five times the current on the inner loop; however, in the second passband, the current on the inner loop is at least 1.5 times that of the outer loop.

The theoretically determined phase velocities are verified by experimental measurement using the surface-wave resonator method. Also, propagation characteristics are examined in the light of measured near-field at representative frequencies throughout the pass- and stop- bands.

It is also shown that the character of wave propagation on a concentric array remains intact under an arbitrary axial displacement of inner loops relative to outer ones.

The only change appears as a phase shift in the currents of the displaced loops. This latter property may be used to achieve desired pattern shaping and/or limited beam steering of Yagi antennas.

When the outer loop is made extremely large, the concentric array reduces to an isolated array of single loops with one passband per mode. The phase velocities of the propagating waves in the latter case are used to obtain optimum design parameters for the Yagi antenna of circular loops. In the first mode of operation, the Yagi antenna of circular loops radiates mainly in the endfire direction, and in the second mode, the radiation is in a conical shell pattern. This type of antenna is well suited for coarse/fine tracking applications.

Finally, other important and varied applications of the concentric array of circular loops and variations thereof are discussed. Applications as Yagi antennas, surface waveguides, TWT interaction circuits, microwave filters, and open-structure resonators are included.

## TABLE OF CONTENTS

CHAPTER		PAGE
	INTRODUCTION . . . . .	.xiii
1	THE CIRCULAR LOOP ANTENNA . . . . .	1
	1.1 Historical Background . . . . .	1
	1.2 The Driven Circular Loop Antenna . . . . .	2
	1.3 The Parasitic Circular Loop Antenna . . . . .	8
	1.4 Far-Field Patterns of the Parasitic Loop . . . . .	9
2	OPTIMUM DESIGN OF THE YAGI ANTENNA OF CIRCULAR LOOPS . . . . .	23
	2.1 Survey of Recent Progress . . . . .	23
	2.2 The Yagi Antenna of Circular Loops: A Surface-Wave Model . . . . .	27
	2.3 Directivity and Pattern . . . . .	32
	2.4 A Need for Optimization . . . . .	36
	2.5 First Mode: Yagi Array with End-Fire Beam . . . . .	39
	2.6 Second Mode: Yagi Array with Conical- Shell Beam . . . . .	44
	2.7 Design Examples . . . . .	45
3	THE INFINITELY LONG YAGI ARRAY OF CONCENTRIC LOOPS--THEORY . . . . .	55
	3.1 Wave Propagation on Periodic Structures . . . . .	55
	3.2 Derivation of the Dispersion Relation . . . . .	59
	3.3 Numerical Evaluation of Phase Velocity . . . . .	83
	3.4 Lower Cutoff Frequencies . . . . .	91
	3.5 Analysis of the Anomalous Band . . . . .	98

## TABLE OF CONTENTS (Cont'd)

CHAPTER	PAGE
4	THE INFINITELY LONG YAGI ARRAY OF CONCENTRIC LOOPS--EXPERIMENT . . . . . 106
4.1	Experimental Objectives . . . . . 106
4.2	Description of Experimental Set-Up . . 106
4.3	Measured Phase Velocity . . . . . 113
4.4	Near-Field Measurements . . . . . 116
4.5	Dual Wave Band . . . . . 129
5	THE INFINITELY LONG YAGI ARRAY OF COAXIALLY- DISPLACED LOOPS . . . . . 149
5.1	Motivation . . . . . 149
5.2	Derivation of the Dispersion Relation . 150
5.3	Numerical Results . . . . . 161
6	DISCUSSION OF POSSIBLE APPLICATIONS . . . . 165
6.1	An Overview . . . . . 165
6.2	Areas of Possible Application . . . . . 165
7	CONCLUSION . . . . . 180
	REFERENCES . . . . . 183
	APPENDIX A . . . . . 192
	APPENDIX B . . . . . 193
	APPENDIX C . . . . . 195
	APPENDIX D . . . . . 197

## LIST OF FIGURES

FIGURE	PAGE
1.1 Circular Loop Antenna . . . . .	3
1.2 Geometry of the Circular Loop Used in the Far-Zone Calculations . . . . .	9
1.3 Three Dimensional Pattern of the Loop in the First Resonant Mode . . . . .	17
1.4 Beam and Polarization of the $1\lambda$ Loop . . .	19
1.5 Three Dimensional Pattern of the Loop in the Second Resonant Mode . . . . .	20
1.6 Beam and Polarization of the $2\lambda$ Loop . . .	21
2.1 A Yagi Array of Circular Loops . . . . .	28
2.2 Frequency Response Curves for Three Array Lengths . . . . .	28
2.3 Bandwidth and Directivity Versus Array Size for $m=1$ Mode . . . . .	43
2.4 Bandwidth and Directivity Versus Array Size for $m=2$ Mode . . . . .	49
2.5 The Angle of Maximum Radiation of a Yagi Array in the $m=2$ Mode . . . . .	50
2.6 Three Dimensional Radiation Pattern of the Array Operated at 200 MHZ . . . . .	52
2.7 Three Dimensional Radiation Pattern of the Array Operated at 430 MHZ . . . . .	53
3.1 The Yagi Array of Concentric Loops . . . . .	60
3.2 Typical Field and Source Points . . . . .	62

## LIST OF FIGURES (Cont'd)

FIGURE	PAGE
3.3 Phase Velocity of Propagating Waves on the Concentric Array ( $b_2/b_1=1.25$ ). . . . .	88
3.4 Phase Velocity of Propagating Waves on the Concentric Array ( $b_2/b_1=1.50$ ). . . . .	89
3.5 Variation of F Versus Frequency . . . . .	97
3.6 Contour Diagram Showing Phase Velocity Versus Spacing Near Cutoff of the First Band	103
3.7 Contour Diagram Showing Phase Velocity Versus Spacing Near Cutoff of the Second Band . . . . .	104
3.8 Contour Diagram Showing Phase Velocity Versus Spacing Near Cutoff of the Isolated Array . . . . .	105
4.1 Experimental Set-Up . . . . .	107
4.2 The Resonant Cavity . . . . .	109
4.3 Surface-Wave Excitor . . . . .	112
4.4 Phase Velocity of the Propagating Wave On The Isolated Array . . . . .	115
4.5 Phase Velocity of the Propagating Wave In The First and Second Passbands of the Concentric Array . . . . .	117
4.6 Measured Amplitude and Phase of Near-Field Of the Concentric Array (First Passband, $f=1.154$ GHz) . . . . .	120
4.7 Measured Amplitude and Phase of Near-Field Of The Concentric Array (First Passband, $f=1.328$ GHz) . . . . .	121

## LIST OF FIGURES (Cont'd)

FIGURE	PAGE
4.8 Measured Amplitude and Phase of Near-Field of the Concentric Array (First Passband, $f=1.358$ ) . . . . .	122
4.9 Measured Amplitude and Phase of Near-Field of the Concentric Array (Stopband, $f=2.029$ )	125
4.10 Measured Amplitude and Phase of Near-Field Of The Concentric Array (Second Passband, $f=2.070$ GHz) . . . . .	126
4.11 Measured Amplitude and Phase of Near-Field Of The Concentric Array (Second Passband, $f=2.206$ GHz) . . . . .	127
4.12 Measured Amplitude and Phase Of Near-Field Of The Concentric Array (Second Passband, $f=2.220$ GHz) . . . . .	128
4.13 Squared Difference Pattern Corresponding To Single-Wave Data . . . . .	134
4.14 Coefficient $A_1$ Pattern Corresponding To Single-Wave Data . . . . .	135
4.15 Coefficient $A_2$ Pattern Corresponding To Single-Wave Data . . . . .	136
4.16 Squared Difference Pattern Corresponding To Dual-Wave Data . . . . .	138
4.17 Measured Amplitude and Phase of Near-Field Of The Concentric Array (Second Passband, $f=2.220$ GHz) . . . . .	139
4.18 Squared Difference Pattern Corresponding To $f=2.220$ GHz) . . . . .	140

## LIST OF FIGURES (Cont'd)

FIGURE	PAGE
4.19 Measured Amplitude and Phase of Near-Field Of The Concentric Array (Second Passband, f=2.250 GHz) . . . . .	141
4.20 Squared Difference Pattern Corresponding To f=2.250 GHz) . . . . .	142
4.21 Measured Amplitude and Phase of Near-Field Of The Concentric Array (Second Passband, f=2.263 GHz) . . . . .	144
4.22 Squared Difference Pattern Corresponding To f=2.263 GHz) . . . . .	145
4.23 Measured Amplitude and Phase Of Near-Field Of The Concentric Array (Second Passband, f=2.276 GHz) . . . . .	146
4.24 Squared Difference Pattern Corresponding To f=2.276 GHz) . . . . .	147
5.1 The Yagi Array of Coaxially Displaced Loops	150
5.2 Typical Field and Source Points With Associated Distances . . . . .	152
6.1 The Open-Ring Line Structure . . . . .	169
6.2 The Helical Circuit . . . . .	173
6.3 The Ring-Bar Circuit . . . . .	174
6.4 The Ring-Loop Circuit . . . . .	176

## LIST OF TABLES

TABLE	PAGE
I Phase Delay $\phi$ In Radians Of $m=1$ Mode .	30
II Phase Delay $\phi$ In Radians Of $m=2$ Mode .	31
III Yagi Array of Loops-Design Parameters ( $m=1, d/b=1$ ) . . . . .	40
IV Yagi Array of Loops-Design Parameters ( $m=1, d/b=0.5$ ) . . . . .	41
V Yagi Array of Loops-Design Parameters ( $m=1, d/b=0.25$ ) . . . . .	42
VI Yagi Array of Loops-Design Parameters ( $m=2, d/b=0.5$ ) . . . . .	46
VII Yagi Array of Loops-Design Parameters ( $m=2, d/b=0.5$ ) . . . . .	47
VIII Yagi Array of Loops-Design Parameters ( $m=2, d/b=0.25$ ) . . . . .	48
IX Normalized Phase Velocity of $m=1$ Mode ( $a/b_1=0.01, b_2/b_1=1.25$ ) . . . . .	86
X Normalized Phase Velocity of $m=1$ Mode ( $a/b_1=0.01, b_2/b_1=1.50$ ) . . . . .	87
XI Normalized Phase Velocity of $m=1$ Mode ( $a/b_1=0.01, d/b_1=0.25, b_2/b_1=1.25, S/d=0.5$ )	163

## INTRODUCTION

Like the dipole antenna, the circular loop antenna is one of the most fundamental linear antennas in common use. Historically, small loop antennas were first investigated and used as direction finders and magnetic field detectors. It was later found that a circular loop antenna whose circumference is about one wavelength radiates strongly in the direction normal to the surface of the loop and it was employed in a Yagi-Uda endfire array.

In this study emphasis is placed on the circular loop as a parasitic element in infinitely long Yagi arrays of concentric, coaxially-displaced, and isolated arrays of circular loops. Wave propagation on these structures is investigated, and their suitability to the design of useful devices is explored.

Chapter 1 investigates the radiation characteristics of the parasitic circular loop antenna. Properties such as radiation pattern, gain, and polarization are discussed for both the  $m = 1$  and  $m = 2$  modes of operation.

Chapter 2 presents the necessary data for the optimum design of the Yagi antenna of circular loops subject to constraints on directivity, bandwidth, or

array size. A physical Yagi antenna of circular loops is found to have a linearly polarized end-fire beam in one frequency band, and a linearly polarized conical-shell beam in a second band.

Chapter 3 deals with the analysis of wave propagation on the infinitely long Yagi array of concentric loops. A dispersion relation is derived and numerically solved for the phase velocity of the propagating wave. In a given mode of operation, the Yagi array of concentric loops is found to possess two distinct pass bands separated by a stop band. A dual-wave propagation is also seen to prevail in a small portion near the end of the second passband.

The open resonator method is employed in Chapter 4 to experimentally verify the phase velocities of the propagating waves on the concentric array of circular loops. Also, the standing waves set-up within the resonant cavity are measured at various frequencies in the pass-and stop-bands by means of near-field probing of the array. Furthermore, in order to ascertain the existence or absence of dual waves, a matching technique for the near-field data at frequencies near the end of the second passband is also described.

The effect of an arbitrary axial displacement of inner loops relative to outer ones of a concentric array,

is investigated in Chapter 5. It is shown that the phase velocity of the propagating wave, and the amplitudes of loop currents remain unchanged under this transformation. In fact, the only resulting change appears as a phase shift in the currents of the displaced loops.

Finally, Chapter 6 is devoted to the discussion of potential applications of the Yagi array of concentric circular loops, and variations thereof. Applications as a Yagi antenna, surface waveguide, TWT interaction circuit, microwave filter, and open-structure resonator are treated in some detail.

## CHAPTER I

### THE CIRCULAR LOOP ANTENNA

#### 1.1 HISTORICAL BACKGROUND

The circular loop antenna driven and loaded at one or more points, has been analyzed through the years by many investigators. The methods used in these investigations vary in complexity and degree of accuracy. Appropriate to the symmetry of the circular loop, the "Fourier series" method involves a series expansion of the current in terms of the polar angle  $\phi$ . This technique, applied to the loop driven by a  $\delta$ -function generator, was first proposed by Hallen [1] and later improved by Storer [2] and perfected by Wu [3]. The theories of Storer and Wu were later extended by Iizuka to the loop with multiple loadings [4], by Fante et al. to the study of the loop near fields [5], and by King to the shunt-driven loop [6]. The "successive approximation" method of Adachi and Mushiake [7], [8] solves a modified integral equation for the current on the loop using an iterative technique. The third known method is the "numerical method" developed by Baghdasarian and Angelakos [9], which determines a solution for the integral equation given in [7] by direct numerical integration. All the remaining methods which

were used at one time or another are for the most part approximations to the Fourier series method and their validity is limited to a given loop size. Notably, the "variational" method employs a three-term cosine expansion for the current on the loop [10], and the "EMF" method uses only one term [11].

For the sake of completeness and harmony of presentation, the Fourier series method will be outlined in the next section. Interested readers are referred to Storer's and Wu's papers [2], [3] for more details. A more tutorial treatment of the subject is given by King [12].

## 1.2 THE DRIVEN CIRCULAR LOOP ANTENNA

The loop to be analyzed is illustrated in Fig. 1.1. It consists of a circular ring of perfectly conducting wire with a  $\delta$ -function generator  $V_0 \delta(\phi)$  at  $\phi=0$ . The radius of the ring is  $b$ , that of the wire  $a$ . It is assumed that the latter is very small compared with both the radius of the loop and the wavelength, so that

$$a \ll b, \quad \text{and} \quad ka \ll 1 \quad (1.1)$$

The integral equation for the current  $I(\phi)$  can be derived from the boundary condition  $E_\phi = -V_0 \delta(\phi)/b$  on the

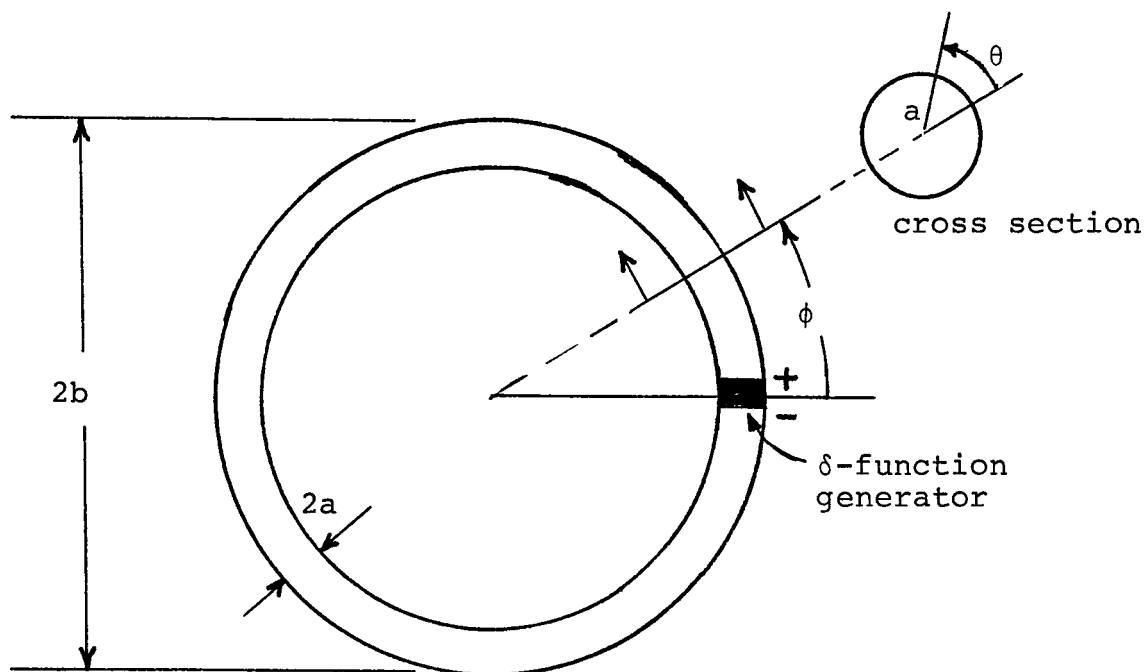


Fig. 1.1 Circular loop antenna.

surface of the loop. This requires that  $E_\phi = 0$  except at  $\phi = 0$ , where it becomes infinite but in such a manner that

$$\int_{-\pi}^{\pi} E_\phi b d\phi = -V_0 \quad (1.2)$$

It follows from the defining relation  $-\vec{E} = \nabla\phi + j\omega\vec{A}$  for the scalar potential that on the surface of the loop

$$\frac{V_0 \delta(\phi)}{b} = \frac{1}{b} \frac{\partial\phi}{\partial\phi} + j\omega A_\phi \quad (1.3)$$

The scalar and vector potentials at the element  $ds = b d\phi$  are given by the following integrals

$$\Phi = \frac{1}{4\pi\epsilon_0} \int_{-\pi}^{\pi} q(\phi') W(\phi - \phi') d\phi' \quad (1.4)$$

$$A_{\phi} = \frac{\mu_0}{4\pi} \int_{-\pi}^{\pi} I(\phi') W(\phi - \phi') \cos(\phi - \phi') d\phi' \quad (1.5)$$

where the Kernel is given by

$$W(\phi - \phi') = \frac{1}{2\pi} \int_{-\pi}^{\pi} \frac{e^{-jKbR}}{R} d\psi \quad (1.6)$$

with

$$R^2 = 4 \sin^2 \left( \frac{\phi - \phi'}{2} \right) + 4 \frac{a^2}{b^2} \sin^2 \frac{\psi}{2}$$

and  $\psi = \theta - \theta'$

where  $\mu_0$ ,  $\epsilon_0$  and  $K$  are the permeability, permittivity, and propagation constant in free space.

The total current and charge per unit length are  $I(\phi) = 2\pi a J_{\phi}(\phi)$  and  $Q(\phi) = 2\pi a \rho(\phi)$  where  $J_{\phi}(\phi)$  and  $\rho(\phi)$  are the surface densities of current and charge.

The equation of continuity may be written as

$$\frac{1}{b} \frac{\partial I(\phi)}{\partial \phi} + j\omega Q(\phi) = 0 \quad (1.7)$$

solving for  $q(\phi)$  one obtains

$$q(\phi) = \frac{j}{\omega b} \frac{\partial I(\phi)}{\partial \phi} \quad (1.8)$$

using (1.8) in the expression for  $\phi$  yields

$$\phi = \frac{j}{4\pi\epsilon_0 \omega b} \int_{-\pi}^{\pi} \frac{\partial I(\phi')}{\partial \phi'} W(\phi - \phi') d\phi' \quad (1.9)$$

By differentiating with respect to  $\phi$  and using the condition  $\frac{\partial W}{\partial \phi} = -\frac{\partial W}{\partial \phi'}$ , the following results

$$\frac{\partial \phi}{\partial \phi} = \frac{-j}{4\pi\epsilon_0 \omega b} \int_{-\pi}^{\pi} \frac{\partial I(\phi')}{\partial \phi'} \frac{\partial}{\partial \phi'} W(\phi - \phi') d\phi' \quad (1.10)$$

Integrating the right-hand side of (1.10) by parts and making use of the fact that  $I(\pi) = I(-\pi)$  yields

$$\frac{\partial \phi}{\partial \phi} = \frac{j}{4\pi\epsilon_0 \omega b} \int_{-\pi}^{\pi} I(\phi') \frac{\partial^2}{\partial \phi'^2} W(\phi - \phi') d\phi' \quad (1.11)$$

and upon substituting (1.11) and (1.5) in (1.3) it follows that

$$\begin{aligned} V_{\phi} \delta(\phi) &= \frac{j\omega\mu_0 b}{4\pi} \int_{-\pi}^{\pi} I(\phi') \cos(\phi - \phi') W(\phi - \phi') d\phi' \\ &+ \frac{j}{4\pi\epsilon_0 \omega b} \int_{-\pi}^{\pi} I(\phi') \frac{\partial^2}{\partial \phi'^2} W(\phi - \phi') d\phi' \end{aligned} \quad (1.12)$$

This may be written as

$$V_o \delta(\phi) = \frac{j\eta_o}{4\pi} \int_{-\pi}^{\pi} M(\phi-\phi') I(\phi') d\phi' \quad (1.13)$$

where the new Kernel is

$$M(\phi-\phi') = [Kb \cos(\phi-\phi') + \frac{1}{Kb} \frac{\partial^2}{\partial \phi^2}] W(\phi-\phi') \quad (1.14)$$

and  $\eta_o = \omega\mu_o/K = (\mu_o/\epsilon_o)^{1/2}$  is the intrinsic impedance of free space.

A solution of the integral equation (1.13) is now obtained in the form of a series expansion. This is derived by expanding both the Kernel  $W(\phi-\phi')$  and the current  $I(\phi')$  in Fourier series. Thus, let

$$W(\phi-\phi') = \sum_{m=-\infty}^{+\infty} K_m e^{-jm(\phi-\phi')} \quad (1.15)$$

$$I(\phi') = \sum_{n=-\infty}^{+\infty} I_n e^{-jn\phi'} \quad (1.16)$$

where the coefficients  $K_m$  and  $I_n$  are given by

$$I_n = \frac{1}{2\pi} \int_{-\pi}^{\pi} I(\phi') e^{jn\phi'} d\phi' \quad (1.17)$$

$$K_n = \frac{1}{2\pi} \int_{-\pi}^{\pi} W(\phi-\phi') e^{jn(\phi-\phi')} d\phi = K_{-n} \quad (1.18)$$

The substitution of (1.15) in (1.14) leads to the following result

$$M(\phi - \phi') = \sum_n \left[ \frac{Kb}{2} (K_{n+1} + K_{n-1}) - \frac{n^2}{Kb} K_n \right] e^{-jn(\phi - \phi')} \quad (1.19)$$

which may be written in the compact form

$$M(\phi - \phi') = \sum_{n=-\infty}^{+\infty} a_n e^{-jn(\phi - \phi')} \quad (1.20)$$

where

$$a_n = \frac{Kb}{2} [K_{n+1} + K_{n-1}] - \frac{n^2}{Kb} K_n = a_{-n} \quad (1.21)$$

On substituting (1.20) in (1.13),  $I(\phi')$  by its series representation, and evaluating the coefficients  $I_n$  by the usual methods, one obtains the result

$$I_n = \frac{-jV_o}{\eta_o \pi a_n} \quad (1.22)$$

The series solution for the loop current is now given by

$$I(\phi) = \frac{-jV_o}{\eta_o \pi} \left( \frac{1}{a_o} + 2 \sum_{n=1}^{\infty} \frac{\cos n\phi}{a_n} \right) \quad (1.23)$$

The associated input admittance is

$$Y = \frac{I(0)}{V_o} = \frac{-j}{\eta_o \pi} \left( \frac{1}{a_o} + 2 \sum_{n=1}^{\infty} \frac{1}{a_n} \right) \quad (1.24)$$

### 1.3 THE PARASITIC CIRCULAR LOOP ANTENNA

The research described throughout this dissertation focuses on the circular loops as parasitic elements excited by a traveling wave that propagates on the infinitely long Yagi structure, and not as independently driven antennas. By virtue of symmetry, the propagating modes on such a structure will be independently excited. This fact was predicted by Sensiper [13] as early as 1955 in his comments on the tape ring structure; however, it was never theoretically investigated until recently [14], [15]. This behavior results from the orthogonality property of the sinusoidal functions hereby designated as the "orthogonality property" of modes. It should be pointed out, however, that this phenomenon occurs only in the case of the infinitely long Yagi array of short-circuited loops. If, for instance, the loops are loaded at one or more points or open-circuited ( $Z_L = \infty$ ), the modal picture changes and the independent excitation of modes no longer holds.

For the purposes of this chapter, later studies will show that a mode  $m$  can be excited on the infinitely long Yagi array of circular loops. Thus, the current on any element of the array is assumed to be

$$I(\phi) = \cos m\phi; \quad m=1,2,3,\dots \quad (1.25)$$

where the amplitude has been arbitrarily normalized to unity.

#### 1.4 FAR-FIELD PATTERNS OF THE PARASITIC LOOP

In this section, the calculation of the far-zone fields of the parasitic circular loop antenna is considered. Such an antenna is shown in Fig. 1.2.

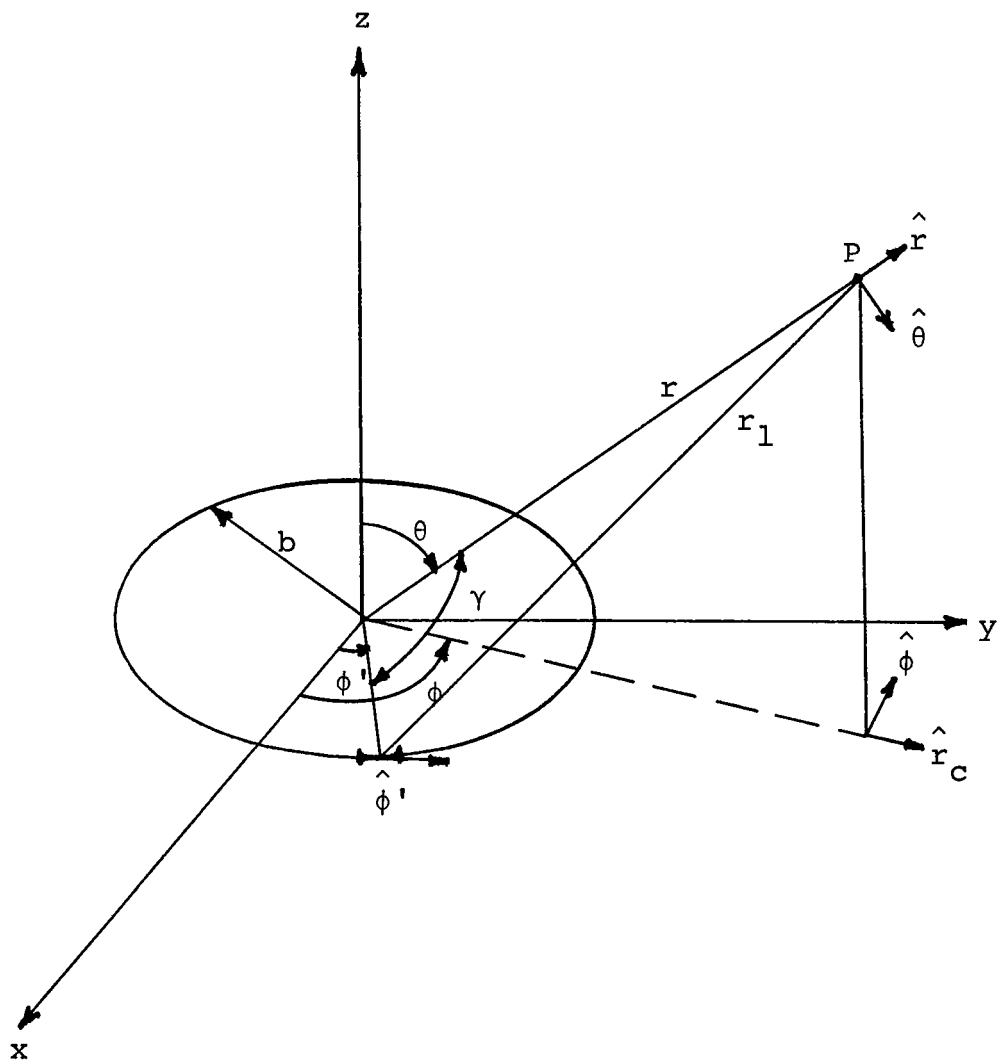


Fig. 1.2. Geometry of the circular loop used in the far-zone calculations.

The vector potential at the point P due to the current  $I(\phi)$  is given by

$$\vec{A} = \frac{\mu_0}{4\pi} \int_0^{2\pi} \frac{I(\phi') b d\phi' e^{-jKr_1} \hat{\phi}'}{r_1} \quad (1.26)$$

where  $\hat{\phi}' = \cos(\phi - \phi') \hat{\phi} + \sin(\phi - \phi') \hat{r}_c$  is a unit vector in the direction of the current element  $b d\phi'$ . And,  $\hat{r}_c = \sin\theta \hat{r} + \cos\theta \hat{\theta}$  is a unit vector in the direction shown. The distance  $r_1$  from the current element  $b d\phi'$  to the field point P is given by

$$r_1^2 = r^2 + b^2 - 2rb \cos\gamma \quad (1.27)$$

since  $b \ll r$  then

$$r_1 \approx r - b \cos\gamma = r - b \sin\theta \cos(\phi - \phi') \quad (1.28)$$

Using the expression for the unit vector  $\hat{\phi}'$  and that of the distance  $r_1$  in (1.26), the vector potential separates into its three spherical components given as

$$A_\phi = \frac{\mu_0 b}{4\pi} \frac{e^{-jKr}}{r} \int_0^{2\pi} d\phi' \cos m\phi' \cos(\phi - \phi') e^{jKb \sin\theta \cos(\phi - \phi')} \quad (1.29a)$$

$$A_{\theta} = \frac{\mu_0 b \cos \theta}{4\pi} \frac{e^{-jKr}}{r} \int_0^{2\pi} d\phi' \cos m\phi' \sin(\phi-\phi') e^{jKb \sin\theta \cos(\phi-\phi')} \quad (1.29b)$$

$$A_r = \frac{\mu_0 b \sin \theta}{4\pi} \frac{e^{-jKr}}{r} \int_0^{2\pi} d\phi' \cos m\phi' \sin(\phi-\phi') e^{jKb \sin\theta \cos(\phi-\phi')} \quad (1.29c)$$

where  $I(\phi')$  was replaced by  $\cos m\phi'$ . ( $\mu_0$  is the permeability of free space and  $K = \omega\sqrt{\mu_0\epsilon_0}$  is the propagation constant in free space.)

In the far zone, the electric field is given by

$$\vec{E} = -j\omega\vec{A}_t \quad (1.30)$$

where  $\vec{A}_t$  denotes the transverse component of the vector potential. Then,

$$\vec{E} = -j\omega(A_{\theta}\hat{\theta} + A_{\phi}\hat{\phi}) \quad (1.31)$$

Hence, once  $A_{\theta}$  and  $A_{\phi}$  are explicitly determined, the electric field follows from (1.31). In order to simplify  $A_{\phi}$  in (1.29a), a change of variable is made first. Let  $u = \phi' - \phi$  then  $du = d\phi'$  and  $\phi' = \phi + u$ . Using this in (1.29a) the expression for  $A_{\phi}$  becomes

$$A_{\phi} = \frac{\mu_0 b}{4\pi} \frac{e^{-jKr}}{r} \int_0^{2\pi} du \cos m(\phi+u) \cos u e^{jKb \sin\theta \cos u} \quad (1.32)$$

Using the trigonometric identity  $\cos m(\phi+u) = \cos m\phi \cos mu - \sin m\phi \sin mu$ , one obtains

$$A_{\phi} = \frac{\mu_0 b e^{-jKr}}{4\pi r} \left\{ \cos m\phi \int_0^{2\pi} du \cos mu \cos u e^{jKb \sin\theta \cos u} - \sin m\phi \int_0^{2\pi} du \sin mu \cos u e^{jKb \sin\theta \cos u} \right\} \quad (1.33)$$

Using now the identities  $\cos mu \cos u = [\cos(m+1)u + \cos(m-1)u]/2$  and,  $\sin mu \cos u = [\sin(m+1)u + \sin(m-1)u]/2$ , the expression for  $A_{\phi}$  may be put in the following form

$$A_{\phi} = \frac{\mu_0 b e^{-jKr}}{8\pi r} \left\{ \cos m\phi [Q_{m+1} + Q_{m-1}] - \sin m\phi [R_{m+1} + R_{m-1}] \right\} \quad (1.34)$$

where

$$Q_m = \int_0^{2\pi} \cos mu e^{jKb \sin\theta \cos u} du \quad (1.35a)$$

and,

$$R_m = \int_0^{2\pi} \sin mu e^{jKb \sin\theta \cos u} du \quad (1.35b)$$

Note that the integrand in the expression for  $R_m$  is an odd function of the variable  $u$  which yields zero when

integrated from 0 to  $2\pi$ . Hence,  $R_m=0$  and  $A_\phi$  reduces to

$$A_\phi = \frac{\mu_0 b e^{-jKr}}{8\pi r} \cos m\phi [Q_{m+1}(\theta) + Q_{m-1}(\theta)] \quad (1.36)$$

On the other hand, the integrand in  $Q_m$  is an even function of the variable  $u$ . Then  $Q_m$  may be written as

$$Q_m = 2 \int_0^\pi \cos mu e^{jKb \sin\theta \cos u} du = 2\pi j^m J_m(Kb \sin\theta) \quad (1.37)$$

where  $J_m(x)$  is the Bessel function of the first kind of order  $m$ .

The substitution of (1.37) in (1.36) yields

$$A_\phi = \frac{\mu_0 b e^{-jKr}}{4r} j^{m+1} \cos m\phi [J_{m+1}(Kb \sin\theta) - J_{m-1}(Kb \sin\theta)] \quad (1.38)$$

If the recurrence relation  $J_{m+1}(x) - J_{m-1}(x) = -2J'_m(x)$  is used in (1.38), the final expression for  $A_\phi$  results

$$A_\phi = \frac{\mu_0 b e^{-jKr}}{2r} j^{m-1} \cos m\phi J'_m(Kb \sin\theta) \quad (1.39)$$

Let us now turn to the expression of  $A_\theta$  and perform the change of variable  $u = \phi' - \phi$  with the following result

$$A_\theta = \frac{\mu_0 b e^{-jKr}}{4\pi r} \cos\theta \int_0^{2\pi} du \cos m(\phi+u) \sin(-u) e^{jKb \sin\theta \cos u} \quad (1.40)$$

Upon using the identities:  $\cos m(\phi+u) = \cos m\phi \cos mu - \sin m\phi \sin mu$ , with  $\cos mu \sin u = [\sin(m+1)u + \sin(m-1)u]/2$ , and  $\sin mu \sin u = [\cos(m-1)u - \cos(m+1)u]/2$  coupled with the vanishing of the integral  $R_m$  (see 1.35b),  $A_\theta$  reduces to

$$A_\theta = \frac{\mu_0 b e^{-jKr}}{8\pi r} \cos\theta \sin m\phi [Q_{m-1} - Q_{m+1}] \quad (1.41)$$

where  $Q_m$  is as defined in (1.35a).

Replacing  $Q_m$  by its value from (1.37) yields the result

$$A_\theta = \frac{\mu_0 b e^{-jKr}}{8\pi r} \cos\theta \sin m\phi (2\pi j^{m-1}) [J_{m-1}(Kb \sin\theta) + J_{m+1}(Kb \sin\theta)] \quad (1.42)$$

Making use of the recurrence relation  $J_{m-1}(x) + J_{m+1}(x) = 2m J_m(x)/x$ , gives the final expression for  $A_\theta$ . Namely,

$$A_\theta = \frac{\mu_0 e^{-jKr}}{2Kr} j^{m-1} \sin m\phi \frac{\cos\theta}{\sin\theta} J_m(Kb \sin\theta) \quad (1.43)$$

The electric field components  $E_\phi = -j\omega A_\phi$  and  $E_\theta = -j\omega A_\theta$  may now be determined at once.

$$E_{\phi} = -j^m \frac{\eta_0}{2} Kb \frac{e^{-jKr}}{r} J'_m(Kb \sin\theta) \cos m\phi \quad (1.44a)$$

$$E_{\theta} = -j^m \frac{\eta_0}{2} m \frac{e^{-jKr}}{r} \frac{\cos\theta}{\sin\theta} J_m(Kb \sin\theta) \sin m\phi \quad (1.44b)$$

where  $\eta_0 = \sqrt{\mu_0/\epsilon_0}$  is the intrinsic impedance of free space. Similarly, the magnetic field components

$H_{\phi} = E_{\theta}/\eta_0$  and  $H_{\theta} = -E_{\phi}/\eta_0$  are given by

$$H_{\phi} = -j^m \frac{m}{2} \frac{e^{-jKr}}{r} \frac{\cos\theta}{\sin\theta} \sin m\phi J_m(Kb \sin\theta) \quad (1.45a)$$

$$H_{\theta} = j^m \frac{Kb}{2} \frac{e^{-jKr}}{r} \cos m\phi J'_m(Kb \sin\theta) \quad (1.45b)$$

The magnitude of the time-average Poynting vector is given by

$$P_{av} = \frac{1}{2} R_e [E_{\theta} H_{\phi}^* - E_{\phi} H_{\theta}^*] = \frac{1}{2\eta_0} [|E_{\theta}|^2 + |E_{\phi}|^2] \quad (1.46)$$

Replacing  $|E_{\theta}|$  and  $|E_{\phi}|$  by their values, squaring and rearranging yields

$$P_{av}(\theta, \phi) = \frac{\eta_0}{8r^2} \left[ \left( m \frac{\cos\theta}{\sin\theta} \sin m\phi J_m(Kb \sin\theta) \right)^2 + \left( Kb \cos m\phi J'_m(Kb \sin\theta) \right)^2 \right] \quad (1.47)$$

The total radiated power from the loop antenna is obtained by integrating the time-average Poynting vector (magnitude) over the surface of a large sphere of radius  $r$ .

$$P_{\text{rad}} = \int_0^\pi \int_0^{2\pi} P_{\text{av}}(\theta, \phi) r^2 \sin\theta \, d\theta \, d\phi \quad (1.48)$$

The integration with respect to  $\phi$  is straightforward since  $\int_0^{2\pi} \sin^2 m\phi \, d\phi = \int_0^{2\pi} \cos^2 m\phi \, d\phi = \pi$ , and only the integration with respect to  $\theta$  remains.

$$P_{\text{rad}} = \frac{\pi \eta_0}{8} \left\{ m^2 \int_0^\pi \frac{\cos^2\theta J_m^2(Kb \sin\theta)}{\sin\theta} \, d\theta + (Kb)^2 \int_0^\pi \sin\theta J_m'^2(Kb \sin\theta) \, d\theta \right\} \quad (1.49)$$

The directive gain of the loop antenna is defined as the ratio between the time-average Poynting vector (magnitude) and the average radiated power density

$$G_d(\theta, \phi) = \frac{P_{\text{av}}(\theta, \phi)}{\left( \frac{P_{\text{rad}}}{4\pi r^2} \right)} \quad (1.50)$$

Substituting  $P_{\text{av}}(\theta, \phi)$  and  $P_{\text{rad}}$  by their values, it follows that

$$G_d(\theta, \phi) = \frac{\left[ 2m \frac{\cos\theta}{\sin\theta} \sin m\phi J_m(Kb \sin\theta) \right]^2 + \left[ 2Kb \cos m\phi J_m'(Kb \sin\theta) \right]^2}{m^2 \int_0^\pi \frac{\cos^2\theta J_m^2(Kb \sin\theta)}{\sin\theta} \, d\theta + (Kb)^2 \int_0^\pi J_m'^2(Kb \sin\theta) \sin\theta \, d\theta} \quad (1.51)$$

where the integrations in the denominator of (1.59) must be evaluated numerically.

At this point, one is ready to investigate the radiation properties of the parasitic circular loop antenna. With this objective in mind, only the first two resonant modes ( $m=1,2$ ) will be considered.

(1) Case:  $m=1$

The radiation intensity defined as  $(r^2 P_{av})$  was plotted as a function of  $\theta$  and  $\phi$  by a Lehner's digital plotter with the help of a 3-D program [16]. The far-field pattern of a loop in the first resonant mode ( $Kb=1$ ) is shown in Fig. 1.3. Note the  $(\theta, \phi)$  plane forms the plane of the page while the radiation intensity is the elevation above that plane. The plot view angle ( $\gamma=30^\circ$ ) designates the angle between the observer's line of sight and the  $(\theta, \phi)$  plane. Also, before plotting, all the radiation intensity values were translated upwards by an amount equal to the absolute value of the minimum. Hence, a plot minimum, or valley, represents zero elevation.

Inspection of Fig. 1.3 reveals the existence of a peak in the radiation pattern at  $\theta$  equal to  $0^\circ$  and  $180^\circ$ , and a null at  $\theta$  equal to  $90^\circ$  for  $\phi$  equal to  $90^\circ$  and  $270^\circ$ . Hence, unlike the in-plane omnidirectional pattern of the small loop with uniform current, the pattern of the one-wave-

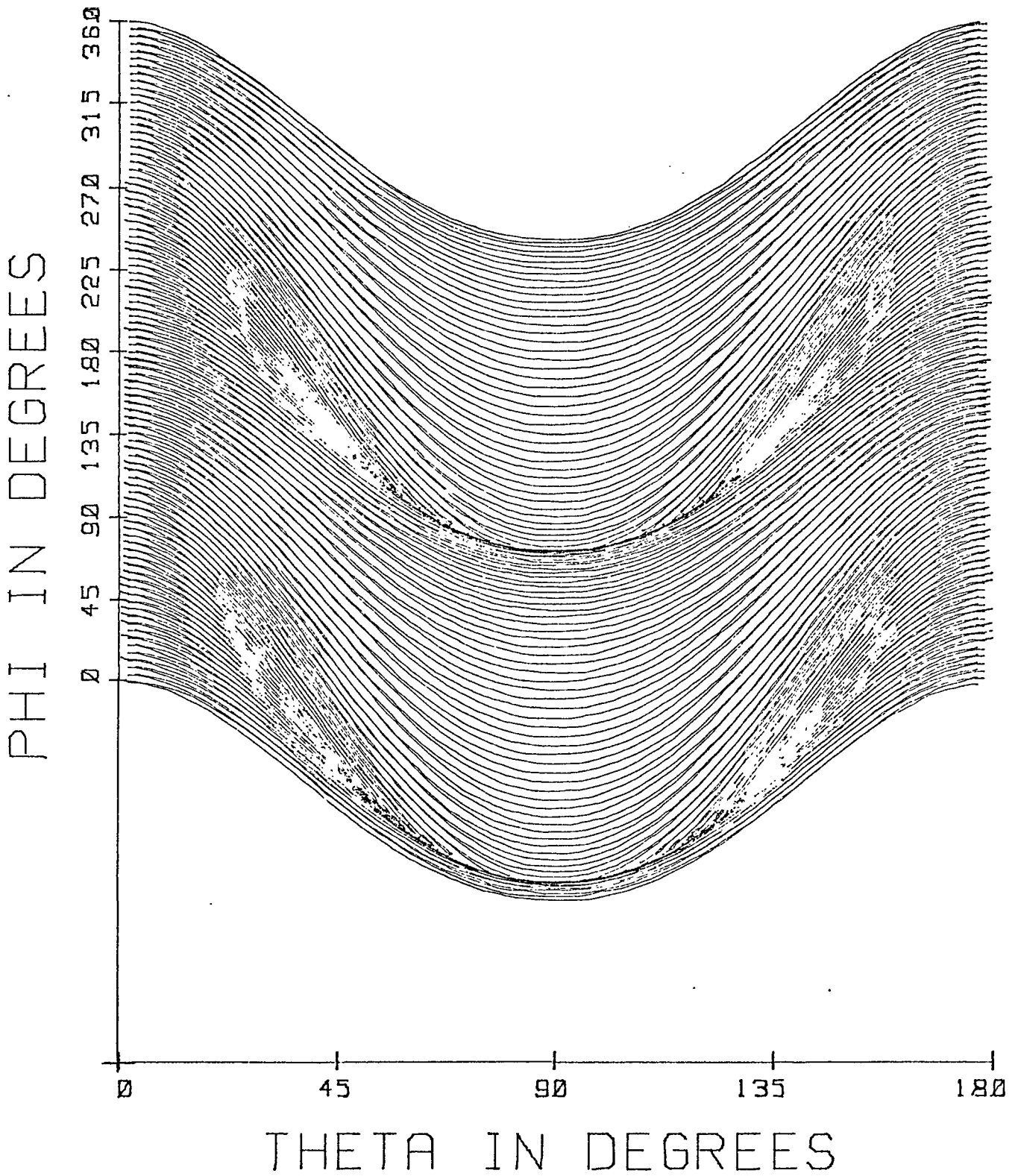


Fig. 1.3 Three dimensional pattern of the loop in the first resonant mode. ( $m=1$ ,  $K_b=1$ )

length loop is bidirectional and coincident with its axis. By evaluating the electric field in rectangular coordinates, it is easily shown that  $E_x$  vanishes at  $\theta=0^\circ$  and  $180^\circ$ . Therefore, the polarization of the antenna is linear and in the  $y$ -direction. This is illustrated schematically in Fig. 1.4. The  $E$ -field vector is parallel to an imaginary line connecting the two current nodes [17].

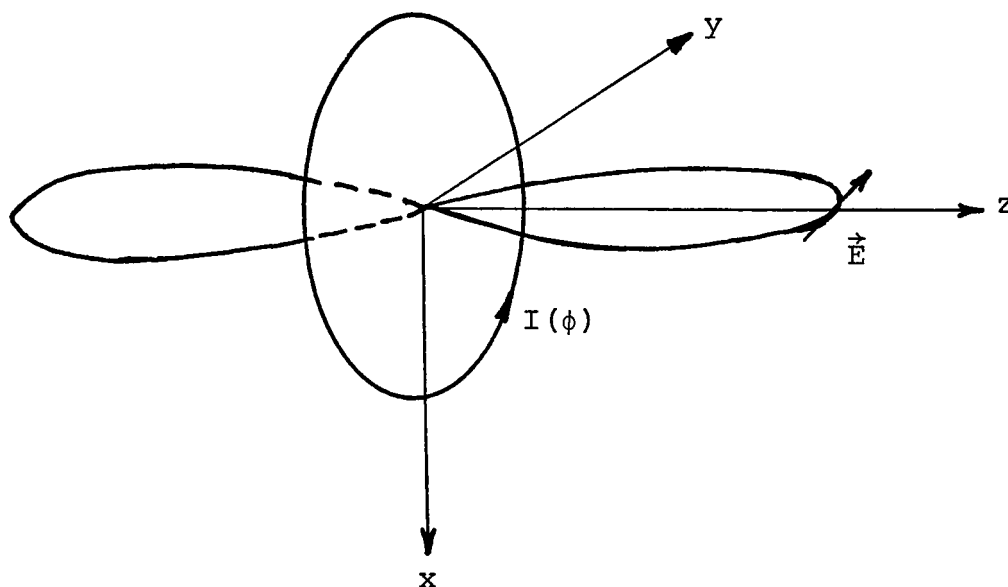


Fig. 1.4. Beam and polarization of the  $1\lambda$  loop.

It is interesting to note that the directivity of this one-wavelength antenna is approximately 4dB above isotropic or, 1.86 dB above a one-half wavelength dipole [8].

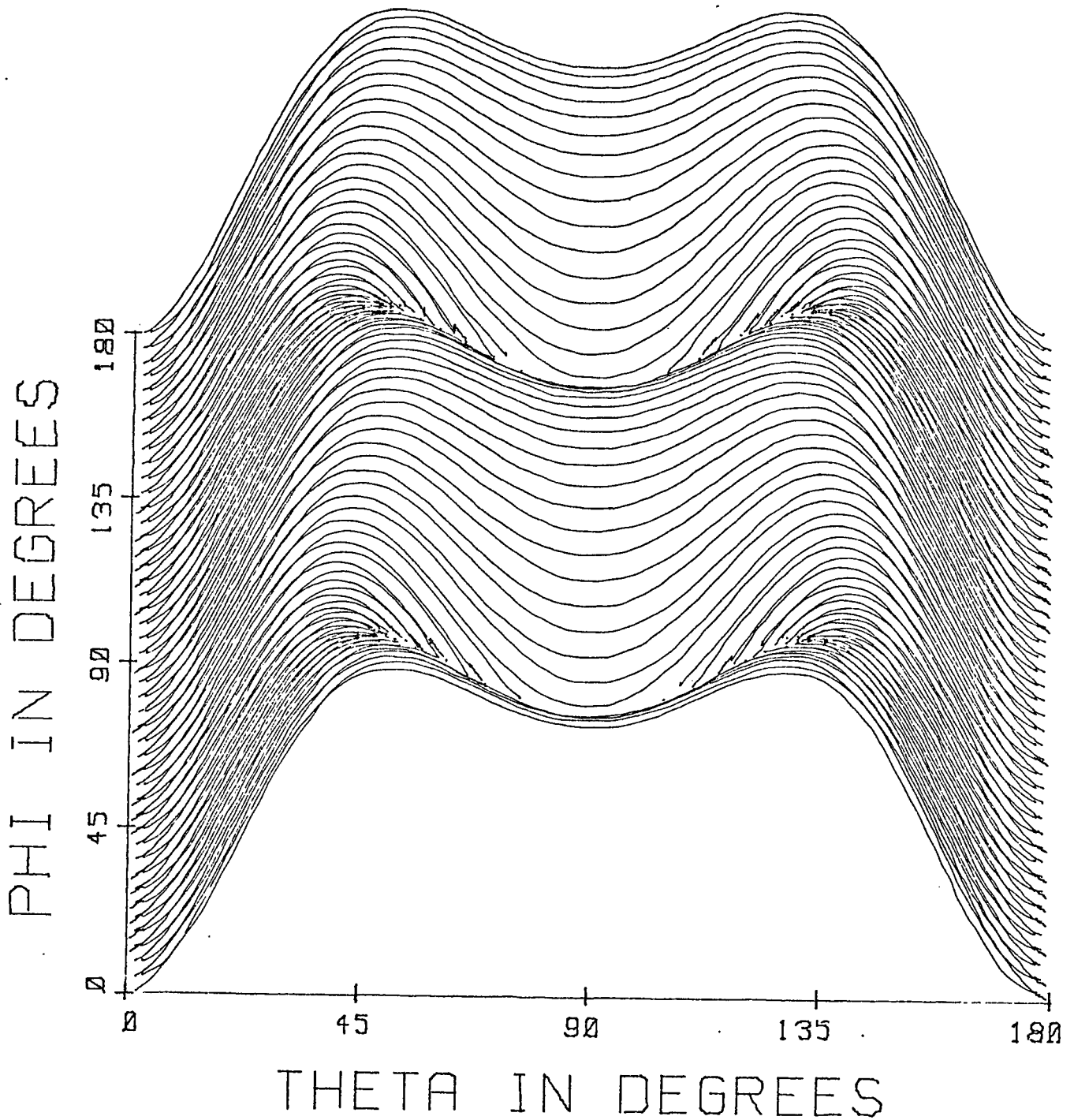


Fig. 1.5 Three-dimensional pattern of the loop in the second resonant mode. ( $m=2, K_b=2$ )

Also, since the distribution of current on the loop is in the dipole mode, the field pattern resembles that of a two-element broadside dipole array [18], however, its directivity is lower by about 1.14 dB.

(2) Case:  $m=2$

The far-field pattern of a loop in the second resonant mode ( $Kb=2$ ) is shown in Fig. 1.5. The plot view angle in this case is 45 degrees.

Inspection of Fig. 1.5 reveals the existence of a peak at  $\theta$  equal to  $45^\circ$  and  $135^\circ$  for some values of  $\phi$ , and a null at  $\theta$  equal to  $0^\circ$  and  $180^\circ$  for all values of  $\phi$ . Closer examination of pattern behavior at  $\theta=45^\circ$  and  $135^\circ$  when  $\phi$  is varied, shows a variation in the radiation intensity of no more than 3dB. Thus, the  $2\lambda$  loop has a conical-shell beam with a slightly nonuniform rose-like aperture as illustrated in Fig. 1.6.

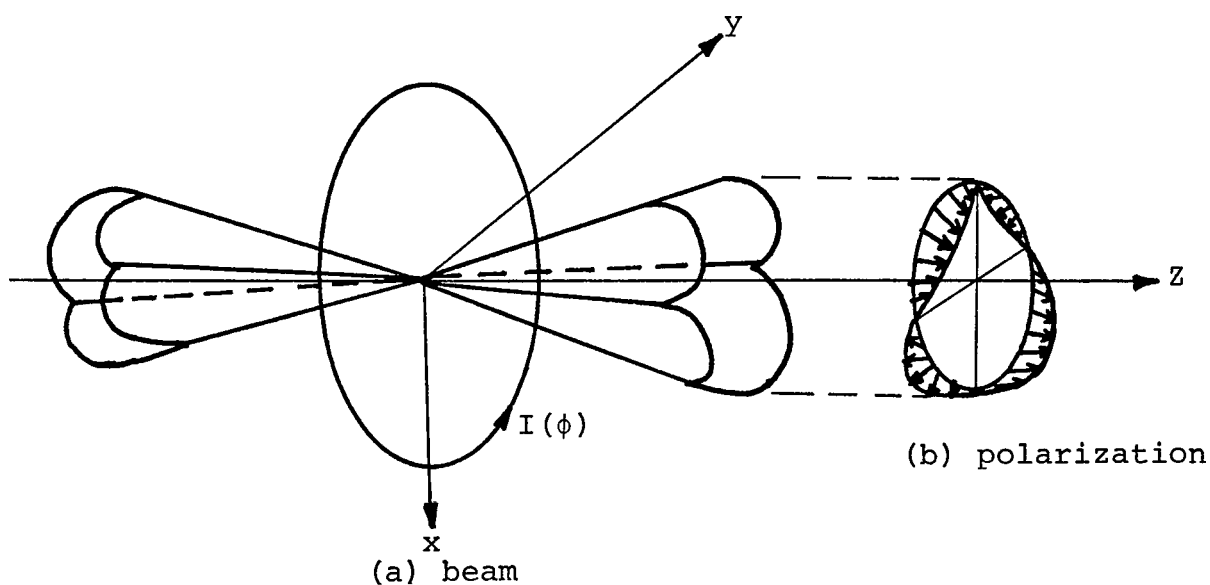


Fig. 1.6. Beam and polarization of the  $2\lambda$  loop.

The polarization in the beam is linear; however, the orientation of the E-field vector changes with  $\theta$  and  $\phi$  as one traces the circular aperture of the beam.

CHAPTER 2  
OPTIMUM DESIGN OF THE YAGI ANTENNA  
OF CIRCULAR LOOPS\*

2.1 SURVEY OF RECENT PROGRESS

Dipoles [19-39], slots [46], helices [47], and loops [14, 15, 17, 40-42, 43-44] have all been used as elements in a Yagi array. Although dipole arrays were investigated considerably in the literature, work on the loop arrays is relatively scarce by comparison. It is worthwhile to note that using loops in place of dipoles could eliminate problems of corona at high altitudes [17], and result in reduced ground reaction near the earth [45].

Ever since the discovery of the directive property of the large one-wavelength circular loop by Adachi and Mushiake (1957) [8], many investigations, mainly by Japanese researchers, were made on the use of the  $1\lambda$  loop as an element in a Yagi antenna. However, due to the analytical complexity of the loop, all of these investigations were limited to the study of two-element arrays.

---

\* Material contained in this chapter has been published in a paper by Shen & Raffoul [43].

An early study of the relatively long Yagi array of loops was an experimental one by Lindsay in 1967 [17]. Lindsay examined the pattern, gain and polarization of an array of  $l\lambda$  loops. One result, which later research did not confirm, was that the gain differential of 1.8 dB between the loop and the dipole also exists between a loop array and a dipole array of the same length. In a 1971 paper [40], Yamazawa et al. studied the propagating waves on the infinite array of tape loops. However, their analysis was lacking in several respects: (1) A uniform current was assumed to exist over the width of the tape loops; whereas, the current should actually possess a square-root singularity at the edges. (2) Cutoff was defined to occur when the interelement phase shift reaches a value equal to  $\Pi$  radians. This assumption is not valid in general as we shall show in section 3.5. (3) Only the first mode passband was discovered. (4) The orthogonality property of modes was not observed. At about the same time, Ito et al. performed a theoretical study of the finite array of loops [41]. Their study involved the use of the fourier series method with appropriate modifications to account for finite excitation gaps and unequal size loops. However, only results for 2-element Yagi arrays were obtained, This was probably due to the

numerical complexity of the matrix equations involved. Later, Appel-Hansen in an experimental paper (1972) [42], showed that the gain of a Yagi antenna depends on the velocity of the propagating wave, and not to any considerable extent on the particular forms of the director elements. After referencing Shen's work on the dipole array [30-31], Yamazawa et al. (1973) cleared up some of the shortcomings in their original paper [15]. This time they succeeded in showing the existence of various passbands and in recognizing the orthogonality property of modes. However, the remaining two defects continued to limit the accuracy and applicability of their results. About the same time, Kodis et al. in a private memorandum [14] analyzed rigorously the propagating waves on the infinite array of circular loops. Data on the phase velocity of the waves in several passbands were also given. Near cutoff and in a narrow frequency band, two propagating waves of different phase velocities were found to exist. Although the regular passbands were verified by experiment, the anomalous bands passed undetected. More will be said on this in Chapter 3. Using the phase velocity data obtained in [14], optimum design parameters for the finite array of circular loops subject to constraints on directivity, bandwidth, or array

size have been obtained. Details of this optimization strategy with numerical results are given below. Finally, the latest known publication on the subject is the one by Shoomanesh and Shafai (1975), and deals with the finite array of circular loops [44]. Calculations for a uniform array of equal size loops ( $K_b=1.0$ ) were made. In this case the  $m = 1$  mode is obviously dominant. The total current, and input admittance of the driven element, and the radiation field of the entire array, with ten Fourier coefficients taken into account, were compared to those corresponding to the dominant first mode only. The difference in both radiation field and admittance was negligible. While the first mode current is a perfect standing wave, the total current has an extra travelling wave component associated with it. This confirms the assumption made in the next section that a single dominant mode also exists on a finite Yagi array.

A short survey of recent work dealing with the large array of circular loops has been presented. The references consulted are representative of the work done and are not to be construed as exhaustive. Attention will now be focused on the main topic of this chapter: namely, a detailed discussion of the optimization procedure used in determining the physical parameters of a

finite Yagi array of circular loops constrained in bandwidth, directivity or array length.

## 2.2 THE YAGI ANTENNA OF CIRCULAR LOOPS: A SURFACE-WAVE MODEL

A Yagi array of loops is shown in Fig. 2.1, where the parameters  $a$ ,  $b$ ,  $d$ ,  $N$  and the coordinates  $r$ ,  $\theta$ ,  $\phi$  are defined. When the number of elements is infinite, it has been shown that this structure can support propagating modes in several distinct frequency bands [14]. In a given passband, a surface-wave is excited and travels unattenuated along the array. The current it induces on the elements is constant in amplitude with a progressive phase shift  $\phi$  from one element to the next. Thus, the current distribution on the typical  $n$ th loop is given by

$$I_n = \cos(m\phi)e^{-jn\phi} \quad (2.1)$$

where  $m$  is the mode number and the amplitude has been arbitrarily normalized to unity.

A Yagi antenna may be modeled as a finite section of the infinitely long structure where one end is driven by a source and the other end is terminated in free space. Also, in order to keep the model simple, certain assumptions are made. First, the current on the loops is assumed

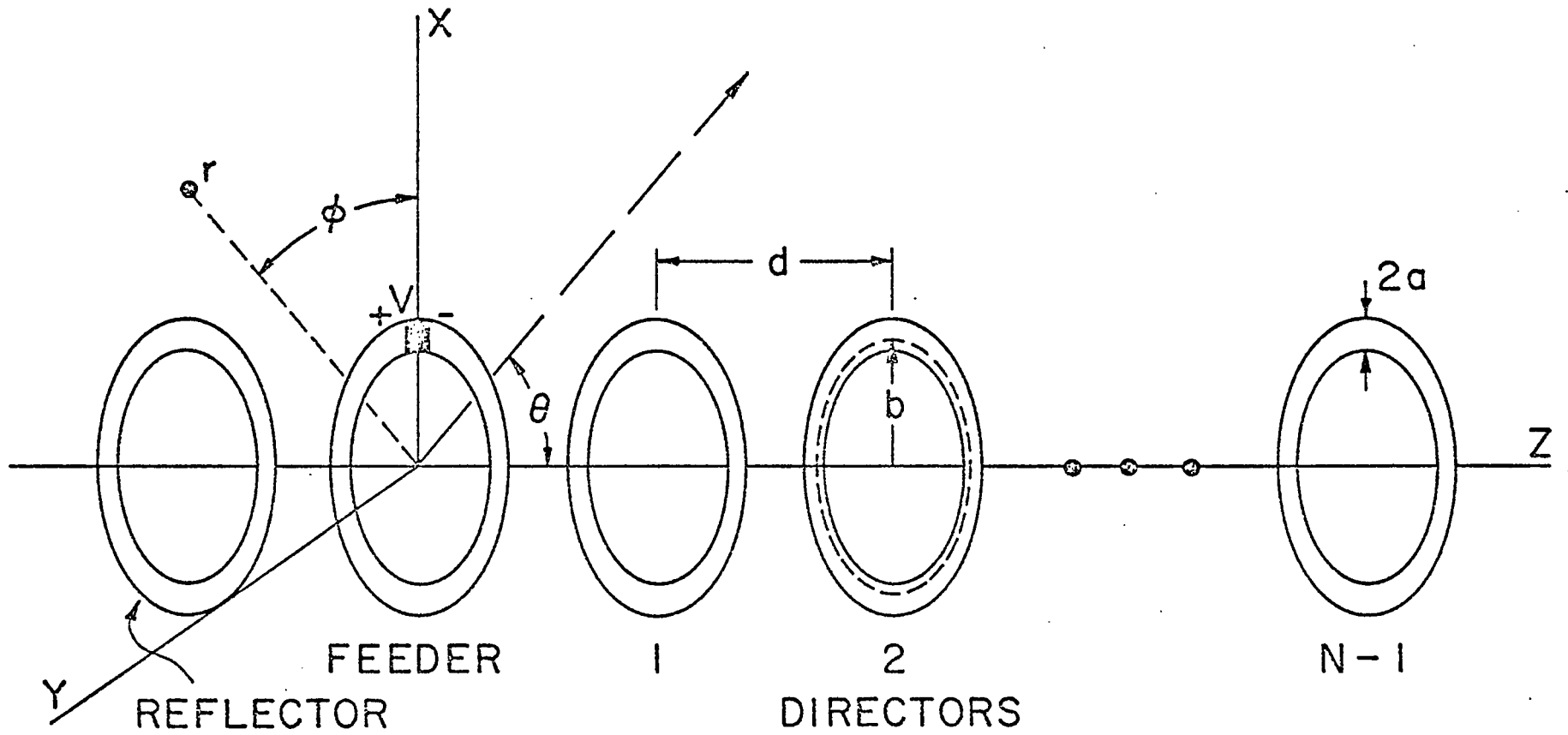


Fig. 2.1. A Yagi array of circular loops.

to have the same distribution as the current that exists on the loops of the infinitely long array (Eq. 2.1). In other words, the effect of reflection at the array ends is neglected. Second, it is assumed that the reflector loop contributes negligible radiation; therefore, its presence is ignored in the computations. The first assumption follows the same approximation procedure used in an earlier work which yielded quite satisfactory results [32]. And, the validity of the second assumption is discussed in [19].

Using the model thus formed, the far-field and directivity of the Yagi antenna may now be calculated. The phase delay  $\phi$  in equation (2.1) is first obtained, for various loop radii and spacings, from the phase velocity data given in [14] where  $\phi = (Kb)(d/b)/(v/c)$ . Also, before any pattern or gain calculations are made, the passband is limited on the low end by the requirement that the transverse power density ( $\alpha e^{-2\sqrt{\beta^2 - K^2}r}$ ) should decay as fast as  $e^{-r/2b}$ . This condition is necessary in order to limit the extent of the field in the direction normal to the array. (Note  $\phi = \beta d$  where  $\beta$  is the axial propagation constant of the wave). The phase delays corresponding to frequencies in the permissible range of the first and second passbands are given in Tables I and II respectively.

TABLE I

Phase delay  $\phi$  in radians of  $m=1$  mode ( $a/b=0.01$ )

Kb	d/b=1.0	d/b=0.5	d/b=0.25
.76			.202
.77			.207
.78		.411	.211
.79		.419	.215
.80		.427	.220
.81		.436	.224
.82		.445	.229
.83	.871	.455	.234
.84	.888	.465	.240
.85	.904	.475	.245
.86	.924	.486	.251
.87	.944	.498	.260
.88	.965	.510	.264
.89	.987	.524	.272
.90	1.011	.539	.280
.91	1.038	.556	.291
.92	1.069	.573	.298
.93	1.103	.592	.309
.94	1.142	.615	.320
.95	1.189	.642	.334
.96	1.245	.671	.352
.97	1.313	.709	.365
.98	1.404	.756	.393
.99	1.540	.822	.422
.995	1.639	.868	.443
1.000	1.783	.933	.469

TABLE II

Phase delay  $\phi$  in radians of  $m=2$  mode ( $a/b=0.01$ )

Kb	$d/b=1.0$	$d/b=0.5$	$d/b=0.25$
1.81			.458
1.82			.463
1.83			.468
1.84			.475
1.85		.933	.483
1.86		.945	.491
1.87		.958	.499
1.88		.973	.508
1.89		.990	.518
1.90		1.007	.529
1.91	1.927	1.029	.542
1.92	1.959	1.053	.556
1.93	1.998	1.078	.572
1.94	2.044	1.112	.589
1.95	2.104	1.148	.611
1.96	2.178	1.197	.636
1.97	2.280	1.256	.668
1.98	2.429	1.340	.711
1.99	2.689	1.465	.773

### 2.3 DIRECTIVITY AND PATTERN

The far zone electric field of the linear array shown in Fig. 2.1 may be obtained by applying the principle of pattern multiplication. This simply states that for an array consisting of identical radiators of like orientations, the radiated electric field is equal to the product of the normalized "element pattern" and the "array factor" [48]. The normalized "element pattern" is the electric field due to only one element of the array with a unity excitation current. The "array factor" of a linear array is the electric field intensity arising from a similar array of isotropic radiators having the same spatial positions and excitation currents as the elements comprising the original array.

The array factor for the  $N$  equally spaced elements of Fig. 2.1 is given by

$$AF = \sum_{n=0}^{N-1} e^{jn(Kd \cos \theta - \phi)} \quad (2.2)$$

where  $K = 2\pi/\lambda$  is the free space wavenumber,  $d$  is the interelement spacing, and  $\theta$  is the angle from forward endfire. The array factor may also be written as

$$AF(\psi) = \sum_{n=0}^{N-1} e^{jn\psi} \quad (2.3)$$

where  $\psi = Kd \cos \theta - \phi$ . The intensity of the electric field radiated by the array is equal to the product of the array factor,  $AF(\psi)$ , and the normalized element pattern,  $\vec{F}$ .

$$\vec{E} = \vec{F}(AF) \quad (2.4)$$

where  $\vec{F}$  was calculated in Chapter I and given by

$$\vec{F} = -j^m \frac{\eta_0}{2} \frac{e^{-jKr}}{r} \left[ m \frac{\cos \theta}{\sin \theta} J_m(Kb \sin \theta) \sin m\phi \hat{\theta} + Kb J'_m(Kb \sin \theta) \cos m\phi \hat{\phi} \right] \quad (2.5)$$

where  $\eta_0$  is the intrinsic impedance of free space,  $J_m$  is the Bessel function of order  $m$ , and  $J'_m$  is its derivative with respect to the argument. The components of the electric field intensity may be written as

$$E_\theta = -j^m \frac{\eta_0}{2} \frac{e^{-jKr}}{r} m \frac{\cos \theta}{\sin \theta} J_m(Kb \sin \theta) \sin m\phi [AF] \quad (2.6a)$$

$$E_\phi = -j^m \frac{\eta_0}{2} \frac{e^{-jKr}}{r} Kb J'_m(Kb \sin \theta) \cos m\phi [AF] \quad (2.6b)$$

The series in (2.3) is the geometric series which may be written in closed form as

$$AF(\psi) = \sum_{n=0}^{N-1} e^{jn\psi} = \frac{e^{jN\psi} - 1}{e^{j\psi} - 1} = e^{j\frac{1}{2}(N-1)\psi} \frac{\sin(N\psi/2)}{\sin(\psi/2)} \quad (2.7)$$

The time-average Poynting vector (magnitude) is given by

$$P_{av.} = \frac{1}{2\eta_0} [ |E_\theta|^2 + |E_\phi|^2 ] \quad (2.8)$$

Using (2.6) and (2.7) in (2.8) yields the result

$$P_{av}(\theta, \phi) = \frac{\eta_0}{8r^2} \frac{\sin^2(N\psi/2)}{\sin^2(\psi/2)} \left\{ \left[ m \frac{\cos\theta}{\sin\theta} J_m(Kb \sin\theta) \sin m\phi \right]^2 + \left[ Kb J'_m(Kb \sin\theta) \cos m\phi \right]^2 \right\} \quad (2.9)$$

The total radiated power is obtained by integrating  $P_{av}(\theta, \phi)$  over the surface of a large sphere of radius  $r$ . The integration with respect to  $\phi$  is straightforward, while the integration with respect to  $\theta$  remains.

$$P_{rad} = \frac{\pi\eta_0}{8} \left\{ \int_0^\pi \left[ m \frac{\cos\theta}{\sin\theta} J_m(Kb \sin\theta) \frac{\sin(N\psi/2)}{\sin(\psi/2)} \right]^2 \sin\theta d\theta + \int_0^\pi \left[ Kb J'_m(Kb \sin\theta) \frac{\sin(N\psi/2)}{\sin(\psi/2)} \right]^2 \sin\theta d\theta \right\} \quad (2.10)$$

Performing the change of variable  $y = \cos\theta$ ,  $dy = -\sin\theta d\theta$  yields the result

$$P_{\text{rad}} = \frac{\pi \eta_0}{8} [F_1(m) + F_2(m) + F_3(m) + F_4(m)] \quad (2.11)$$

where

$$F_1(m) = \int_0^1 \left[ m \frac{y}{\sqrt{1-y^2}} J_m(Kb\sqrt{1-y^2}) \frac{\sin N/2(yKd-\phi)}{\sin \frac{1}{2}(yKd-\phi)} \right]^2 dy \quad (2.12a)$$

$$F_2(m) = \int_0^1 \left[ m \frac{y}{\sqrt{1-y^2}} J_m(Kb\sqrt{1-y^2}) \frac{\sin N/2(yKd+\phi)}{\sin \frac{1}{2}(yKd+\phi)} \right]^2 dy \quad (2.12b)$$

$$F_3(m) = \int_0^1 \left[ Kb J'_m(Kb\sqrt{1-y^2}) \frac{\sin N/2(yKd-\phi)}{\sin \frac{1}{2}(yKd-\phi)} \right]^2 dy \quad (2.12c)$$

$$F_4(m) = \int_0^1 \left[ Kb J'_m(Kb\sqrt{1-y^2}) \frac{\sin N/2(yKd+\phi)}{\sin \frac{1}{2}(yKd+\phi)} \right]^2 dy \quad (2.12d)$$

The directive gain may now be evaluated from the relation  $G_d(\theta, \phi) = (4\pi r^2) (P_{\text{av}}(\theta, \phi) / P_{\text{rad}})$ . It follows that

$$G_d(\theta, \phi) = \frac{[m \cot \theta J_m(Kb \sin \theta) \sin m\phi]^2 + [Kb J'_m(Kb \sin \theta) \cos m\phi]^2}{F_1(m) + F_2(m) + F_3(m) + F_4(m)} \cdot \left[ \frac{2 \sin N/2(Kd \cos \theta - \phi)}{\sin \frac{1}{2}(Kd \cos \theta - \phi)} \right]^2 \quad (2.13)$$

Finally, the directivity of the antenna is defined as the directive gain evaluated in the direction of maximum radiation. As in Chapter I, only two cases are considered.

(1) case:  $m=1$

In this case the beam is in endfire direction ( $\theta_{\max} = \phi_{\max} = 0$ ). Using this in the numerator of (2.13) yields the directivity of the Yagi array in the first mode.

$$D_1 = \frac{(Kb)^2 [\sin N/2(Kd-\phi) / \sin \frac{1}{2}(Kd-\phi)]^2}{F_1(1) + F_2(1) + F_3(1) + F_4(1)} \quad (2.14)$$

(2) case:  $m=2$

In this case the beam is shaped like conical shell with  $\theta_{\max}$  and  $\phi_{\max}$  determined by a study of the radiation intensity  $r^2 P_{av}$  (Eq. 2.9) when  $\theta$  and  $\phi$  are varied in their respective ranges. It follows that  $\phi_{\max}=0$  while  $\theta_{\max}$  is variable and function of the parameters of the array. Then, the expression for the directivity of the Yagi array in the second mode may be written as

$$D_2 = \frac{[2 Kb J_2' (Kb \sin \theta_{\max})]^2}{F_1(2)+F_2(2)+F_3(2)+F_4(2)} \cdot \left[ \frac{\sin N/2(Kd \cos \theta_{\max} - \phi)}{\sin \frac{1}{2}(Kd \cos \theta_{\max} - \phi)} \right]^2 \quad (2.15)$$

#### 2.4 A NEED FOR OPTIMIZATION

The ideas described below apply to the Yagi array antenna when operated in either the first or the second mode. For the sake of clarity, A Yagi array operated in the first mode ( $m=1$ ) is considered. The array parameters

$N$ ,  $a/b$  and  $d/b$  have certain fixed and known values. By substituting the phase delay data of Table I in Eq. (2.14), the directivity of such an antenna may be calculated at discrete frequencies throughout the passband. The resultant gain versus frequency curve shows an almost linear increase with frequency up to a maximum value after which the gain sharply deteriorates. This is illustrated typically in Fig. 2.2 for  $a/b = 0.01$ ,  $d/b = 0.25$ , and three different values of  $N$  ( $N=24$ ,  $48$ , and  $72$ ).

The bandwidth of the array is hereby defined as the frequency range in which the gain is equal to or greater than that at the lower cutoff frequency of the passband. Inspection of Fig. 2.2 shows as much as 4 dB variation in gain from the maximum value when the frequency varies within the range covered by the bandwidth. So, in order to limit the gain variation to a minimum without a sacrifice in bandwidth, it is necessary to choose the center frequency as the nominal design frequency instead of the one corresponding to maximum gain. It is seen that this selection of operating frequency results in a slight reduction in gain from the maximum value; however, the increase in operating bandwidth more than compensates for the reduced gain.

Using these guidelines, the necessary data needed

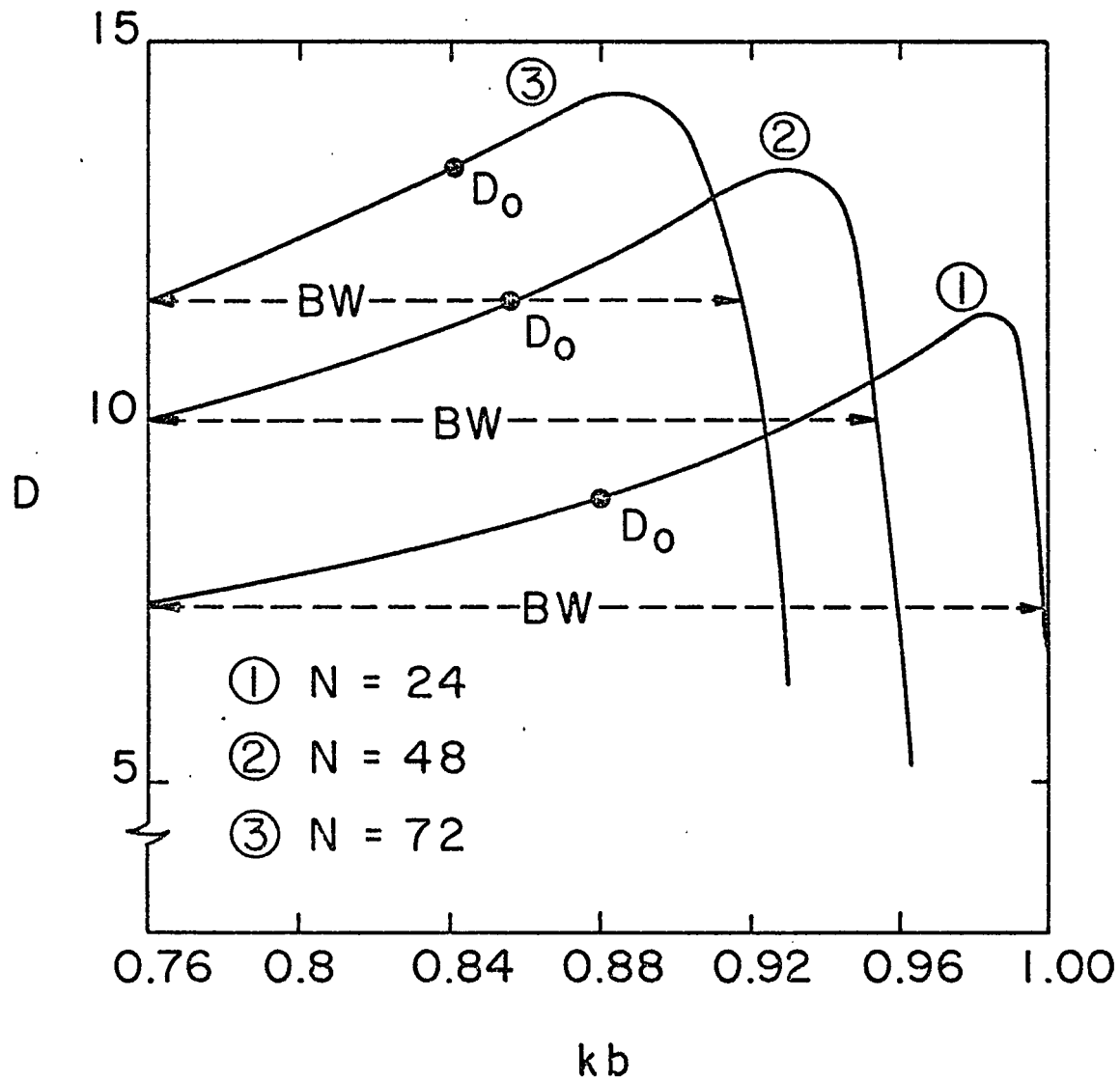


Fig. 2.2 Frequency response curves for three array lengths ( $a/b=0.01$ ,  $d/b=0.25$ )

in the design of Yagi antenna arrays constrained in either gain, bandwidth, or array size may now be obtained. It is shown that the physical structure of the Yagi antenna is completely determined whenever any two of these constraints are specified.

## 2.5 FIRST MODE: YAGI ARRAY WITH END-FIRE BEAM

Starting with a given set of array parameters ( $N$ ,  $a/b$ , and  $d/b$ ), the phase delay data of Table I are used in Eq. (2.14) to calculate values for the directivity corresponding to frequencies in the first passband. Then, the bandwidth of the array is determined in the manner explained in the previous section. The center frequency  $(Kb)_0$  and its corresponding directivity  $D_0$  are determined next. After that, the percent bandwidth and the array length are evaluated in terms of center frequency. This completes one round of calculation. Next, a new value of  $N$  is chosen and the procedure is repeated.

Tables III-V list the results of the calculations for the  $m=1$  mode. These results are also plotted in Fig. 2.3. Note that the directivity is insensitive to the spacing of the loops while the bandwidth is very much dependent on it. The calculated directivity is compared with the experimental data obtained in [42]. It should

TABLE III  
 Yagi Array of Loops - Design Parameters  
 ( $m=1, d/b=1$ )

N	kb	D (dB)	BW (%)	$L/\lambda$
6	0.92	8.6	18.6	0.73
8	0.91	9.7	17.6	1.01
10	0.91	10.6	16.6	1.30
12	0.90	11.3	15.5	1.58
14	0.90	12.1	15.5	1.86
16	0.90	12.6	14.5	2.13
18	0.90	13.2	14.5	2.42
20	0.89	13.7	13.5	2.69
22	0.89	14.1	12.4	2.96
24	0.89	14.5	12.4	3.23
26	0.88	14.9	11.4	3.50
28	0.88	15.3	11.4	3.78
30	0.88	15.5	10.3	4.03

TABLE IV  
 Yagi Array of Loops - Design Parameters  
 (m=1, d/b=0.5)

N	kb	D (dB)	BW (%)	L/ $\lambda$
12	0.89	8.7	24.7	0.78
14	0.89	9.3	24.2	0.92
16	0.88	9.7	22.7	1.05
18	0.88	10.2	22.7	1.19
20	0.88	10.6	21.7	1.32
24	0.87	11.4	20.7	1.59
28	0.87	12.0	19.7	1.86
32	0.86	12.6	18.6	2.12
36	0.86	13.1	17.5	2.38
40	0.85	13.6	16.5	2.64
44	0.85	14.0	15.4	2.89
48	0.85	14.5	15.4	3.16
52	0.84	14.8	14.3	3.41
56	0.84	15.0	13.2	3.65
60	0.84	15.4	13.2	3.92

TABLE V  
 Yagi Array of Loops - Design Parameters  
 (m=1, d/b=0.25)

N	kb	D (dB)	BW (%)	L/λ
24	0.88	8.7	27.3	0.81
28	0.88	9.3	26.3	0.94
32	0.87	9.9	25.3	1.07
36	0.87	10.2	24.3	1.20
40	0.87	10.8	24.3	1.34
44	0.86	11.1	23.2	1.47
48	0.86	11.5	22.2	1.60
52	0.86	11.9	22.2	1.74
56	0.85	12.2	21.2	1.86
60	0.85	12.4	20.1	1.98
64	0.85	12.7	20.1	2.12
68	0.84	13.0	19.0	2.24
72	0.84	13.3	19.0	2.37
76	0.84	13.5	18.0	2.49
80	0.83	13.6	16.9	2.61
84	0.83	13.9	16.9	2.74
88	0.83	14.2	16.9	2.87
92	0.83	14.3	15.8	2.99
96	0.83	14.5	15.8	3.12
100	0.82	14.7	14.6	3.23
104	0.82	14.9	14.6	3.36
108	0.82	15.1	14.6	3.49
112	0.82	15.1	13.5	3.60
116	0.81	15.2	12.3	3.71
120	0.81	15.4	12.3	3.84

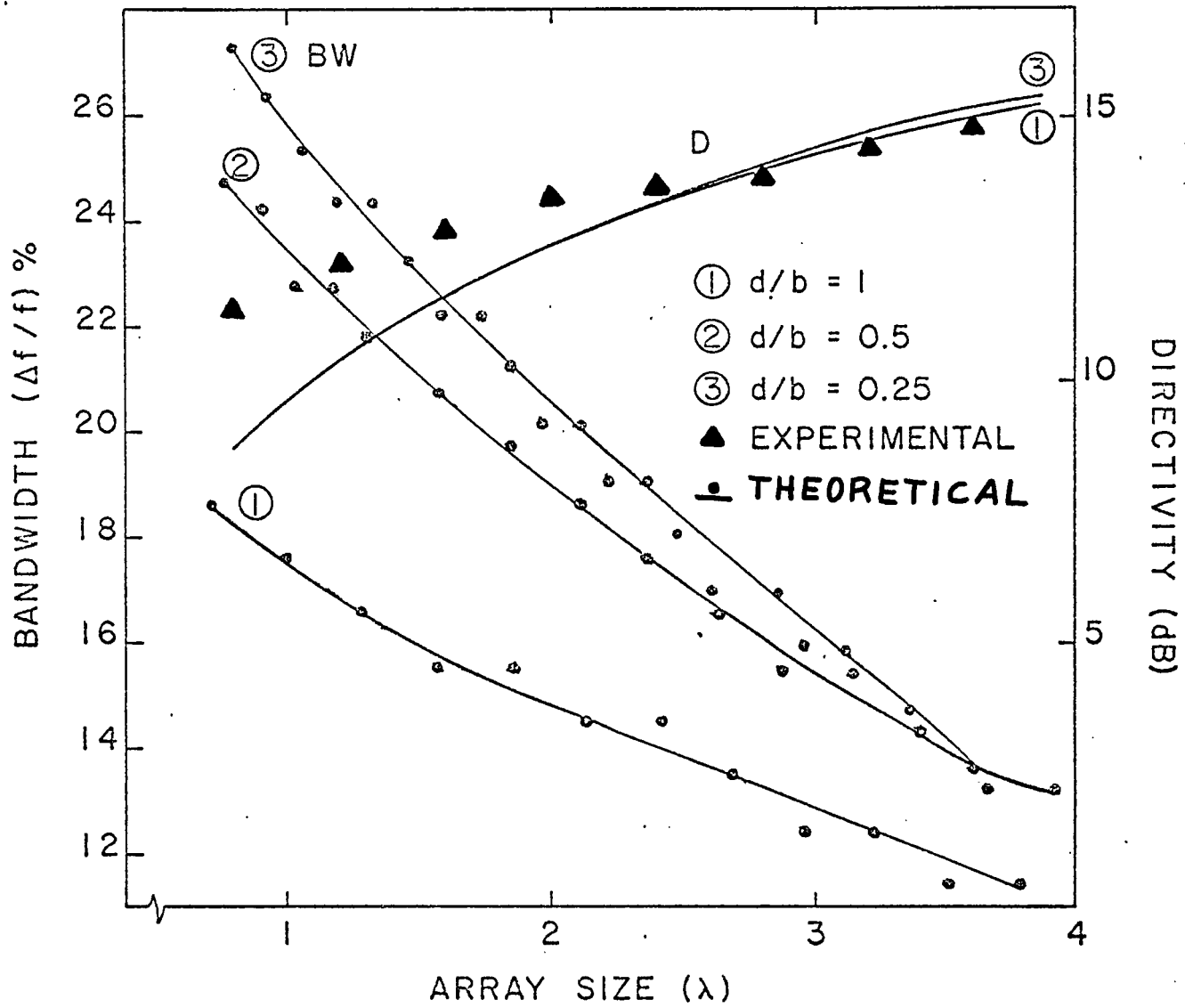


Fig. 2.3. Bandwidth and directivity versus array size for  $m=1$  mode.

be remembered that in the present analysis the directivity corresponds to the midrange frequency, while the measured one corresponds to the largest obtainable directivity as shown in Fig. 2.2. From Fig. 2,3, it is seen that the difference between the two may be as much as 2.5 dB when the array is  $0.8\lambda$  long. For longer arrays, the bandwidth is narrower and the discrepancy gradually disappears. In view of this fact, the agreement between theory and experiment is considered to be quite satisfactory.

Finally, like a dipole array, a loop array in the first mode of operation radiates mainly in the end-fire direction.

## 2.6 SECOND MODE: YAGI ARRAY WITH CONICAL-SHELL BEAM

Starting with a given set of array parameters ( $N$ ,  $a/b$ , and  $d/b$ ), the beam position  $\theta_{\max}$  is first determined. This is done by inspection of the radiation intensity (Eq. 2.9) as  $\theta$  varies throughout its range. The knowledge of the array parameters, the beam position  $\theta_{\max}$ , and the phase delays given in Table II enables one to obtain the directivity versus frequency curve by successive application of equation (2.15). The remainder of the numerical procedure is identical to that used previously for the first mode.

Tables VI-VIII list the results of the calculations for the  $m=2$  mode. These results are also plotted in Fig. 2.4. It is interesting to note that there is no radiation in the end-fire direction. In fact, the beam is shaped like a conical shell. The angle,  $\theta_{\max}$ , at which maximum radiation occurs, is plotted in Fig. 2.5. The angle  $\theta_{\max}$  and the directivity  $D$  are both functions of array size but very insensitive to the spacing between the loops. The bandwidth, on the other hand, varies between one and two percent when the spacing changes by a factor of two. On the conical surface  $\theta = \theta_{\max}$ , the radiation intensity is almost independent of  $\phi$ . The variation with  $\phi$  is greater for shorter arrays; for example, it is approximately 1.1 dB for  $L=0.9\lambda$  but reduces to less than 0.1 dB for  $L=8\lambda$ .

## 2.7 DESIGN EXAMPLES

**Example 1:** Consider the following problem. It is required to design a Yagi array of loops with length limited to 3m and an operating frequency range of  $200\pm 10$  MHz. An optimum set of parameters is to be found to yield a maximum directivity in the end-fire direction with a minimum number of elements.

**Solution:** Since the array size is  $2\lambda$  and the bandwidth

TABLE VI  
 Yagi Array of Loops - Design Parameters  
 (m=2, d/b=1.0)

N	kb	$\theta_{\max}$	D (dB)	BW (%)	L/ $\lambda$
4	1.95	35°	7.3	4.1	.91
6	1.95	30°	8.9	3.6	1.55
8	1.94	26°	9.8	3.1	2.16
10	1.94	23°	10.6	3.1	2.78
12	1.94	22°	11.1	2.6	3.40
14	1.94	20°	11.4	2.6	4.01
16	1.93	19°	11.9	2.1	4.61
18	1.93	17°	12.2	2.1	5.22
20	1.93	17°	12.5	1.6	5.84
22	1.93	16°	12.6	1.6	6.45
24	1.93	15°	12.8	1.6	7.07
26	1.93	15°	12.8	1.6	7.68
28	1.93	14°	12.9	1.6	8.29
30	1.92	14°	13.7	1.0	8.86

TABLE VII  
 Yagi Array of Loops - Design Parameters  
 (m=2, d/b=0.5)

N	kb	$\theta_{\max}$	D (dB)	BW (%)	L/ $\lambda$
6	1.93	39°	7.0	6.8	.77
8	1.92	35°	7.9	6.3	1.07
10	1.92	32°	8.6	6.3	1.38
12	1.92	29°	9.2	5.7	1.68
14	1.91	28°	9.6	5.2	1.98
16	1.91	26°	10.1	4.7	2.28
18	1.91	25°	10.4	4.7	2.58
20	1.90	24°	10.7	4.2	2.87
22	1.90	23°	10.9	4.2	3.18
24	1.90	22°	11.1	3.7	3.48
26	1.90	21°	11.3	3.7	3.78
28	1.90	20°	11.5	3.7	4.08
30	1.89	20°	11.8	3.2	4.36
34	1.89	18°	12.0	3.2	4.96
38	1.89	17°	12.2	2.7	5.57
42	1.88	17°	12.6	2.1	6.13
46	1.88	16°	12.8	2.1	6.73
50	1.88	15°	12.9	2.1	7.33
54	1.88	15°	12.9	1.6	7.93
58	1.88	14°	12.9	1.6	8.53

TABLE VIII  
 Yagi Array of Loops - Design Parameters  
 (m=2, d/b=0.25)

N	kb	$\theta_{\max}$	D (dB)	BW (%)	L/ $\lambda$
12	1.90	39°	7.0	9.5	.83
14	1.90	36°	7.5	9.0	.98
16	1.90	35°	7.9	9.0	1.13
18	1.89	33°	8.2	8.5	1.28
20	1.89	32°	8.6	8.5	1.43
22	1.89	31°	8.9	8.0	1.58
24	1.89	30°	9.2	8.0	1.73
26	1.88	28°	9.4	7.4	1.87
28	1.88	27°	9.6	7.4	2.02
30	1.88	27°	9.8	6.9	2.17
32	1.88	26°	10.0	6.9	2.32
34	1.87	25°	10.2	6.4	2.46
36	1.87	24°	10.4	6.4	2.60
38	1.87	24°	10.5	6.9	2.75
40	1.87	24°	10.7	5.9	2.90
44	1.87	22°	10.9	5.9	3.2
48	1.86	21°	11.2	5.4	3.48
52	1.86	21°	11.4	4.9	3.77
56	1.86	20°	11.5	4.9	4.07
60	1.86	19°	11.7	4.9	4.37
64	1.85	19°	11.9	4.3	4.64
68	1.85	18°	12.1	4.3	4.93
72	1.85	18°	12.2	3.8	5.23
76	1.85	18°	12.2	3.8	5.52
80	1.85	17°	12.4	3.8	5.82
84	1.85	16°	12.4	3.8	6.11
88	1.84	16°	12.7	3.3	6.37
92	1.84	16°	12.8	3.3	6.66
96	1.84	16°	12.9	3.3	6.76
100	1.84	16°	12.9	2.7	7.25

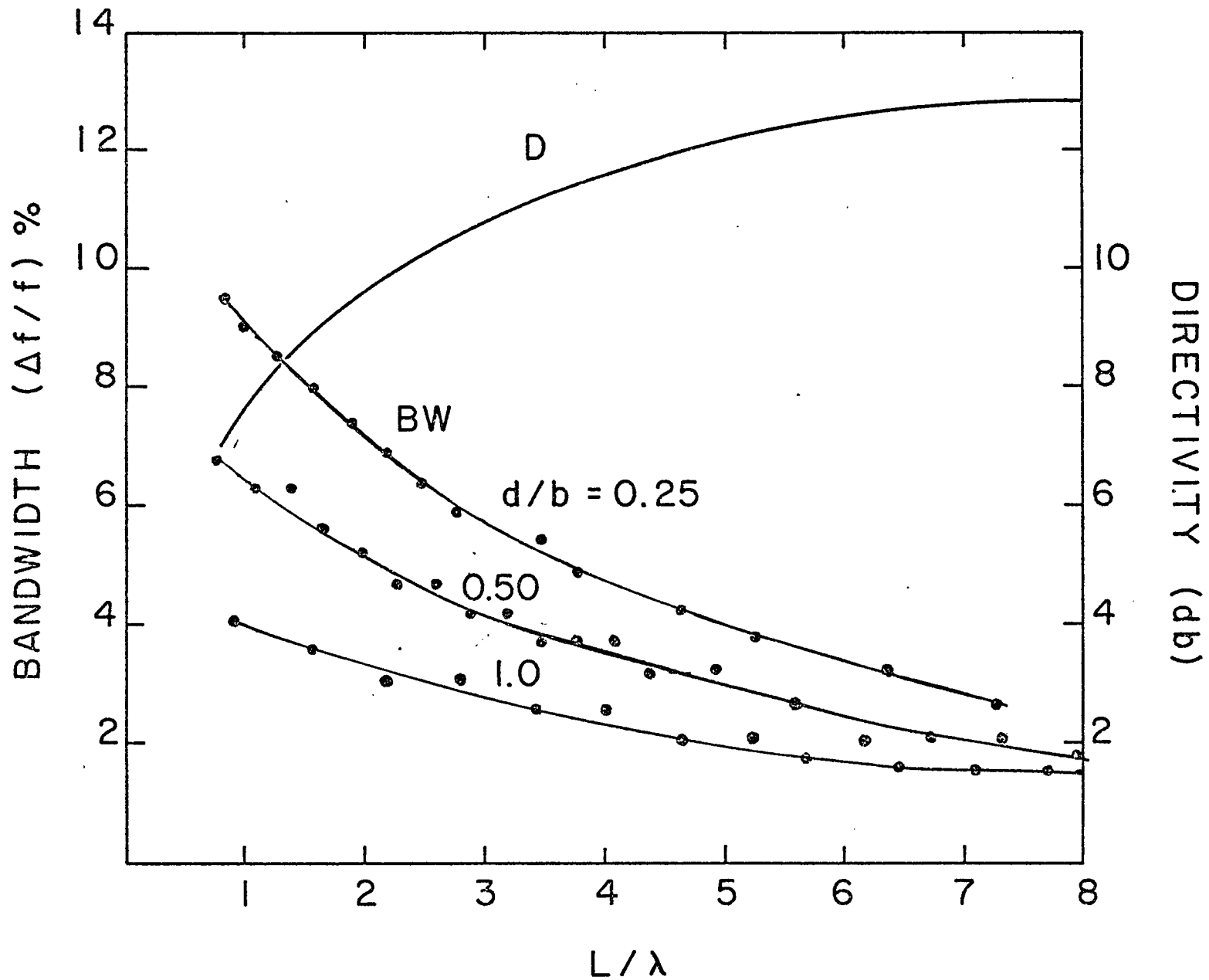


Fig. 2.4 Bandwidth and directivity versus array size for  $m=2$  mode.

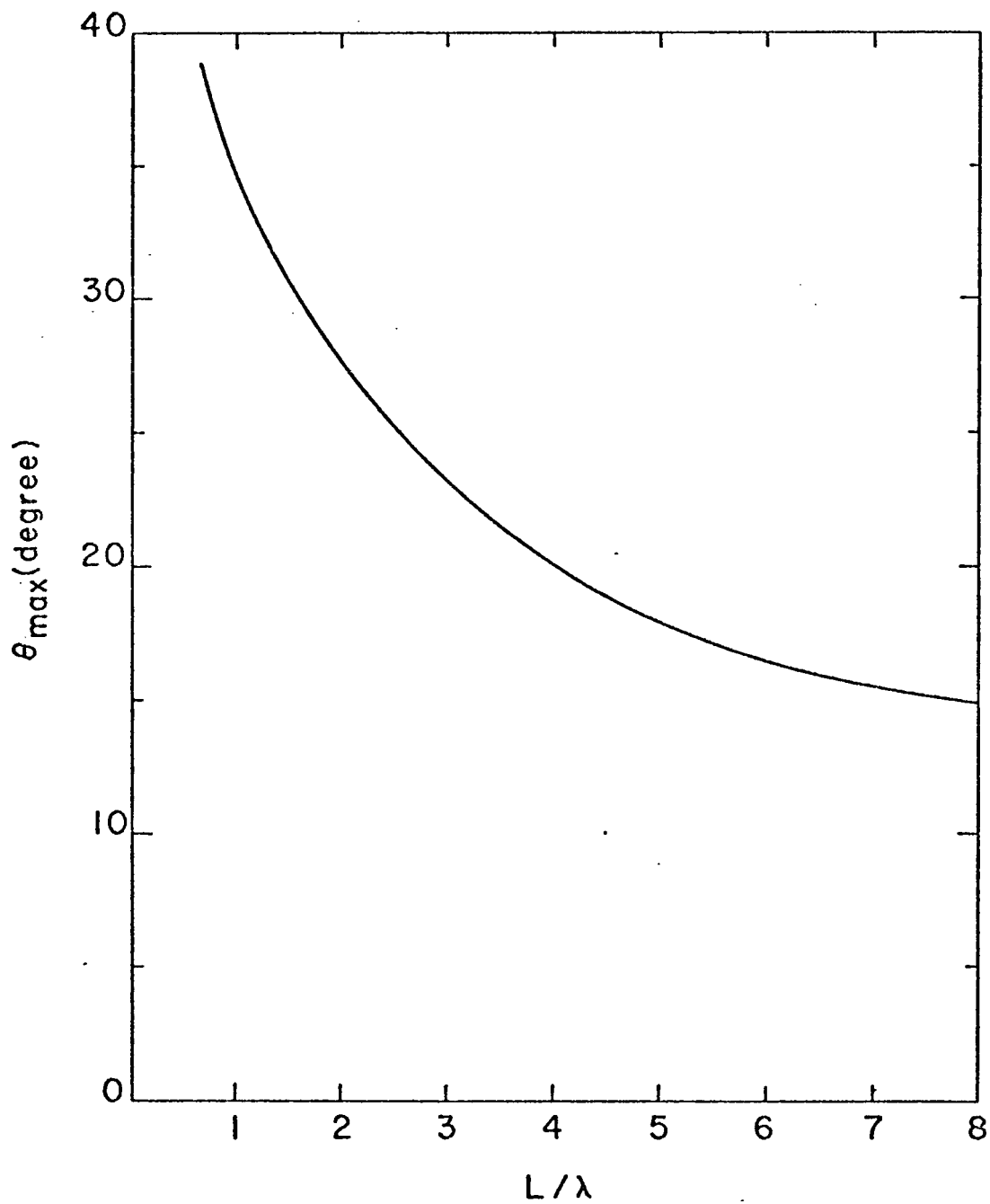


Fig. 2.5. The angle of maximum radiation of a Yagi array in the  $m=2$  mode. (valid for all spacings).

is 10%, from Fig. 2.3, it is seen that the parameter  $d/b$  may be chosen equal to 1.0. The directivity is about 12.5 dB. A more accurate result is obtained from Table III. By interpolation, it is found that  $N=15$ ,  $K_b=0.90$ ,  $D=12.35$  dB,  $BW=15\%$  and  $L=1.995\lambda$ . In terms of physical parameters,  $a=0.00215m$ ,  $b=0.215m$ ,  $d=0.215m$ , and  $L=2.993m$ . The array has one reflector, one feeder, and 14 directors. The array radiates in the end-fire direction. A three-dimensional plot of the field pattern of this array is shown in Fig. 2.6.

Example 2: Consider the following design problem. Suppose that it is required to design a Yagi array of loops subject to the conditions set in Example 1. Furthermore, it is to be operated at another frequency that is roughly twice that of the fundamental frequency of Example 1. Find the second frequency range that the array may be operated in, the directivity, and the shape of the radiated beam.

Solution: According to the result obtained in the first example,  $N=15$  and  $d/b=1.0$ . Using Table VI, it is found that the corresponding  $K_b$  is 1.935,  $\theta_{\max}=19.5^\circ$ ,  $D=11.65$  dB, and  $BW=2.35\%$ . In other words, the array is operable at a new center frequency of 430 MHz with a range of  $\pm 5.05$  MHz having a conical shell beam with  $\theta_{\max}=19.5^\circ$ . A three-dimensional plot of the field pattern of this array is shown in Fig. 2.7.

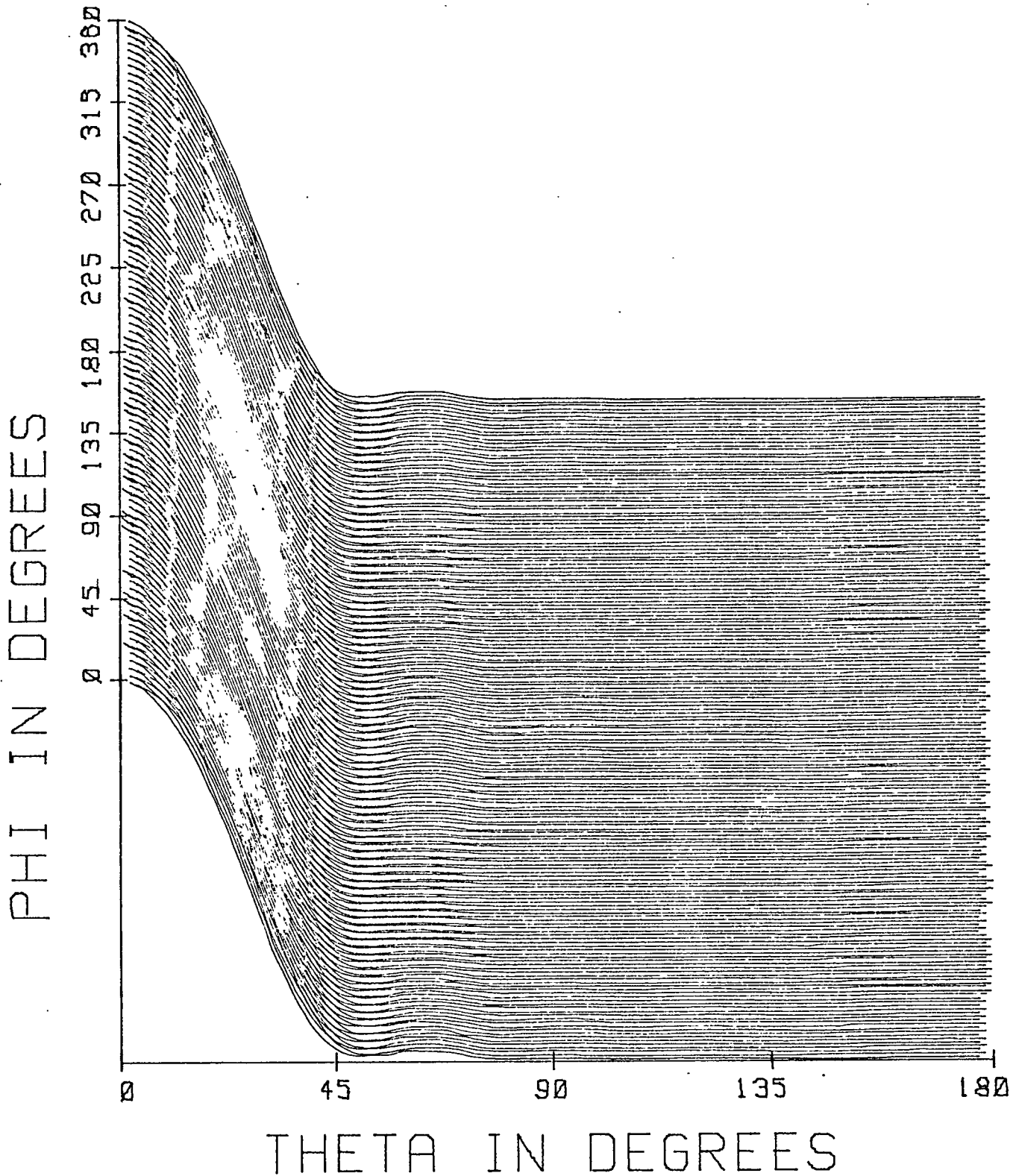


Fig. 2.6 Three-dimensional radiation pattern of the array with  $a=0.00215$  m,  $b=0.215$  m,  $d=0.215$  m, and  $L=2.993$  m,  $N=15$ ,  $D=12.35$  dB, operated at 200 MHz.

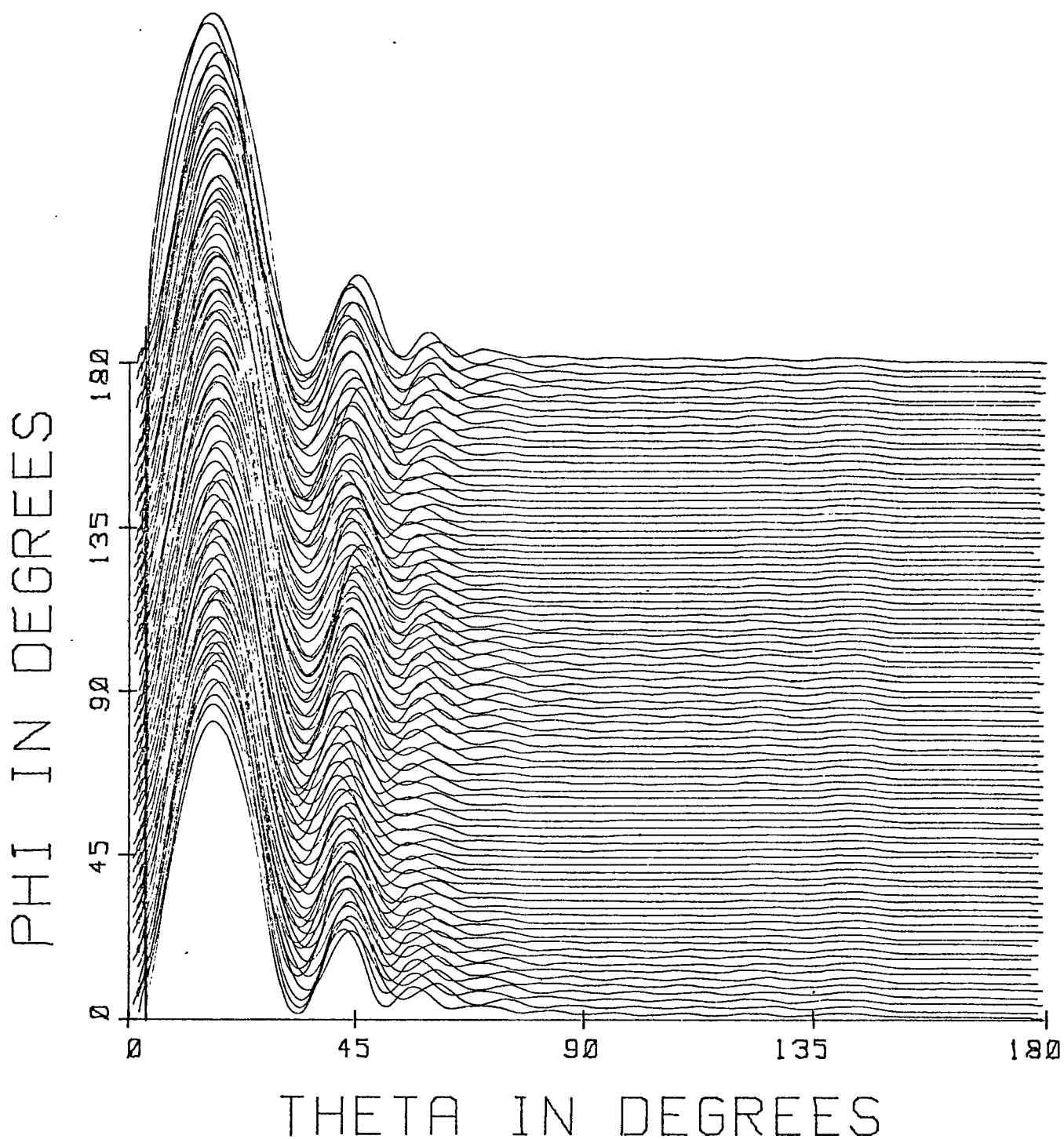


Fig. 2.7 Three-dimensional radiation pattern of the array in Fig. 2.6 operated at 430 MHz,  $D=11.65$  dB,  $\theta_{\max}=19.5^\circ$ .

The two examples described above clearly illustrate the feasibility of constructing a dual-frequency directional Yagi array of circular loops. One potential application of this array is as a coarse/fine tracking antenna. The directional end-fire beam of the low frequency band may first be used to obtain "coarse" tracking of the target. A tracking receiver will indicate "acquisition" when an adequate signal has been picked up by the antenna. After this, a switch to a frequency in the higher band may be used to obtain "FINE" tracking of the target. The sharp null along the axis of the array in this case will result in a "loss of acquisition" at the receiver when the antenna directly points toward the target. This will then be interpreted as "home".

## CHAPTER 3

THE INFINITELY LONG YAGI ARRAY  
OF CONCENTRIC LOOPS--THEORY

## 3.1 WAVE PROPAGATION ON PERIODIC STRUCTURES

The form of guided waves traveling along an axially periodic structure is mathematically described with the help of a representation commonly referred to as Floquet's theorem [12]. With the axial direction denoted by  $z$  and the period by  $d$ , Floquet's theorem may be stated as follows: "A time-harmonic electromagnetic field  $\psi(x,y,z)$  of a normal mode guided along an axially periodic structure is itself periodic in  $z$  with periodicity  $d$  and has the property

$$\psi(x,y,z) = e^{j\beta z} P(x,y,z) \quad (3.1)$$

where  $P(x,y,z)$  is also a periodic function of  $z$  with the period  $d$ ." The generally complex Floquet wave number  $\beta$  is referred to as the fundamental propagation constant.

The periodic function  $P(x,y,z)$  may be expanded in a Fourier series

$$P(x,y,z) = \sum_{n=-\infty}^{+\infty} a_n(x,y) e^{j\frac{2\pi n}{d} z} \quad (3.2)$$

$$\text{then } \psi(x, y, z) = \sum_{n=-\infty}^{+\infty} a_n(x, y) e^{j\beta_n z} \quad (3.3)$$

$$\text{where } \beta_n = \beta + \frac{2\pi n}{d}; \quad n=0, \pm 1, \pm 2, \dots \quad (3.4)$$

The Fourier series expansion indicates that the field of a normal mode of an axially periodic structure is expressible in terms of an infinite number of traveling waves of the form  $a_n(x, y) e^{j\beta_n z}$ , called space harmonics. The wave numbers  $\beta_n$  represent the various space harmonic axial propagation constants, while  $a_n(x, y)$  denote the corresponding space harmonic amplitudes.

The periodic structures described by Floquet's theorem may be divided into two broad categories. They may be closed structures like in an iris-loaded waveguide, or open in one or more transverse dimensions, like in corrugated surfaces, helical lines, and arrays of various elements. While the closed structures support predominantly fast waves that are guided by the conducting enclosures, the open structures support generally slow surface-waves that cling closely to the structure. Attention here is directed towards the latter type, of which the concentric array of loops is one example.

The various methods used in the analysis of the propagating waves on open periodic structures may be grouped into four general methods. The first method is

the classical "field theory" approach in which the problem is formulated as a multi-region boundary value problem. The fields in the different regions are written in the form of doubly infinite fourier series with expansions over all possible modes and space harmonics. The unknown fourier coefficients and the dispersion equations for all possible propagation constants are then obtained by applying the necessary boundary conditions. Aside from mathematical complexity, the "field theory" method is suited only to structures offering regional symmetry. Examples of structures treated by this method are the helical line [13], the array of disks [49], and the array of tape loops [15]. The "equivalent circuit" method regards the periodic structure as a periodically loaded transmission line. A dispersion relation is obtained by combining the circuit equations of a two-port network representation of one section of the loaded line [50]. The ease with which a dispersion relation is obtained renders this method attractive in cases where only an intuitive feel for the nature of wave propagation is desired. However, only gross estimations of phase velocity are possible due to lack of knowledge of exact loading under all possible conditions. This method was used to obtain crude approximations of phase velocity in the case of the array

of rods [20], [23], and the array of short helices [47]. The "circuit theory" method is another approach that has been applied to the analysis of the single array [22], and the coupled coplanar arrays of rods [34]. It involves the derivation of a dispersion equation in terms of mutual impedances between the zeroth element and all the other elements in the array. The solution of such an equation for the propagation constant is then obtained by substituting approximate values for the mutual impedances  $Z_{on}$  from published Tables in the case of small index  $n$ . However, for large values of  $n$ ,  $Z_{on}$  is replaced by an asymptotic expression. A final method, designated here as the "antenna theory" method, is well suited to the analysis of propagating waves on arrays of linear elements such as rods, loops, and slots. It consists basically of calculating the electric field due to all the elements when a surface wave is propagating along the array structure. The tangential component of the electric field is subsequently made to vanish on the surfaces of the elements which leads to a dispersion relation for the propagation constant of the wave. This method was used extensively in the study of the infinite array of rods. There, it met with varying degrees of success depending on the approximations used in the derivation, and on the assumptions made as to the form of the current distribution

on the elements [20], [23], [24], [27]. A recent study avoided the usual a priori assumption of some form of current distribution by combining the "antenna theory" approach with the so-called "point-matching" technique commonly used in the study of wire antennas [30].

In this chapter, the "antenna theory" approach will be used to analyze the propagating waves on the infinitely long Yagi array of concentric loops. A dispersion relation is derived and numerically solved for the phase velocity of the wave. The concentric array of loops is found to possess two distinct propagation bands, and a dual velocity band that is about twice as wide as that found in the case of the single array of loops.

### 3.2 DERIVATION OF THE DISPERSION RELATION

The infinitely long Yagi array of concentric loops is shown in Fig. 3.1, where the parameters ( $a_1, a_2, b_1, b_2,$  and  $d$ ) are defined. The direction of propagation is denoted by  $z$  with the transverse coordinates labeled  $x$  and  $y$  respectively.

The  $m$ th mode is assumed to be propagating along the array. Moreover, currents on the concentric loops of the same cell differ only by a real multiplying factor, while currents on equal size loops of adjacent cells differ only by a phase factor  $e^{j\beta d}$ , where  $\beta$  is the

propagation constant. Also, the current on each loop is assumed to flow in the  $\phi$ -direction only. This implies that the wire loops are electrically thin ( $Ka_1$  and  $Ka_2 \ll 1$ ).

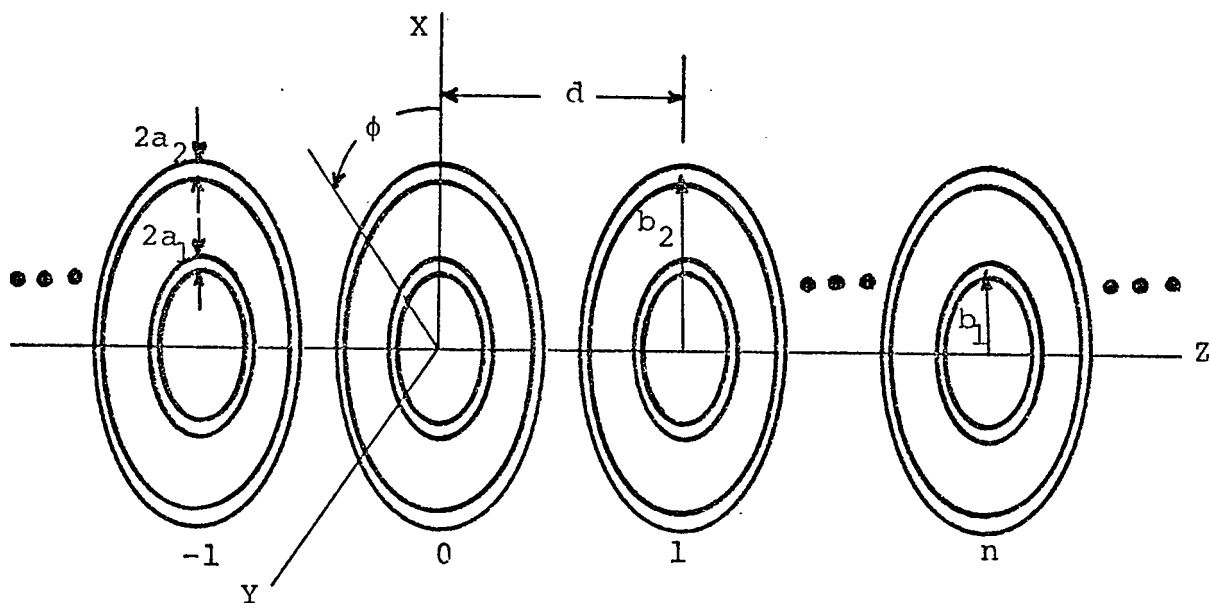


Fig. 3.1. The Yagi array of concentric loops

Therefore, the currents on the two concentric loops of the typical  $n$ th cell may be written as

$$I_{1n} = A_1 \cos m\phi e^{-jn\beta d} \quad (3.1a)$$

$$I_{2n} = A_2 \cos m\phi e^{-jn\beta d} \quad (3.1b)$$

where  $I_{1n}$  and  $I_{2n}$  are the currents on the inner and outer

loop respectively. (Note  $e^{j\omega t}$  variation is implied and suppressed throughout).

A dispersion relation is obtained when the tangential component of the total electric field due to the currents on all the elements is made to vanish on each element of the array. From symmetry considerations, the vanishing of the tangential electric field on the elements of one cell implies its vanishing on the elements of all other cells. Hence, without loss of generality, it suffices to set the tangential electric field equal to zero on the surfaces of the elements contained in the zeroth cell. Thus, in the present analysis the latter condition is adopted.

Let  $P_1(\theta_1, \phi)$  and  $P_2(\theta_2, \phi)$  be two field points located arbitrarily at some angle  $\phi$  on the surfaces of the inner and outer loops respectively of the zeroth cell. Also, let  $P'_1(\theta'_1, \phi')$  and  $P'_2(\theta'_2, \phi')$  be two source points located arbitrarily at some angle  $\phi'$  on the surfaces of the inner and outer loops respectively of the typical  $n$ th cell. This is illustrated in Fig. 3.2.

The  $\phi$ -components of the electric field at the points  $P_1$  and  $P_2$  respectively are given by

$$E_{\phi_1} = E_{\phi_{11}} + E_{\phi_{12}} \quad (3.2a)$$

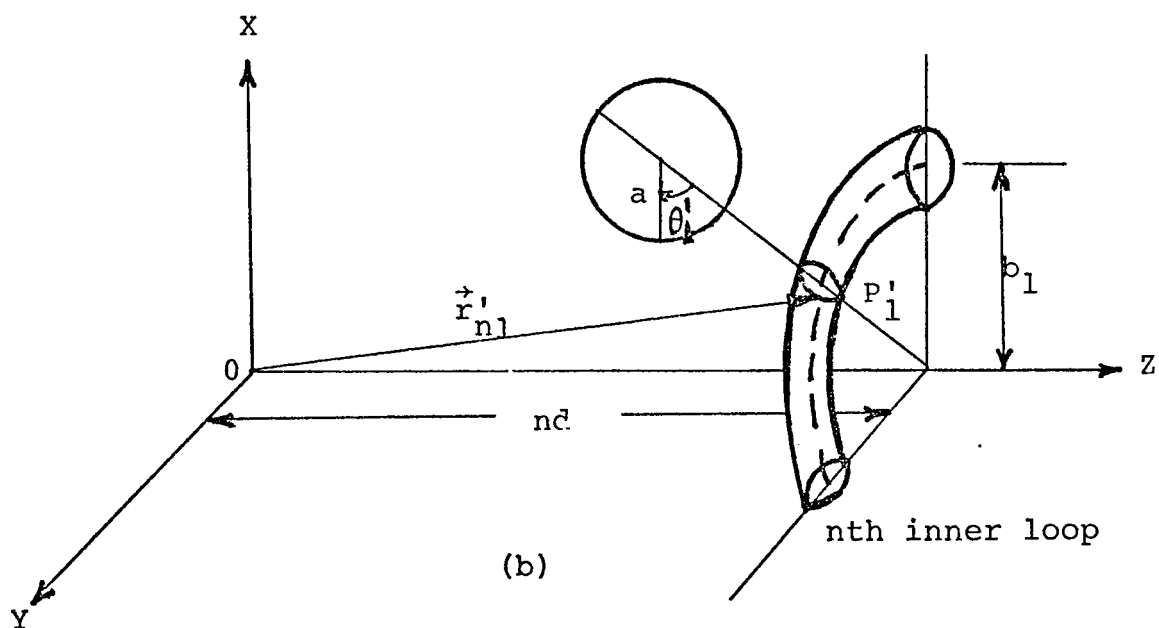
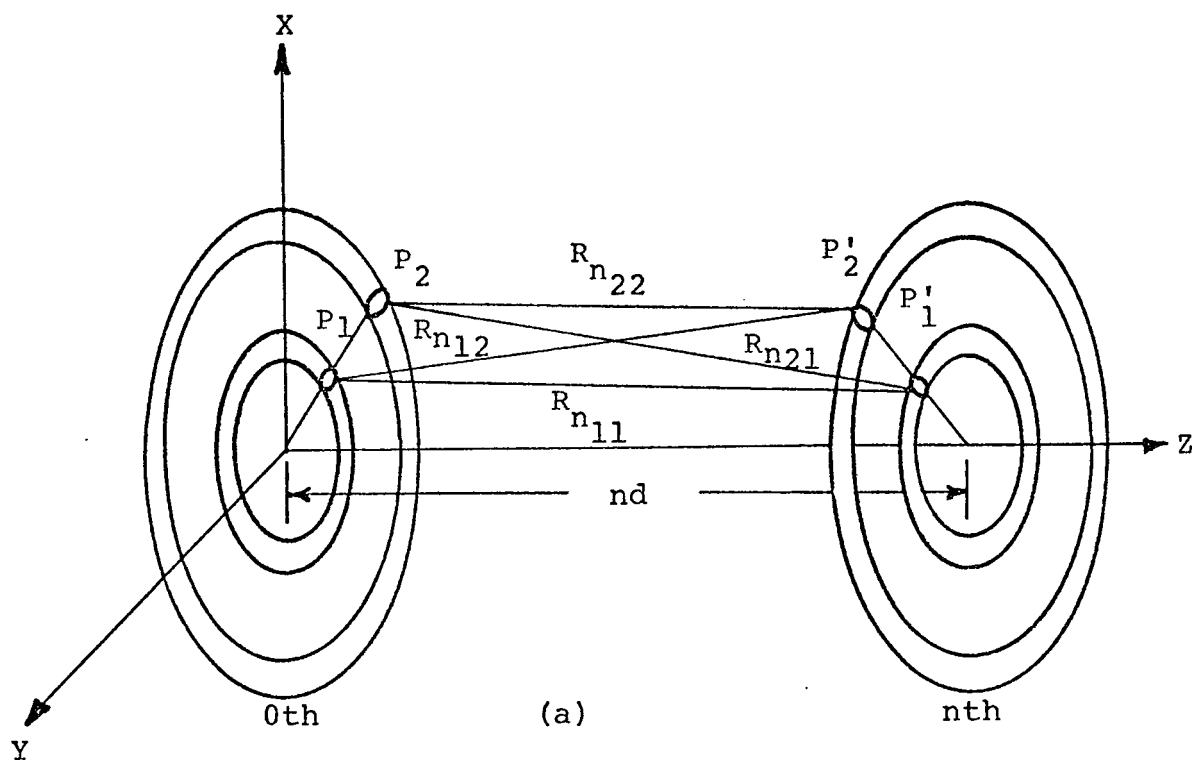


Fig. 3.2 Typical field and source points.  
 (a) Distances; (b) Details

$$E_{\phi_2} = E_{\phi_{22}} + E_{\phi_{21}} \quad (3.2b)$$

where

$E_{\phi_{11}}$  is the field at  $P_1$  due to currents on the inner loop array.

$E_{\phi_{12}}$  is the field at  $P_1$  due to currents on the outer loop array.

$E_{\phi_{22}}$  is the field at  $P_2$  due to currents on the outer loop array.

$E_{\phi_{21}}$  is the field at  $P_2$  due to currents on the inner loop array.

In order to determine each of these field components, it is necessary to derive expressions for the distances depicted in Fig. 3.2. This task is undertaken first. Then, an evaluation of each of the field components is made. Finally, setting  $E_{\phi_1}$  and  $E_{\phi_2}$  equal to zero yields the required dispersion relation.

### 3.2.1 Evaluation of $R_{n11}$

$R_{n11}$  is defined by

$$R_{n11}^2 = |\vec{r}_{01} - \vec{r}'_{n1}|^2 \quad (3.3)$$

where  $\vec{r}_{01} = x_1 \hat{x} + y_1 \hat{y} + z_1 \hat{z}$  and  $\vec{r}'_{n1} = x'_1 \hat{x} + y'_1 \hat{y} + z'_1 \hat{z}$  with the components given as

$$x_1 = (b_1 - a_1 \cos \theta_1) \cos \phi \quad (3.4a)$$

$$y_1 = (b_1 - a_1 \cos \theta_1) \sin \phi \quad (3.4b)$$

$$z_1 = a_1 \sin \theta_1 \quad (3.4c)$$

and,

$$x'_1 = (b_1 - a_1 \cos \theta'_1) \cos \phi' \quad (3.5a)$$

$$y'_1 = (b_1 - a_1 \cos \theta'_1) \sin \phi' \quad (3.5b)$$

$$z'_1 = nd + a_1 \sin \theta'_1 \quad (3.5c)$$

Using (3.4) and (3.5) in (3.3), the expression for  $R_{n11}$  becomes

$$\begin{aligned} R_{n11}^2 = & [(b_1 - a_1 \cos \theta_1) \cos \phi - (b_1 - a_1 \cos \theta'_1) \cos \phi']^2 \\ & + [(b_1 - a_1 \cos \theta_1) \sin \phi - (b_1 - a_1 \cos \theta'_1) \sin \phi']^2 \\ & + [a_1 \sin \theta_1 - nd - a_1 \sin \theta'_1]^2 \quad (3.6) \end{aligned}$$

Squarring and combining terms yields

$$\begin{aligned} R_{n11}^2 = & (b_1 - a_1 \cos \theta_1)^2 + (b_1 - a_1 \cos \theta'_1)^2 - 2(b_1 - a_1 \cos \theta_1) \\ & (b_1 - a_1 \cos \theta'_1) \cos \phi \cos \phi' - 2(b_1 - a_1 \cos \theta_1) (b_1 - a_1 \cos \theta'_1) \\ & \sin \phi \sin \phi' + n^2 d^2 + a_1^2 (\sin \theta_1 - \sin \theta'_1)^2 - 2nd a_1 (\sin \theta_1 - \sin \theta'_1) \quad (3.7) \end{aligned}$$

Squarring terms and using  $\cos \phi \cos \phi' = [\cos(\phi + \phi') + \cos(\phi - \phi')]/2$  with  $\sin \phi \sin \phi' = [\cos(\phi - \phi') - \cos(\phi + \phi')]/2$  and rearranging, yields

$$\begin{aligned}
R_{n11}^2 = & 2b_1^2 [1 - \cos(\phi - \phi')] - 2a_1 b_1 (\cos\theta_1 + \cos\theta_1') [1 - \cos(\phi - \phi')] \\
& + 2a_1^2 - 2a_1^2 [\cos\theta_1 \cos\theta_1' + \sin\theta_1 \sin\theta_1'] + 2a_1^2 \cos\theta_1 \cos\theta_1' \\
& [1 - \cos(\phi - \phi')] + n^2 d^2 - 2nda_1 (\sin\theta_1 - \sin\theta_1') \quad (3.8)
\end{aligned}$$

Using the trigonometric identities  $\cos(\theta_1 - \theta_1') = \cos\theta_1 \cos\theta_1' + \sin\theta_1 \sin\theta_1'$ ;  $2 \sin^2 [(\phi - \phi')/2] = 1 - \cos(\phi - \phi')$ , and  $2 \sin^2 [(\theta_1 - \theta_1')/2] = 1 - \cos(\theta_1 - \theta_1')$  one obtains

$$\begin{aligned}
R_{n11}^2 = & 4b_1^2 \sin^2 [(\phi - \phi')/2] + 4a_1^2 \sin^2 [(\theta_1 - \theta_1')/2] + n^2 d^2 - 2nda_1 \\
& (\sin\theta_1 - \sin\theta_1') + 4a_1^2 \cos\theta_1 \cos\theta_1' \sin^2 [(\phi - \phi')/2] - 4a_1 b_1 (\cos\theta_1 \\
& + \cos\theta_1') \sin^2 [(\phi - \phi')/2] \quad (3.9)
\end{aligned}$$

Equation (3.9) may be simplified further by making the following approximations

$$n^2 d^2 - 2nda_1 (\sin\theta_1 - \sin\theta_1') \approx n^2 d^2 \quad (3.10a)$$

$$(4b_1^2 + 4a_1^2 \cos\theta_1 \cos\theta_1') \sin^2 [(\phi - \phi')/2] \approx 4b_1^2 \sin^2 \left\{ \frac{\phi - \phi'}{2} \right\} \quad (3.10b)$$

The first approximation is valid if  $4a_1 \ll d$ , and the second one is valid if  $a_1 \ll b_1$ . Under these conditions, the expression for  $R_{n11}$  reduces to

$$R_{n11}^2 = 4b_1^2 \sin^2 [(\phi - \phi')/2] + 4a_1^2 \sin^2 [(\theta_1 - \theta_1')/2] + n^2 d^2 \quad (3.11)$$

subject to the following

$$a_1 \ll b_1; 4a_1 \ll d \quad (3.12)$$

### 3.2.2 Evaluation of $R_{n22}$

The expression for  $R_{n22}$  may be deduced from that of  $R_{n11}$  by a simple change of subscripts. Hence,

$$R_{n22}^2 = 4b_2^2 \sin^2[(\phi - \phi')/2] + 4a_2^2 \sin^2[(\theta_2 - \theta_2')/2] + n^2 d^2 \quad (3.13)$$

with the conditions

$$a_2 \ll b_2; 4a_2 \ll d \quad (3.14)$$

### 3.2.3 Evaluation of $R_{n21}$

$R_{n21}$  is defined by

$$R_{n21}^2 = |\vec{r}_{02} - \vec{r}'_{n1}|^2 \quad (3.15)$$

where  $\vec{r}_{02} = x_2 \hat{x} + y_2 \hat{y} + z_2 \hat{z}$  and  $\vec{r}'_{n1} = x'_1 \hat{x} + y'_1 \hat{y} + z'_1 \hat{z}$ . The components of the vector  $\vec{r}_{02}$  are

$$x_2 = (b_2 - a_2 \cos \theta_2) \cos \phi \quad (3.16a)$$

$$y_2 = (b_2 - a_2 \cos \theta_2) \sin \phi \quad (3.16b)$$

$$z_2 = a_2 \sin \theta_2 \quad (3.16c)$$

while the components of  $r'_{n1}$  have already been defined in (3.5). Then,  $R_{n21}$  may be written as

$$R_{n21}^2 = [(b_2 - a_2 \cos \theta_2) \cos \phi - (b_1 - a_1 \cos \theta_1') \cos \phi']^2 + [(b_2 - a_2 \cos \theta_2) \sin \phi - (b_1 - a_1 \cos \theta_1') \sin \phi']^2 + [a_2 \sin \theta_2 - nd - a_1 \sin \theta_1']^2 \quad (3.17)$$

Squaring and combining terms yields

$$R_{n21}^2 = (b_2 - a_2 \cos \theta_2)^2 + (b_1 - a_1 \cos \theta_1')^2 - 2(b_2 - a_2 \cos \theta_2)(b_1 - a_1 \cos \theta_1') \cos \phi \cos \phi' - 2(b_2 - a_2 \cos \theta_2)(b_1 - a_1 \cos \theta_1') \sin \phi \sin \phi' + n^2 d^2 + (a_2 \sin \theta_2 - a_1 \sin \theta_1')^2 - 2nd(a_2 \sin \theta_2 - a_1 \sin \theta_1') \quad (3.18)$$

Squaring terms and then using the identities

$$\cos \phi \cos \phi' = [\cos(\phi + \phi') + \cos(\phi - \phi')] / 2; \quad \sin \phi \sin \phi' = [\cos(\phi - \phi') - \cos(\phi + \phi')] / 2 \text{ and rearranging, yields}$$

$$R_{n21}^2 = b_1^2 + b_2^2 - 2b_1 b_2 \cos(\phi - \phi') - 2(a_2 b_2 \cos \theta_2 + a_1 b_1 \cos \theta_1') + a_1^2 + a_2^2 + 2(a_1 b_2 \cos \theta_1' + a_2 b_1 \cos \theta_2) \cos(\phi - \phi') - 2a_1 a_2 (\cos \theta_2 \cos \theta_1' + \sin \theta_2 \sin \theta_1') + 2a_1 a_2 \cos \theta_2 \cos \theta_1' [1 - \cos(\phi - \phi')] + n^2 d^2 - 2nd(a_2 \sin \theta_2 - a_1 \sin \theta_1') \quad (3.19)$$

Using the trigonometric identities  $\cos(\theta_2 - \theta_1') = \cos\theta_2 \cos\theta_1' + \sin\theta_2 \sin\theta_1'$ ;  $2 \sin^2[(\phi - \phi')/2] = 1 - \cos(\phi - \phi')$ , and  $2 \sin^2[(\theta_2 - \theta_1')/2] = 1 - \cos(\theta_2 - \theta_1')$  one obtains

$$R_{n21}^2 = (b_2 - b_1)^2 + 4b_1 b_2 \sin^2[(\phi - \phi')/2] + (a_2 - a_1)^2 + 4a_1 a_2 \sin^2[(\theta_2 - \theta_1')/2] + n^2 d^2 - 2nd(a_2 \sin\theta_2 - a_1 \sin\theta_1') + 4a_1 a_2 \cos\theta_2 \cos\theta_1' \sin^2[(\phi - \phi')/2] - 2a_2(b_2 - b_1)\cos\theta_2 + 2a_1(b_2 - b_1)\cos\theta_1' - 4(a_1 b_2 \cos\theta_1' + a_2 b_1 \cos\theta_2) \sin^2[(\phi - \phi')/2] \quad (3.20)$$

Equation (3.20) may be simplified considerably by making the following approximations

$$n^2 d^2 - 2nd(a_2 \sin\theta_2 - a_1 \sin\theta_1') \approx n^2 d^2 \quad (3.21a)$$

$$b_1 b_2 + a_1 a_2 \cos\theta_2 \cos\theta_1' - (a_1 b_2 \cos\theta_1' + a_2 b_1 \cos\theta_2) \approx b_1 b_2 \quad (3.21b)$$

$$(b_2 - b_1)^2 + 2(b_2 - b_1)(a_1 \cos\theta_1' - a_2 \cos\theta_2) \approx (b_2 - b_1)^2 \quad (3.21c)$$

The approximation of (3.21a) is valid when  $2(a_1 + a_2) \ll d$ , that of (3.21b) is satisfied when  $(a_1/b_1) + (a_2/b_2) \ll 1$ , and (3.21c) holds when  $2(a_1 + a_2) \ll b_2 - b_1$ . Under these conditions, the expression for  $R_{n21}$  reduces to

---


$$R_{n21}^2 = (b_2 - b_1)^2 + 4b_1 b_2 \sin^2[(\phi - \phi')/2] + n^2 d^2 \quad (3.22)$$

subject to the following

$$2(a_1+a_2) \ll d; 2(a_1+a_2) \ll b_2-b_1; (a_1/b_1)+(a_2/b_2) \ll 1 \quad (3.23)$$

### 3.2.4 Evaluation of $R_{n21}$

From symmetry considerations  $R_{n12}$  is equal to  $R_{n21}$ . This may also be seen by interchanging subscripts in the expression for  $R_{n21}$ .

### 3.2.5 Evaluation of $E_{\phi 11}$

The scalar and vector potentials at the point  $P_1$  (see Fig. 3.2) due to contributions from all elements of the inner loop array, are given by the following integrals

$$A_{\phi 11} = \frac{\mu_0}{4\pi} \int_{-\pi}^{\pi} I_1(\phi') W_{11}(\phi-\phi') \cos(\phi-\phi') b_1 d\phi' \quad (3.24)$$

$$\phi_{11} = \frac{1}{4\pi\epsilon_0} \int_{-\pi}^{\pi} q_1(\phi') W_{11}(\phi-\phi') b_1 d\phi' \quad (3.25)$$

where  $I_1(\phi')$  and  $q_1(\phi')$  are the total current and charge per unit length of inner loop. The Kernel  $W_{11}(\phi-\phi')$  is given by

$$W_{11}(\phi-\phi') = \sum_{n=-\infty}^{+\infty} e^{-j\beta n d} \left[ \frac{1}{2\pi} \int_{-\pi}^{\pi} \frac{e^{-jKR_{n11}}}{R_{n11}} d\theta'_1 \right] \quad (3.26)$$

where  $R_{n11}$  is defined in (3.11).  $\mu_0, \epsilon_0$  and  $K$  are the

permeability, permittivity, and propagation constant in free space. The equation of continuity for the currents and charges in the inner loop yields

$$\frac{1}{b_1} \frac{dI_1(\phi')}{d\phi'} + j\omega q_1(\phi') = 0 \quad (3.27)$$

Solving for  $q_1(\phi')$  one obtains

$$q_1(\phi') = \frac{j}{\omega b_1} I_1'(\phi') \quad (3.28)$$

Using (3.28) in the expression for  $\Phi_{11}$  gives

$$\Phi_{11} = \frac{j}{4\pi\omega\epsilon_0} \int_{-\pi}^{\pi} I_1'(\phi') W_{11}(\phi-\phi') d\phi' \quad (3.29)$$

By differentiating with respect to  $\phi$  and using the condition  $\partial W_{11}/\partial\phi = -\partial W_{11}/\partial\phi'$ , the following results

$$\frac{\partial\Phi_{11}}{\partial\phi} = \frac{-j}{4\pi\omega\epsilon_0} \int_{-\pi}^{\pi} I_1'(\phi') \frac{\partial}{\partial\phi'} W_{11}(\phi-\phi') d\phi' \quad (3.30)$$

Integrating the right-hand side of (3.30) by parts and making use of the fact that  $I_1'(\pi) = I_1'(-\pi) = 0$  yields

---


$$\frac{\partial\Phi_{11}}{\partial\phi} = \frac{j}{4\pi\omega\epsilon_0} \int_{-\pi}^{\pi} W_{11}(\phi-\phi') I_1''(\phi') d\phi' \quad (3.31)$$

where  $I_1''(\phi')$  is the second derivative of  $I_1(\phi')$  with respect to  $\phi'$ .

From the defining relation  $\vec{E} = -j\omega\vec{A} - \nabla\phi$  for the electric field it follows that on the surface of the inner loop

$$E_{\phi_{11}} = -j\omega A_{\phi_{11}} - \frac{1}{b_1} \frac{\partial \phi_{11}}{\partial \phi} \quad (3.32)$$

Upon substituting (3.24) and (3.31) in (3.32) it follows that

$$E_{\phi_{11}} = \frac{-j}{4\pi\omega\epsilon_0 b_1} \left[ \int_{-\pi}^{\pi} d\phi' I_1''(\phi') W_{11}(\phi - \phi') + \right. \\ \left. K^2 b_1^2 \int_{-\pi}^{\pi} d\phi' \cos(\phi - \phi') I_1(\phi') W_{11}(\phi - \phi') \right] \quad (3.33)$$

Let us now decompose the expression for  $R_{n11}$  into two parts as follows

$$R_{n11}^2 = A^2 + n^2 d^2 \quad (3.34)$$

where  $A^2 = 4b_1^2 \sin^2[(\phi - \phi')/2] + 4a_1^2 \sin^2[(\theta_1 - \theta'_1)/2]$

Then the Kernel  $W_{11}(\phi - \phi')$  may be written as

---


$$W_{11}(\phi - \phi') = \frac{1}{2\pi} \int_{-\pi}^{\pi} d\theta'_1 \sum_{n=-\infty}^{+\infty} e^{-j\beta n d} \frac{e^{-jK\sqrt{A^2 + n^2 d^2}}}{\sqrt{A^2 + n^2 d^2}} \quad (3.35)$$

An equivalent representation to (3.35) may be obtained by invoking the Poisson's summation formula [51]

$$\sum_{n=-\infty}^{+\infty} f(nd) = \frac{1}{d} \sum_{m=-\infty}^{+\infty} F \left[ \frac{2\pi m}{d} \right] \quad (3.36)$$

where  $F$  denotes the exponential Fourier transform of the function  $f$ ; i.e.,

$$F(x) = \int_{-\infty}^{+\infty} f(t) e^{-jxt} dt \quad (3.37)$$

Using (3.36) and (3.37) in (3.35) the Kernel  $W_{11}(\phi-\phi')$  may be written as

$$W_{11}(\phi-\phi') = \frac{1}{2\pi} \int_{-\pi}^{+\pi} d\theta \int_{-\infty}^{+\infty} dt \left\{ \frac{1}{d} \sum_{m=-\infty}^{+\infty} \int_{-\infty}^{+\infty} e^{-jt(\beta + \frac{2\pi m}{d})} \frac{e^{-jK\sqrt{A^2+t^2}}}{\sqrt{A^2+t^2}} dt \right\} \quad (3.38)$$

By Floquet's theorem  $\beta_m = \beta + 2m\pi/d$  and the indefinite integral in (3.38) is readily evaluated as [52]

$$\int_{-\infty}^{+\infty} e^{-j\beta_m t} \frac{e^{-jK\sqrt{A^2+t^2}}}{\sqrt{A^2+t^2}} dt = 2K_0(A\sqrt{\beta_m^2 - K^2}) \quad (3.39)$$

where  $K_0$  is the modified Bessel function of zero order.

Let  $\gamma_m^2 = \beta_m^2 - K^2$ , then the Kernel in (3.38) is given by

$$W_{11}(\phi - \phi') = \frac{1}{\pi d} \int_{-\pi}^{\pi} d\theta'_1 \sum_{n=-\infty}^{+\infty} K_0(A\gamma_n) \quad (3.40)$$

Returning to equation (3.33) and substituting  $I_1(\phi')$  by  $A_1 \cos m\phi'$  and  $I_1''(\phi')$  by  $-m^2 A_1 \cos m\phi'$ , the expression for  $E_{\phi_{11}}$  becomes

$$E_{\phi_{11}} = \frac{-jA_1}{4\pi\omega\epsilon_0 b_1} \left\{ -m^2 \int_{-\pi}^{\pi} d\phi' \cos m\phi' W_{11}(\phi - \phi') \right. \\ \left. + K^2 b_1^2 \int_{-\pi}^{\pi} d\phi' \cos(\phi - \phi') \cos m\phi' W_{11}(\phi - \phi') \right\} \quad (3.41)$$

Performing a change of variable  $\alpha = \phi' - \phi$ ;  $d\alpha = d\phi'$ , yields

$$E_{\phi_{11}} = \frac{-jA_1}{4\pi\omega\epsilon_0 b_1} \left\{ -m^2 \int_{-\pi}^{\pi} d\alpha \cos m(\alpha + \phi) W_{11}(\alpha) + \right. \\ \left. K^2 b_1^2 \int_{-\pi}^{\pi} d\alpha \cos \alpha \cos m(\alpha + \phi) W_{11}(\alpha) \right\} \quad (3.42)$$

Using the trigonometric identity  $\cos m(\alpha + \phi) = \cos m\alpha \cos m\phi - \sin m\alpha \sin m\phi$ , and noting that only the  $\cos m\alpha$  term contributes to the integral leads to the following result

$$E_{\phi_{11}} = \frac{-jA_1 \cos m\phi}{4\pi\omega\epsilon_0 b_1} \left\{ -m^2 \int_{-\pi}^{\pi} d\alpha \cos m\alpha W_{11}(\alpha) \right.$$

$$+K^2 b_1^2 \int_{-\pi}^{\pi} d\alpha \cos \alpha \cos m\alpha W_{11}(\alpha) \} \quad (3.43)$$

If use of the identity  $\cos \alpha \cos m\alpha = [\cos(m+1)\alpha + \cos(m-1)\alpha]/2$  is made in (3.43) one obtains

$$E_{\phi_{11}} = \frac{-jA_1 \cos m\phi}{4\pi\omega\epsilon_0 b_1} \left\{ -m^2 Q_m + \frac{K^2 b_1^2}{2} (Q_{m+1} + Q_{m-1}) \right\} \quad (3.44)$$

$$\text{where } Q_m = \int_{-\pi}^{\pi} d\alpha \cos m\alpha W_{11}(\alpha) \quad (3.45)$$

Since the integral in the expression for  $W_{11}(\alpha)$  (Eq. 3.40) remains invariant when a change of variable  $\theta = (\theta_1 - \theta_1')$  is made,  $Q_m$  may be expressed as

$$Q_m = \frac{1}{\pi d} \int_{-\pi}^{\pi} d\theta \int_{-\pi}^{\pi} d\alpha \cos m\alpha \sum_{n=-\infty}^{+\infty} K_0(A\gamma_n) \quad (3.46)$$

where  $A = [2b_1^2(1 - \cos\alpha) + a_1'^2]^{\frac{1}{2}}$ . Note: use was made of the identity  $2\sin^2\alpha/2 = 1 - \cos\alpha$ , and  $a_1'$  is equal to  $2a_1 \sin\theta/2$ . An addition theorem given on page 102 of [53], expresses the zero order modified Bessel function as a series of products of Bessel functions; i.e.,

$$K_0(w) = \sum_{\ell=-\infty}^{+\infty} K_{\ell}(z) I_{\ell}(z) e^{j\ell\alpha} \quad (3.47)$$

where  $w = (z^2 + z^2 - 2zz\cos\alpha)^{\frac{1}{2}}$ .

Setting  $w = A\gamma_n$  and solving for  $z$  and  $Z$  with the condition  $|Z| > |z|$ , yields the result

$$z_n = \frac{\gamma_n}{2} (\sqrt{4b_1^2 + a_1'^2} + |a_1'|) \quad (3.48a)$$

$$z_n = \frac{\gamma_n}{2} (\sqrt{4b_1^2 + a_1'^2} - |a_1'|) \quad (3.48b)$$

Inserting (3.47) in (3.46), the expression for  $Q_m$  becomes

$$Q_m = \frac{1}{\pi d} \int_{-\pi}^{\pi} d\theta \sum_{n=-\infty}^{+\infty} \int_{-\pi}^{\pi} d\alpha \cos m\alpha \sum_{\ell=-\infty}^{+\infty} K_{\ell}(Z_n) I_{\ell}(z_n) [\cos \ell\alpha + j \sin \ell\alpha] \quad (3.49)$$

Only the real part of the integrand in (3.49) contributes to the integral, and only when  $\ell = \pm m$ . Hence,

$$Q_m = \frac{2}{d} \int_{-\pi}^{\pi} d\theta \sum_{n=-\infty}^{+\infty} K_m(Z_n) I_m(z_n) \quad (3.50)$$

where  $I_m$  and  $K_m$  are the modified Bessel functions of the first and second kind of order  $m$ . Substituting  $Q_m$  by its value in (3.44) gives

$$E_{\phi 11} = \frac{-jA_1 \cos m\phi}{2\pi \epsilon_0 \omega b_1 d} \int_{-\pi}^{\pi} d\theta \sum_n \left\{ \frac{K^2 b_1^2}{2} (K_{m+1} I_{m+1} + K_{m-1} I_{m-1}) - m^2 K_m I_m \right\} \quad (3.51)$$

where the arguments of the Bessel functions  $z_n$  and  $Z_n$  have been suppressed for simplicity. In Appendix A, it is shown that

$$K_{m+1}I_{m+1} + K_{m-1}I_{m-1} = - \left( \frac{2m^2}{z_n Z_n} I_m K_m + 2K'_m I'_m \right) \quad (3.52)$$

Using (3.52) in (3.51) and combining terms, it follows that

$$E_{\phi 11} = \frac{jA_1 \omega \mu_0 b_1 \cos m \phi}{2\pi d} \sum_n \int_{-\pi}^{\pi} d\theta \left\{ \left( \frac{m\beta_n}{Kb_1 \gamma_n} \right)^2 I_m K_m + I'_m K'_m \right\} \quad (3.53)$$

where the relations  $z_n Z_n = b_1^2 \gamma_n^2$  and  $K^2 + \gamma_n^2 = \beta_n^2$  have been used. In order to extract the  $\theta$ -dependency from the arguments of the Bessel functions, the following approximations are made.

$$I_m(z_n) \approx I_m(\gamma_n b_1) e^{-\gamma_n |a'|/2} \quad (3.54a)$$

$$K_m(Z_n) \approx K_m(\gamma_n b_1) e^{-\gamma_n |a'|/2} \quad (3.54b)$$

Since  $a_1 \ll b_1$ , these approximations are quite close to the exact values. Then, the expression for  $E_{\phi 11}$  becomes

$$E_{\phi 11} = \frac{jA_1 \omega \mu_0 b_1 \cos m \phi}{d} \sum_n \left\{ \left( \frac{m\beta_n}{Kb_1 \gamma_n} \right)^2 I_m(\gamma_n b_1) K_m(\gamma_n b_1) \right.$$

$$+I'_m(\gamma_n b_1)K'_m(\gamma_n b_1)\} \frac{1}{2\pi} \int_0^{2\pi} e^{-2\gamma_n a_1 \sin|\theta/2|} d\theta \quad (3.55)$$

The integral in (3.55) may be expressed in terms of a tabulated function by performing a change of variable  $\alpha = \theta/2$ ,  $d\alpha = d\theta/2$ . It follows that

$$\frac{1}{2\pi} \int_0^{2\pi} e^{-2\gamma_n a_1 \sin|\theta/2|} d\theta = \frac{1}{\pi} \int_0^\pi e^{-2\gamma_n a_1 \sin\alpha} d\alpha = S(2\gamma_n a_1) \quad (3.56)$$

where  $S(x)$  is the struve function [54]

$$S(x) = \frac{1}{\pi} \int_0^\pi e^{-x \sin\alpha} d\alpha \quad (3.57)$$

Substituting (3.56) in (3.55), the final expression for  $E_{\phi_{11}}$  results

$$E_{\phi_{11}} = \frac{jA_1 \eta_0 K b_1 \cos m\phi}{d} \sum_n \left\{ \left( \frac{m\beta_n}{K b_1 \gamma_n} \right)^2 I_m(\gamma_n b_1) K_m(\gamma_n b_1) + I'_m(\gamma_n b_1) K'_m(\gamma_n b_1) \right\} S(2\gamma_n a_1) \quad (3.58)$$

where  $\eta_0$  is the intrinsic impedance of free space.

### 3.2.6 Evaluation of $E_{\phi_{22}}$

The expression for  $E_{\phi_{22}}$  may be obtained from that of  $E_{\phi_{11}}$  by replacing  $a_1$ ,  $b_1$ , and  $A_1$  by  $a_2$ ,  $b_2$ , and  $A_2$

respectively. Hence,

$$E_{\phi_{22}} = \frac{jA_2 \eta_0 K b_2 \cos m\phi}{d} \sum_n \left\{ \left( \frac{m\beta_n}{K b_2 \gamma_n} \right)^2 I_m(\gamma_n b_2) K_m(\gamma_n b_2) \right. \\ \left. + I'_m(\gamma_n b_2) K'_m(\gamma_n b_2) \right\} S(2\gamma_n a_2) \quad (3.59)$$

### 3.2.7 Evaluation of $E_{\phi_{21}}$

The scalar and vector potentials at the point  $P_2$  (Fig. 3.2) due to contributions from all elements of the inner loop array, are given by the integrals

$$A_{\phi_{21}} = \frac{\mu_0}{4\pi} \int_{-\pi}^{\pi} I_1(\phi') W_{21}(\phi - \phi') \cos(\phi - \phi') b_1 d\phi' \quad (3.60)$$

$$\Phi_{21} = \frac{1}{4\pi\epsilon_0} \int_{-\pi}^{\pi} q_1(\phi') W_{21}(\phi - \phi') b_1 d\phi' \quad (3.61)$$

where the Kernel  $W_{21}(\phi - \phi')$  is given by

$$W_{21}(\phi - \phi') = \sum_{n=-\infty}^{+\infty} e^{-j\beta n d} \left[ \frac{1}{2\pi} \int_{-\pi}^{\pi} \frac{e^{-jKR_{n21}}}{R_{n21}} d\theta'_1 \right] \quad (3.62)$$

with the distance  $R_{n21}$  defined in (3.22).

Replacing  $q_1(\phi')$  in (3.61) by its value from (3.28), yields

$$\Phi_{21} = \frac{j}{4\pi\omega\epsilon_0} \int_{-\pi}^{\pi} I_1'(\phi') W_{21}(\phi-\phi') d\phi' \quad (3.63)$$

Differentiating  $\Phi_{21}$  with respect to  $\phi$ , and using the condition  $\partial W_{21}/\partial\phi = -\partial W_{21}/\partial\phi'$  followed by integration of the right-hand side by parts, leads to the result

$$\frac{\partial\Phi_{21}}{\partial\phi} = \frac{j}{4\pi\omega\epsilon_0} \int_{-\pi}^{\pi} W_{21}(\phi-\phi') I_1''(\phi') d\phi' \quad (3.64)$$

On the surface of the outer loop, the electric field may be expressed as

$$E_{\phi_{21}} = -j\omega A_{\phi_{21}} - \frac{1}{b_2} \frac{\partial\Phi_{21}}{\partial\phi} \quad (3.65)$$

Upon substituting (3.60) and (3.64) in (3.65) it follows that

$$E_{\phi_{21}} = \frac{-j}{4\pi\omega\epsilon_0 b_2} \left( \int_{-\pi}^{\pi} d\phi' I_1''(\phi') W_{21}(\phi-\phi') + \right. \\ \left. K^2 b_1 b_2 \int_{-\pi}^{\pi} d\phi' \cos(\phi-\phi') I_1(\phi') W_{21}(\phi-\phi') \right) \quad (3.66)$$

By decomposing the expression for  $R_{n_{21}}$  into two parts, the Kernel  $W_{21}(\phi-\phi')$  may be written as

$$W_{21}(\phi-\phi') = \frac{1}{2\pi} \int_{-\pi}^{\pi} d\theta_1' \sum_{n=-\infty}^{+\infty} e^{-j\beta n d} \frac{e^{-jK\sqrt{B^2+n^2d^2}}}{\sqrt{B^2+n^2d^2}} \quad (3.67)$$

where  $B^2 = (b_2 - b_1)^2 + 4b_1b_2 \sin^2[(\phi - \phi')/2]$ . Applying Poisson's summation formula to the series in (3.67), the Kernel may be put in the following form

$$W_{21}(\phi - \phi') = \frac{1}{\pi d} \int_{-\pi}^{\pi} d\theta'_1 \sum_{n=-\infty}^{+\infty} K_0(B\gamma_n) \quad (3.68)$$

The substitution of  $I_1(\phi') = A_1 \cos m\phi'$  and  $I_1''(\phi') = -m^2 A_1 \cos m\phi'$  into equation (3.66) yields

$$E_{\phi_{21}} = \frac{-jA_1}{4\pi\omega\epsilon_0 b_2} \left\{ \int_{-\pi}^{\pi} d\phi' \cos m\phi' W_{21}(\phi - \phi') \right. \\ \left. + K^2 b_1 b_2 \int_{-\pi}^{\pi} d\phi' \cos(\phi - \phi') \cos m\phi' W_{21}(\phi - \phi') \right\} \quad (3.69)$$

Performing a change of variable  $\alpha = \phi' - \phi$ , and using the identities  $\cos m(\alpha + \phi) = \cos m\alpha \cos m\phi - \sin m\alpha \sin m\phi$ ;  $\cos \alpha \cos m\alpha = [\cos(m+1)\alpha + \cos(m-1)\alpha]/2$ , the expression for  $E_{\phi_{21}}$  becomes

$$E_{\phi_{21}} = \frac{-jA_1 \cos m\phi}{4\pi\omega\epsilon_0 b_2} \left\{ -m^2 Q_m + \frac{K^2 b_1 b_2}{2} (Q_{m+1} + Q_{m-1}) \right\} \quad (3.70)$$

$$\text{where } Q_m = \frac{1}{\pi d} \int_{-\pi}^{\pi} d\theta'_1 \int_{-\pi}^{\pi} d\alpha \cos m\alpha \sum_{n=-\infty}^{+\infty} K_0(B\gamma_n) \quad (3.71)$$

$$\text{and } B = [b_1^2 + b_2^2 - 2b_1 b_2 \cos \alpha]^{\frac{1}{2}}.$$

Using the addition theorem (Eq. 3.47), the expression for  $Q_m$  may be put in alternative form

$$Q_m = \frac{2}{d} \int_{-\pi}^{\pi} d\theta'_1 \sum_{n=-\infty}^{+\infty} K_m(\gamma_n b_2) I_m(\gamma_n b_1) \quad (3.72)$$

The integration with respect to  $\theta'_1$  in (3.72) is trivial.

Then,

$$Q_m = \frac{4\pi}{d} \sum_{n=-\infty}^{+\infty} K_m(\gamma_n b_2) I_m(\gamma_n b_1) \quad (3.73)$$

Replacing  $Q_m$  by its value in (3.70) yields the following result

$$E_{\phi_{21}} = \frac{-jA_1 \cos m\phi}{\omega \epsilon_0 b_2 d} \sum_n \left\{ \frac{K^2 b_1 b_2}{2} (K_{m+1} I_{m+1} + K_{m-1} I_{m-1}) - m^2 K_m I_m \right\} \quad (3.74)$$

Finally, making use of equation (3.52) with  $z_n Z_n = \gamma_n^2 b_1^2$ , and combining terms gives

$$E_{\phi_{21}} = \frac{jA_1 \eta_0 K b_1 \cos m\phi}{d} \sum_n \left\{ \left( \frac{m\beta_n}{K b_0 \gamma_n} \right)^2 I_m K_m + I'_m K'_m \right\} \quad (3.75)$$

where  $b_0^2 = b_1 b_2$ .

### 3.2.8 Evaluation of $E_{\phi_{12}}$

$E_{\phi_{12}}$  has the same source distribution as  $E_{\phi_{22}}$  on one

hand, and the same distance  $R_n$  as  $E_{\phi_{21}}$  on the other hand. Hence its expression will contain the same "multiplying" factor as  $E_{\phi_{22}}$ , and the same "series" factor as  $E_{\phi_{21}}$ . Thus,

$$E_{\phi_{12}} = \frac{jA_2 \eta_o K b_2 \cos m\phi}{d} \sum_n \left\{ \left( \frac{m\beta_n}{K b_o \gamma_n} \right)^2 I_m(\gamma_n b_1) K_m(\gamma_n b_2) + I'_m(\gamma_n b_1) K'_m(\gamma_n b_2) \right\} \quad (3.61)$$

### 3.2.9 Dispersion relation

The total field  $E_{\phi_1}$  at point  $P_1$  is equal to  $(E_{\phi_{11}} + E_{\phi_{12}})$ . Also, the total field  $E_{\phi_2}$  at point  $P_2$  is equal to  $(E_{\phi_{22}} + E_{\phi_{21}})$ . Setting  $E_{\phi_1} = E_{\phi_2} = 0$  for all values of  $\phi$  yields the following two simultaneous equations for the unknown current amplitudes.

$$b_1 A_1 \cos m\phi (T_{11}) + b_2 A_2 \cos m\phi (T_{12}) = 0 \quad (3.62a)$$

$$b_1 A_1 \cos m\phi (T_{12}) + b_2 A_2 \cos m\phi (T_{22}) = 0 \quad (3.62b)$$

where

$$T_{11} = \sum_n \left[ \left( \frac{m\beta_n}{K b_1 \gamma_n} \right)^2 I_m(\gamma_n b_1) K_m(\gamma_n b_1) + I'_m(\gamma_n b_1) K'_m(\gamma_n b_1) \right] S(2\gamma_n a_1) \quad (3.63a)$$

$$T_{22} = \sum_n \left[ \left( \frac{m\beta_n}{Kb_2\gamma_n} \right)^2 I_m(\gamma_n b_2) K_m(\gamma_n b_2) + I'_m(\gamma_n b_2) K'_m(\gamma_n b_2) \right] s(2\gamma_n a_2) \quad (3.63b)$$

$$T_{12} = \sum_n \left[ \left( \frac{m\beta_n}{Kb_0\gamma_n} \right)^2 I_m(\gamma_n b_1) K_m(\gamma_n b_2) + I'_m(\gamma_n b_1) K'_m(\gamma_n b_2) \right] \quad (3.63c)$$

For a nontrivial solution, the determinant of the coefficients in (3.62) must be zero; namely

$$T_{11}T_{22} - T_{12}^2 = 0 \quad (3.64)$$

Equation (3.64) is the required dispersion relation whose solution yields the propagation constant of the wave.

From Equation (3.62a), the ratio of the current amplitudes may be determined as

$$\frac{A_1}{A_2} = - \left( \frac{b_2}{b_1} \right) \left( \frac{T_{12}}{T_{11}} \right) \quad (3.65)$$

### 3.3 NUMERICAL EVALUATION OF PHASE VELOCITY

A computer program that determines a numerical solution of equation (3.64) for the phase velocity, has been developed. At the start of the program, the parameters  $m$ ,  $a_1/b_1$ ,  $a_2/a_1$ ,  $d/b_1$ , and  $b_2/b_1$  are given specific

values. A calculation cycle is activated by selecting a frequency  $Kb_1$ . The phase delay  $\phi = \beta d$  is varied in increments of 0.1 throughout the visible range [24].

$$Kd < \phi < \pi \quad (3.66)$$

The determinant  $(T_{11} T_{22} - T_{12}^2)$  is evaluated at each increment in  $\phi$ . If at some increment the determinant undergoes a change in sign, a solution region is thus identified. The interval-halving technique is then applied to this region, and a phase delay  $\phi_s$  is resolved at the solution point. The normalized phase velocity  $[v/c = (Kb_1)(d/b_1)/\phi]$  and current ratio  $A_1/A_2$  corresponding to  $\phi_s$  are determined, and the result recorded.

If, on the other hand, the determinant does not experience a change in sign at any point in the visible range of  $\phi$ , the frequency  $Kb_1$  is said to be in a cutoff or stopband region of the structure. In any case, another frequency is selected and the calculation cycle is repeated until all the passbands are identified.

In order to speed-up convergence in evaluating the series  $T_{11}$  and  $T_{22}$ , the following relations are used.

$$T_{11} = a_0 + \sum_{n=1}^{20} (a_n - b_n) + \sum_{n=1}^{20} (a_{-n} - b_n) + 2 \sum_{n=1}^{\infty} b_n \quad (3.67a)$$

$$T_{22} = c_0 + \sum_{n=1}^{20} (c_n - d_n) + \sum_{n=1}^{20} (c_{-n} - d_{-n}) + 2 \sum_{n=1}^{\infty} d_n \quad (3.67b)$$

where  $a_n$  and  $c_n$  are given by

$$a_n = \left[ \left( \frac{m\beta_n}{Kb_1\gamma_n} \right)^2 I_m(\gamma_n b_1) K_m(\gamma_n b_1) + I'_m(\gamma_n b_1) K'_m(\gamma_n b_1) \right] S(2\gamma_n a_1) \quad (3.68a)$$

$$c_n = \left[ \left( \frac{m\beta_n}{Kb_2\gamma_n} \right)^2 I_m(\gamma_n b_2) K_m(\gamma_n b_2) + I'_m(\gamma_n b_2) K'_m(\gamma_n b_2) \right] S(2\gamma_n a_2) \quad (3.68b)$$

while  $b_n$  and  $d_n$  are the asymptotic values of  $a_n$  and  $c_n$  respectively when  $n$  is very large, in the sense that  $a_n/b_n \rightarrow c_n/d_n \rightarrow 1$  as  $n \rightarrow \infty$ . Also, the infinite series  $\sum_{n=1}^{\infty} b_n$  and  $\sum_{n=1}^{\infty} d_n$  may be determined exactly. The expressions for  $b_n$  and  $d_n$  along with the evaluation of their infinite series  $\sum_{n=1}^{\infty} b_n$  and  $\sum_{n=1}^{\infty} d_n$  are given in Appendix B.

Since the terms in the series  $T_{12}$  decay as  $e^{-pn}/n$  for large  $n$ , the evaluation technique of (3.67) is not necessary in this case. The exponential decay in  $T_{12}$  is demonstrated in Appendix C.

The phase velocity and the ratio of current amplitudes in the  $m=1$  case are given in Tables IX-X for two ratios of loop radii, and for three spacings of array elements. The dual-velocity band has been left out from Tables IX and X; however, it is shown expanded when the phase velocity data is plotted in Figs. 3.3 and 3.4.

TABLE IX

Normalized phase velocity of  $m=1$  mode ( $a/b_1=0.01$ ,  $b_2/b_1=1.25$ )

$Kb_1$	$d/b_1=0.25$		$d/b_1=0.50$		$d/b_1=1.00$	
	$v/c$	$A_1/A_2$	$v/c$	$A_1/A_2$	$v/c$	$A_1/A_2$
0.50	0.987	0.034	0.992	0.203	0.997	0.286
0.52	0.981	0.036	0.988	0.182	0.996	0.276
0.54	0.974	0.017	0.983	0.170	0.993	0.275
0.56	0.965	0.016	0.976	0.142	0.989	0.250
0.58	0.954	-0.004	0.967	0.124	0.984	0.236
0.60	0.940	-0.026	0.957	0.109	0.978	0.220
0.62	0.925	-0.045	0.944	0.089	0.970	0.197
0.64	0.906	-0.065	0.928	0.063	0.958	0.169
0.66	0.884	-0.091	0.909	0.036	0.944	0.143
0.68	0.857	-0.120	0.886	0.008	0.927	0.111
0.70	0.826	-0.150	0.858	-0.026	0.904	0.076
0.71	0.807	-0.168	0.842	-0.044	0.890	0.057
0.72	0.787	-0.185	0.824	-0.063	0.875	0.036
0.73	0.764	-0.203	0.803	-0.084	0.857	0.014
0.74	0.738	-0.221	0.780	-0.105	0.835	-0.009
0.75	0.707	-0.240	0.752	-0.128	0.810	-0.035
0.76	0.670	-0.260	0.719	-0.151	0.779	-0.061
0.77	0.625	-0.278	0.679	-0.175	0.741	-0.089
0.78	0.565	-0.292	0.626	-0.198	0.689	-0.118
0.79	0.478	-0.295	0.551	-0.216	0.613	-0.147
0.80	0.278	-0.211	0.394	-0.201	0.448	-0.161
0.95	0.975	-1.407	0.942	-1.599	0.949	-1.793
0.96	0.925	-1.550	0.890	-1.823	0.904	-2.106
0.97	0.871	-1.723	0.837	-2.098	0.853	-2.508
0.98	0.818	-1.924	0.781	-2.448	0.796	-3.042
0.99	0.762	-2.175	0.719	-2.922	0.729	-3.808
1.00	0.701	-2.501	0.646	-3.635	0.640	-5.063

TABLE X

Normalized phase velocity of  $m=1$  mode ( $a/b_1=0.01$ ,  $b_2/b_1=1.50$ )

$Kb_1$	$d/b_1=0.25$		$d/b_1=0.50$		$d/b_1=1.00$	
	$v/c$	$A_1/A_2$	$v/c$	$A_1/A_2$	$v/c$	$A_1/A_2$
0.42	0.986	-0.000	0.991	0.080	0.997	0.173
0.44	0.978	-0.016	0.985	0.066	0.994	0.151
0.46	0.968	-0.030	0.977	0.046	0.990	0.135
0.48	0.954	-0.048	0.967	0.036	0.984	0.122
0.50	0.939	-0.057	0.954	0.021	0.975	0.104
0.52	0.918	-0.078	0.937	0.001	0.963	0.085
0.54	0.894	-0.093	0.916	-0.017	0.948	0.065
0.56	0.864	-0.114	0.890	-0.039	0.927	0.042
0.57	0.847	-0.124	0.874	-0.051	0.915	0.030
0.58	0.828	-0.136	0.857	-0.063	0.900	0.017
0.59	0.806	-0.147	0.837	-0.076	0.883	0.003
0.60	0.782	-0.159	0.815	-0.088	0.863	-0.011
0.61	0.754	-0.171	0.789	-0.102	0.840	-0.026
0.62	0.722	-0.183	0.759	-0.115	0.812	-0.042
0.63	0.684	-0.194	0.723	-0.129	0.778	-0.058
0.64	0.638	-0.203	0.679	-0.142	0.735	-0.074
0.65	0.578	-0.210	0.621	-0.153	0.678	-0.090
0.66	0.492	-0.206	0.538	-0.158	0.592	-0.102
0.91	0.992	-1.684	0.988	-1.791	0.993	-1.906
0.92	0.967	-1.836	0.963	-1.987	0.976	-2.153
0.93	0.934	-2.011	0.933	-2.206	0.952	-2.442
0.94	0.901	-2.199	0.899	-2.463	0.923	-2.790
0.95	0.865	-2.416	0.863	-2.764	0.890	-3.212
0.96	0.827	-2.678	0.825	-3.130	0.853	-3.745
0.97	0.788	-2.981	0.783	-3.587	0.810	-4.435
0.98	0.745	-3.355	0.736	-4.192	0.759	-5.398
0.99	0.696	-3.852	0.680	-5.039	0.696	-6.867
1.00	0.639	-4.540	0.608	-6.442	0.607	-9.566

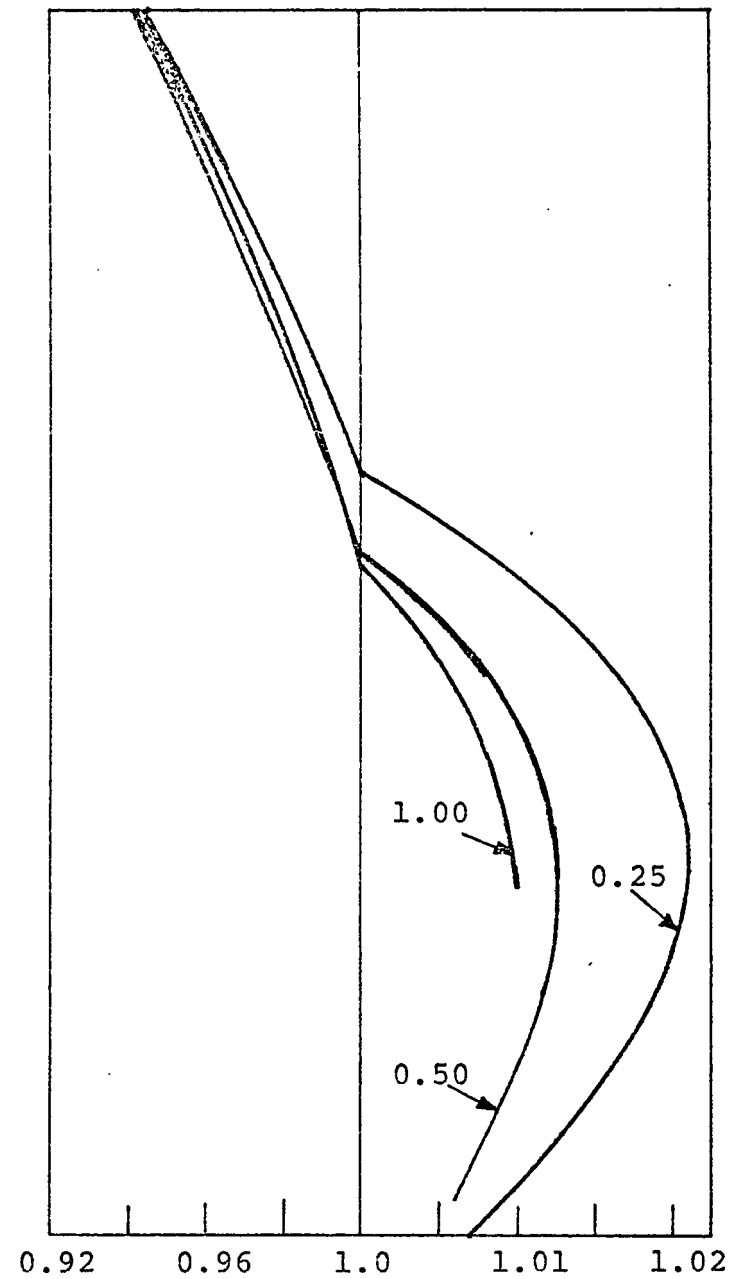
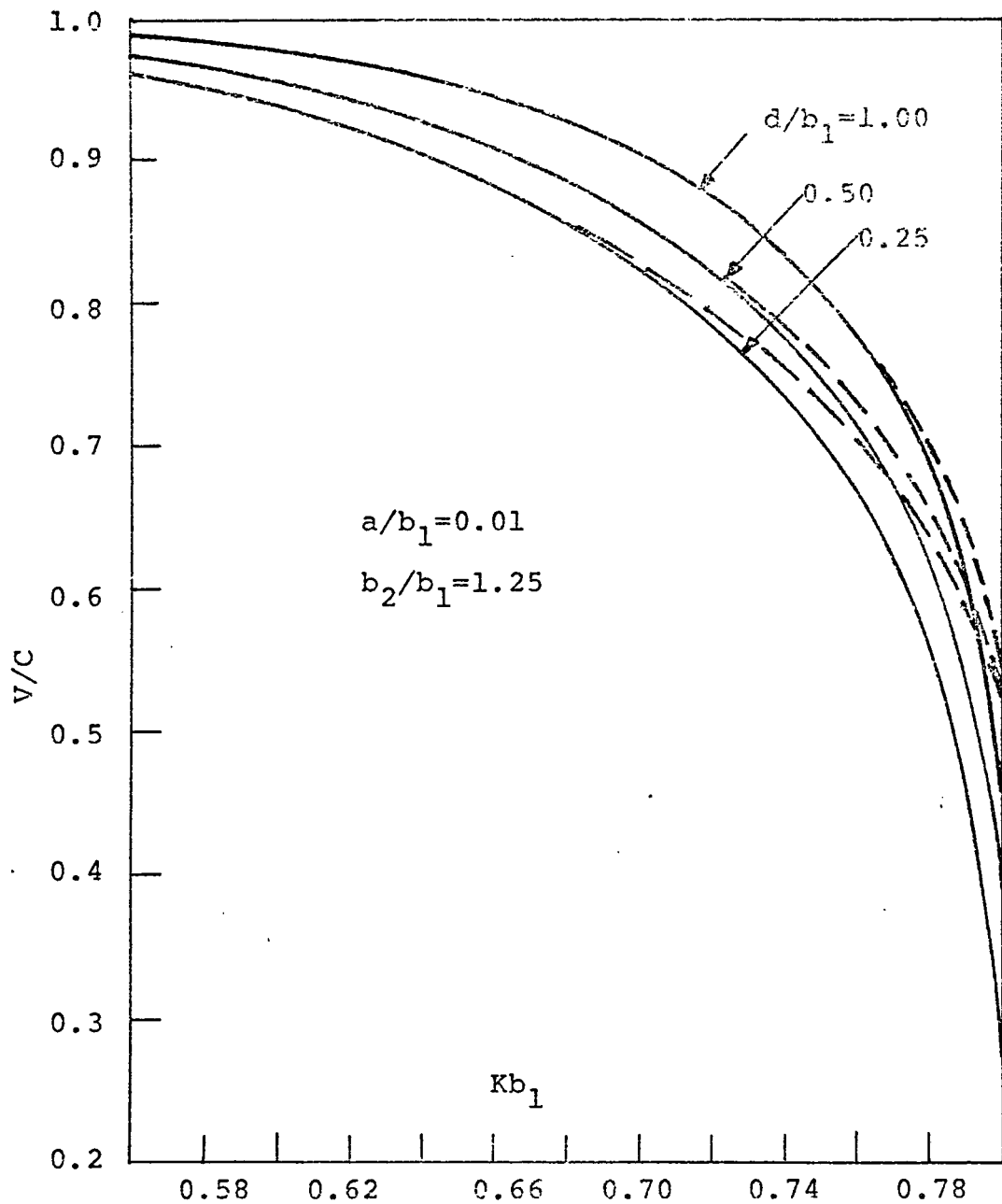


Fig. 3.3 Phase velocity of propagating waves on the concentric array.  
 (Curves for the isolated array are shown dashed)

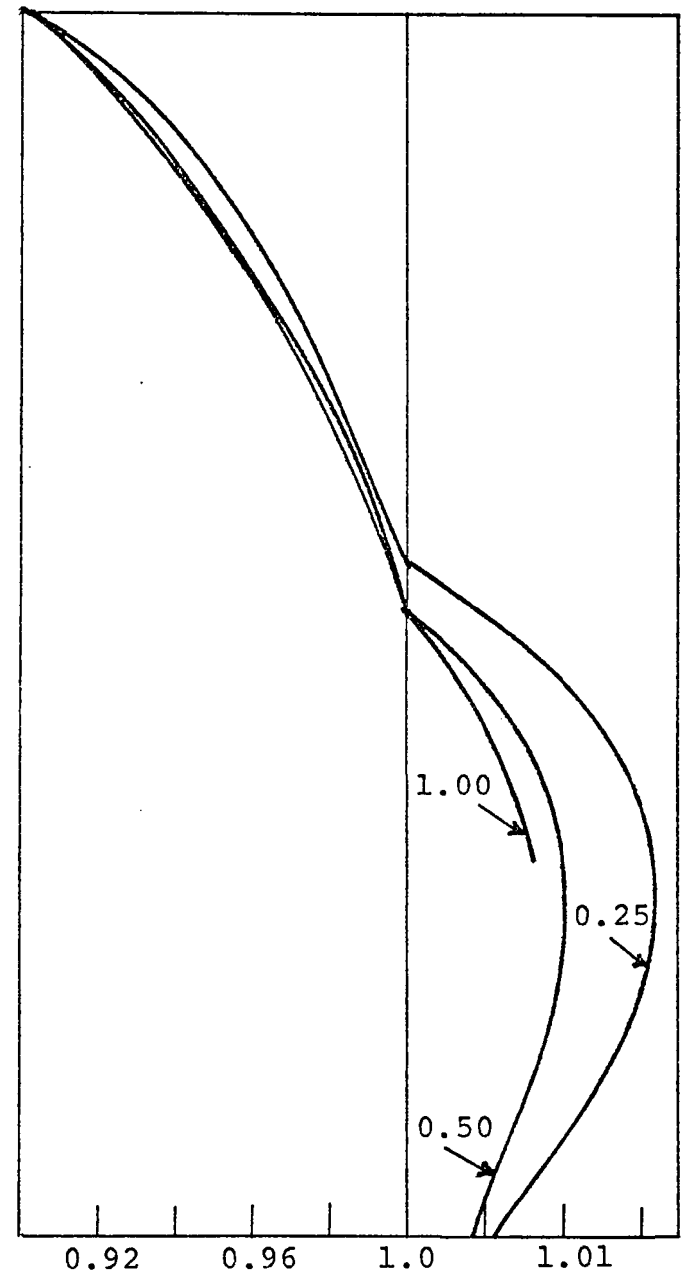
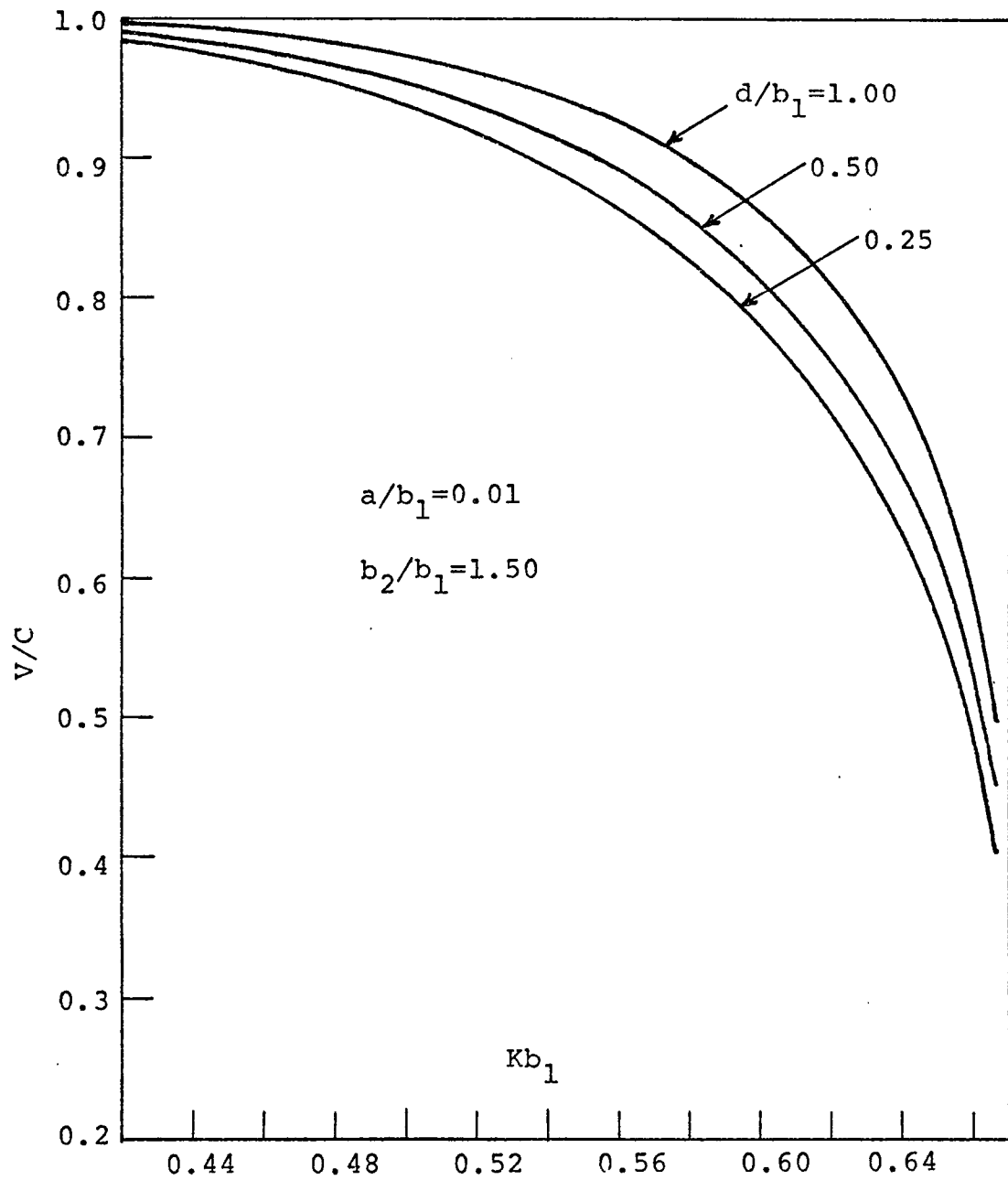


Fig. 3.4 Phase velocity of propagating waves on the concentric array.

As seen from these figures, the concentric array of loops exhibits two disjoint passbands separated by a stopband region. The first passband corresponds to the near resonance of the outer loop ( $Kb_2 \leq 1.0$ ), while the second passband corresponds to the near resonance of the inner loop ( $Kb_1 \leq 1.0$ ). The bandwidth of the first passband is approximately equal to that of an isolated array having the outer loops only as elements, divided by  $b_2/b_1$ . Moreover, the phase velocity curve presents the same type of decrease with spacing as seen in the case of the isolated array, except that it becomes slightly more dispersive as it approaches cutoff.

The stopband region, located between the two passbands, and the second passband have bandwidths that are nonlinear functions of the ratio  $b_2/b_1$ . For instance, a decrease in the ratio  $b_2/b_1$  is accompanied by a corresponding decrease in the widths of these two bands. Also, in the second passband, the phase velocity curve exhibits a low dispersion characteristic and an obvious insensitivity to the spacing between the loops.

In the first passband, the outer loop carries a minimum of five times the current on the inner loop; however, in the second passband, the current on the inner loop is at least 1.5 times that of the outer loop. Also, the currents on the two concentric loops are  $180^\circ$  out of phase

over the two bands, except for a small range at the low end of the first band. This range becomes even smaller if the axial spacing  $Kd$  decreases with fixed transverse spacing  $K(b_2 - b_1)$ ; or, if the transverse spacing increases for fixed axial spacing.

Finally, a discussion of the dual-velocity band is deferred until section 3.5 where a detailed analysis will be given.

#### 3.4 LOWER CUTOFF FREQUENCIES

The phase velocity curves of Figs. 3.3 and 3.4 show an asymptotic approach towards unity on the low end of the first passband, and an abrupt intersection with unity on the low end of the second passband. In fact, the low cutoff frequency of the first passband is theoretically zero. However, in practice it is limited by the difficulty to excite a slow-wave that has a phase velocity very close to the speed of light. On the other hand, the low cutoff frequency of the second passband is very sharp, indicating a fast transition from a radiating structure to a surface-wave structure at some well defined frequency.

In this section, a semi-analytic procedure is devised for the purpose of determining the exact value of the lower cutoff frequency of the second passband. Also, the

asymptotic behavior at the low end of the first passband is verified with some accuracy. This objective is achieved by evaluating the dispersion relation in the limit as  $\beta \rightarrow K$  or equivalently, as  $v/c \rightarrow 1$ . Since the zero-order term in the series  $T_{11}$ ,  $T_{22}$ , and  $T_{12}$  is the dominant term, it follows that all other terms are negligible in the limit as  $\beta \rightarrow K$ . Hence, defining  $x = \gamma b_1$  and  $\alpha = b_2/b_1$ , the expressions for  $T_{11}$ ,  $T_{22}$  and  $T_{12}$  for the  $m=1$  mode are simplified as follows

$$T_{11} = \left[ \left( \frac{\beta}{K} \right)^2 \frac{I_1(x) K_1(x)}{x^2} + I_1'(x) K_1'(x) \right] S\left(2 \frac{a_1}{b_1} x\right) \quad (3.69a)$$

$$T_{22} = \left[ \left( \frac{\beta}{K} \right)^2 \frac{I_1(\alpha x) K_1(\alpha x)}{(\alpha x)^2} + I_1'(\alpha x) K_1'(\alpha x) \right] S\left(2 \frac{a_2}{b_1} x\right) \quad (3.69b)$$

$$T_{12} = \left( \frac{\beta}{K} \right)^2 \frac{I_1(x) K_1(\alpha x)}{(\alpha x)^2} + I_1'(x) K_1'(\alpha x) \quad (3.69c)$$

where

$$x = \gamma b_1 = b_1 \sqrt{\beta^2 - K^2} \quad (3.70)$$

From (3.70), it is seen that as  $\beta$  approaches  $K$ ,  $x$  approaches zero. Therefore, a small argument approximation may be applied to the functions of equations (3.69) to yield limiting forms for  $T_{11}$ ,  $T_{22}$ , and  $T_{12}$ . From these a simplified dispersion relation may be obtained.

The limiting form of the Struve function is given by [54]

$$\lim_{x \rightarrow 0} S(x) = 1.0 \quad (3.71)$$

The ratio  $\beta/K$  may be evaluated in terms of  $x$  by making use of equation (3.70). This yields

$$\left(\frac{\beta}{K}\right)^2 = 1 + \frac{x^2}{(Kb_1)^2} \quad (3.72)$$

Using (3.71) and (3.72) in (3.69), it follows that

$$T_{11} = \left[1 + \frac{x^2}{(Kb_1)^2}\right] \left[ \frac{I_1(x) K_1(x)}{x^2} \right] + I_1'(x) K_1'(x) \quad (3.73a)$$

$$T_{22} = \left[1 + \frac{(\alpha x)^2}{(Kb_2)^2}\right] \left[ \frac{I_1(\alpha x) K_1(\alpha x)}{(\alpha x)^2} \right] + I_1'(\alpha x) K_1'(\alpha x) \quad (3.73b)$$

$$T_{12} = \left[1 + \frac{x^2}{(Kb_1)^2}\right] \left[ \frac{I_1(x) K_1(\alpha x)}{\alpha x^2} \right] + I_1'(x) K_1'(\alpha x) \quad (3.73c)$$

From page 375 of reference [54], the following series representations of  $I_1(x)$  and  $K_1(x)$  for small argument  $x$ , are given.

$$I_1(x) = \frac{x}{2} \sum_{K=0}^{\infty} \frac{(x^2/4)^K}{K! \Gamma(K+2)} \quad (3.74)$$

$$K_1(x) = \frac{1}{x} + I_1(x) \ln\left(\frac{x}{2}\right) - \frac{x}{4} \sum_{K=0}^{\infty} \{\psi(K+1) + \psi(K+2)\} \frac{(x^2/4)^K}{K!(K+1)!} \quad (3.75)$$

where  $\psi(n) = -\gamma + \sum_{K=1}^{n-1} K^{-1}$  and  $\gamma = 0.5772\dots$  is the Euler's constant. Taking only the leading terms of the series in (3.74) and (3.75), and then differentiating the results, yields

$$I_1(x) \approx \frac{x}{2} + \frac{x^3}{16} \quad (3.76a)$$

$$K_1(x) \approx \frac{1}{x} + \frac{x}{2} \ln\left(\frac{x}{2}\right) + \frac{x^3}{16} \ln\left(\frac{x}{2}\right) + 0.0386x - 0.042x^3 \quad (3.76b)$$

$$I_1'(x) \approx \frac{1}{2} + \frac{3}{16} x^2 \quad (3.76c)$$

$$K_1'(x) \approx -\frac{1}{x^2} + 0.5386 + \frac{1}{2} \ln\left(\frac{x}{2}\right) + \frac{3x^2}{16} \ln\left(\frac{x}{2}\right) - 0.06365x^2 \quad (3.76d)$$

By substituting (3.76) back into (3.73), combining terms, and neglecting those terms of order higher than  $x$ , one obtains

$$T_{11} = 0.1636 + \frac{1}{2} \ln\left(\frac{x}{2}\right) + \frac{1}{2(Kb_1)^2} \quad (3.77a)$$

$$T_{22} = 0.1636 + \frac{1}{2} \ln\left(\frac{\alpha x}{2}\right) + \frac{1}{2\alpha^2(Kb_1)^2} \quad (3.77b)$$

$$T_{12} = 0.2886 - \frac{1}{8\alpha^2} + \frac{1}{2} \ln \left( \frac{\alpha x}{2} \right) + \frac{1}{2\alpha^2 (Kb_1)^2} \quad (3.77c)$$

Define  $F = (1/2) \ln(x/2)$ . Evaluating the determinant  $T_{11}T_{22} - (T_{12})^2$ , setting the result equal to zero, and solving for  $F$ , yields

$$F = \frac{(q^2 - s^2 - t^2 - u^2) + (qs + qu + qr + rs + ru) - 2(tu + st + su)}{(s + u + 2t - 2q - r)} \quad (3.78)$$

where

$$q = 0.1636$$

$$r = \frac{1}{2(Kb_1)^2}$$

$$s = \frac{1}{2\alpha^2 (Kb_1)^2}$$

$$t = 0.2886 - \frac{1}{8\alpha^2}$$

$$u = \frac{1}{2} \ln(\alpha)$$

Solving for  $x$  in terms of  $F$  gives the result

$$x = 2 e^{2F} \quad (3.79)$$

Low-frequency cutoff may now be determined with the help of (3.78) and (3.79). At cutoff,  $\beta$  is equal to  $K$ ; or, equivalently  $x$  is equal to zero. From (3.79), this requires that  $F$  be a negative infinite number ( $F = -\infty$ ).

This also means that the denominator in (3.78) must be zero. That is,

$$s+u+2t-2q-r=0 \quad (3.80)$$

Equation (3.80) involves only  $\alpha$  and  $Kb_1$  as variables. Hence, for a given  $\alpha$ , the lower cutoff frequency is obtained from the solution of (3.80) for  $Kb_1$ . This yields

$$Kb_1 = \left[ \frac{2}{1 - \left( \frac{2\alpha^2}{1-\alpha^2} \right) \ell n \alpha} \right]^{\frac{1}{2}} \quad (3.81)$$

For instance, when  $\alpha$  equals 1.25,  $Kb_1$  is found to be equal to 0.945; and when  $\alpha$  is 1.50,  $Kb_1$  is 0.90. These values fall within 0.5% of the cutoff frequencies indicated by Figs. 3.3 and 3.4.

A plot of the function  $F$  versus frequency for  $\alpha=1.25$  is shown in Fig. 3.5. The gradual decrease at low frequency indicates a phase velocity asymptotically approaching speed of light. On the other hand, the singularity at  $Kb_1=0.945$  indicates a phase velocity that is exactly equal to the speed light.

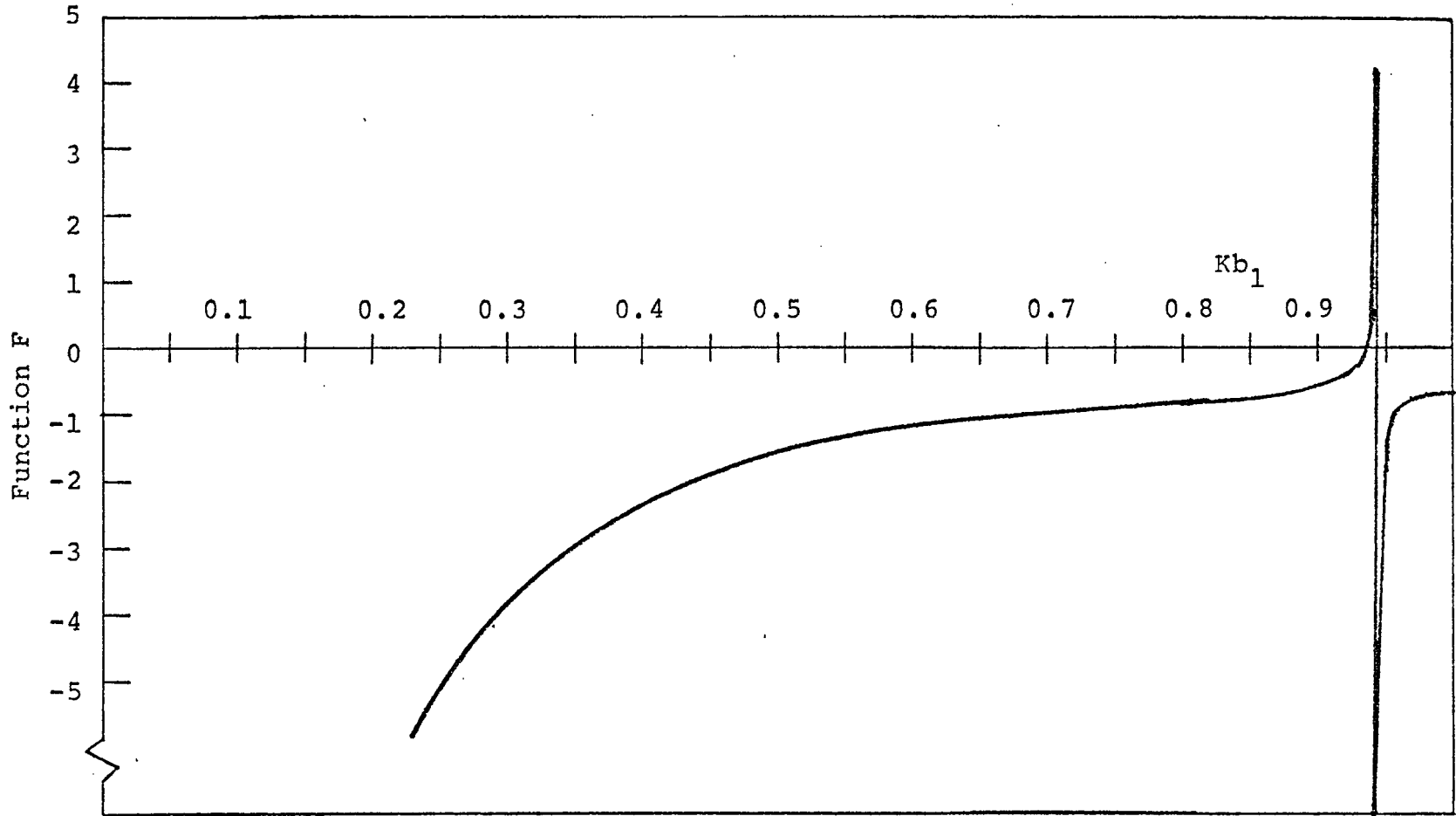


Fig. 3.5 Variation of F versus frequency ( $\alpha=1.25$ ).

### 3.5 ANALYSIS OF THE ANOMALOUS BAND

The most general definition of cutoff that is applicable to all periodic structures regardless of the physical apparatus of such structures may be based on a theorem derived by Bell [50]. The theorem states that the time-average power flow in the pass bands of the periodic structure is equal to the group velocity times the time-average electrical, and magnetic stored energy per period divided by the period. Mathematically speaking, this may be translated as

$$\frac{1}{2} \operatorname{Re} \left\{ \int_{\mathbf{s}} \vec{\mathbf{E}} \times \vec{\mathbf{H}}^* \cdot d\vec{\mathbf{s}} \right\} = \frac{v_g}{d} \int_V \left( \frac{1}{4} \epsilon \vec{\mathbf{E}} \cdot \vec{\mathbf{E}}^* + \frac{1}{4} \mu \vec{\mathbf{H}} \cdot \vec{\mathbf{H}}^* \right) dV \quad (3.82)$$

where

$\mathbf{s}$  is an infinite surface normal to the axis of the structure;

$V$  is the volume enclosed by two such surfaces forming the boundaries of one period;

$v_g = d\omega/d\beta$  is the group velocity; and,

$d$  = the period of the structure.

In general, cutoff may be defined as the frequency at which forward power flow vanishes. Equivalently, this may also be termed as the point at which the group velocity goes

to zero. From the definition of group velocity  $v_g = d\omega/d\beta = cdK/d\beta$ , an expression for the slope of the phase velocity curve (Figs. 3.3 and 3.4) in terms of phase velocity and group velocity may be derived as

$$\text{Slope} = \frac{(v/c)}{Kb_1} \left[ 1 - \frac{v}{v_g} \right] \quad (3.83)$$

Using (3.83), it is possible to carry the definition of cutoff one step further and describe it as the point at which the slope of the phase velocity curve becomes equal to  $-\infty$ .

The actual realization of cutoff (ceasing of forward power flow) may be achieved by one of two physical phenomena. First, cutoff occurs if the interelement distance  $d$  becomes one half of the guided wavelength. In this case, the field reverses from one section to the next and meaningful propagation comes to a halt. This phenomenon will be referred to as "axial resonance" due to its dependence on the axial distance  $d$ . The phenomenon of "axial resonance" is widely accepted and assumed to be the sole contributor to propagation cutoff in periodic structures. However, if cutoff is to occur because of "axial resonance", the structure must possess a moderately high degree of dispersion in order to satisfy the require-

ment of zero group velocity at cutoff. The high dispersion property, in turn, puts a limitation on the type of elements and their spacing.

The case of the periodic array of single loops will be examined first. As the spacing  $d$  is decreased, the periodic structure becomes steadily less dispersive. In other words, the group velocity begins to change less rapidly as a function of frequency. As a result, the usual cutoff due to "axial resonance" cannot take place. A new type of cutoff occurs when the equivalent loading vanishes ( $X=0$ ). This phenomenon may be termed "transverse resonance" due to the transverse loading presented by the elements on a periodically loaded transmission line model of the array.

It should be noted here that cutoff brought about by "axial resonance" occurs when the array elements reach resonant lengths, or soon thereafter, and involves the propagation cutoff of a single wave by decreasing its group velocity to zero. On the other hand, cutoff dictated by "transverse resonance" occurs at a frequency higher than that at which the array elements attain resonant lengths. Also, the latter cutoff forms the end of propagation for two waves of unequal phase velocities. The "primary" wave (larger phase velocity) has its phase and

group velocities in the same direction. The "secondary" wave (lower phase velocity) has its phase and group velocities oppositely directed. Thus, the "secondary" wave acts to diminish the forward power flow of the "primary" wave and reduce it eventually to zero.

Next, the behavior of the concentric array of loops is explained in the light of the theory developed thusfar. Consider first the case where the ratio  $b_2/b_1$  is small (Fig. 3.3). In the first passband, the structure is seen to be highly dispersive even at small spacings. As a result, the dual-wave behavior in this passband is practically nonexistent, and cutoff occurs almost exactly at  $Kb_2=1.0$ . In the second passband, the structure is seen to possess low dispersion even at large spacings. Therefore, the dual-wave band is increased by a factor of two over that of the isolated array.

When the ratio  $b_2/b_1$  is increased, the coupling between the inner and outer loops is reduced. Thus, the first passband will increase its dual-wave region, while the second passband will reduce it. Finally, when the inner and outer loops become completely uncoupled, each passband reduces to that of an isolated array.

In order to dramatize the effect of reduced spacing on the creation of the dual-wave phenomenon, contour diagrams of phase velocity versus spacing with the frequency

as a parameter are shown in Figs. 3.6 and 3.7. Note the near absence of dual waves in the first passband depicted in Fig. 3.6. In contrast, note the excitation of dual waves over a relatively large band in the second passband depicted in Fig. 3.7. Finally, contour diagrams for the isolated array are given in Fig. 3.8 for the purpose of comparison with those of the concentric array.

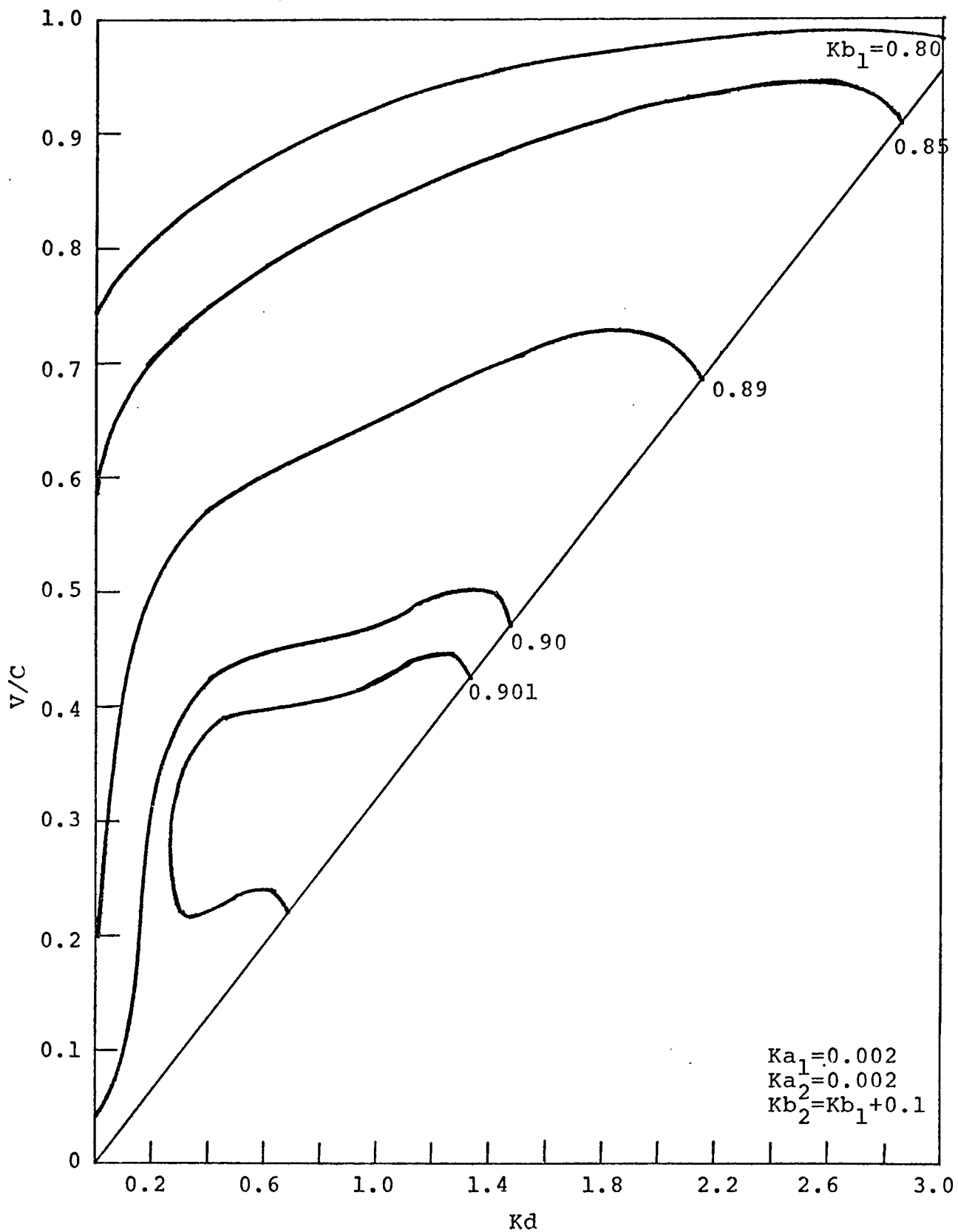


Fig. 3.6 Contour diagram showing phase velocity versus spacing near cutoff of the first band.

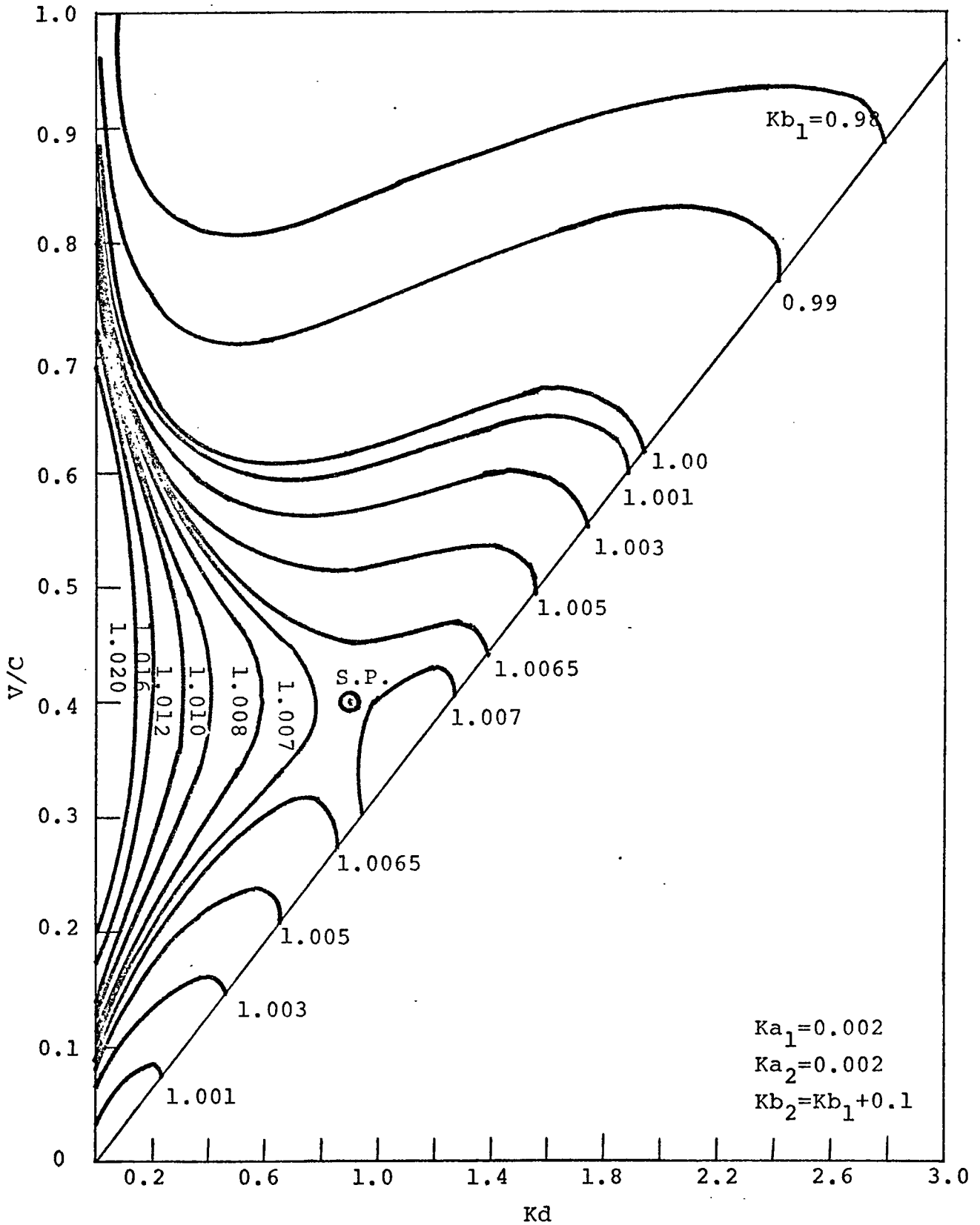


Fig. 3.7 Contour diagram showing phase velocity versus spacing near cutoff of the second band.

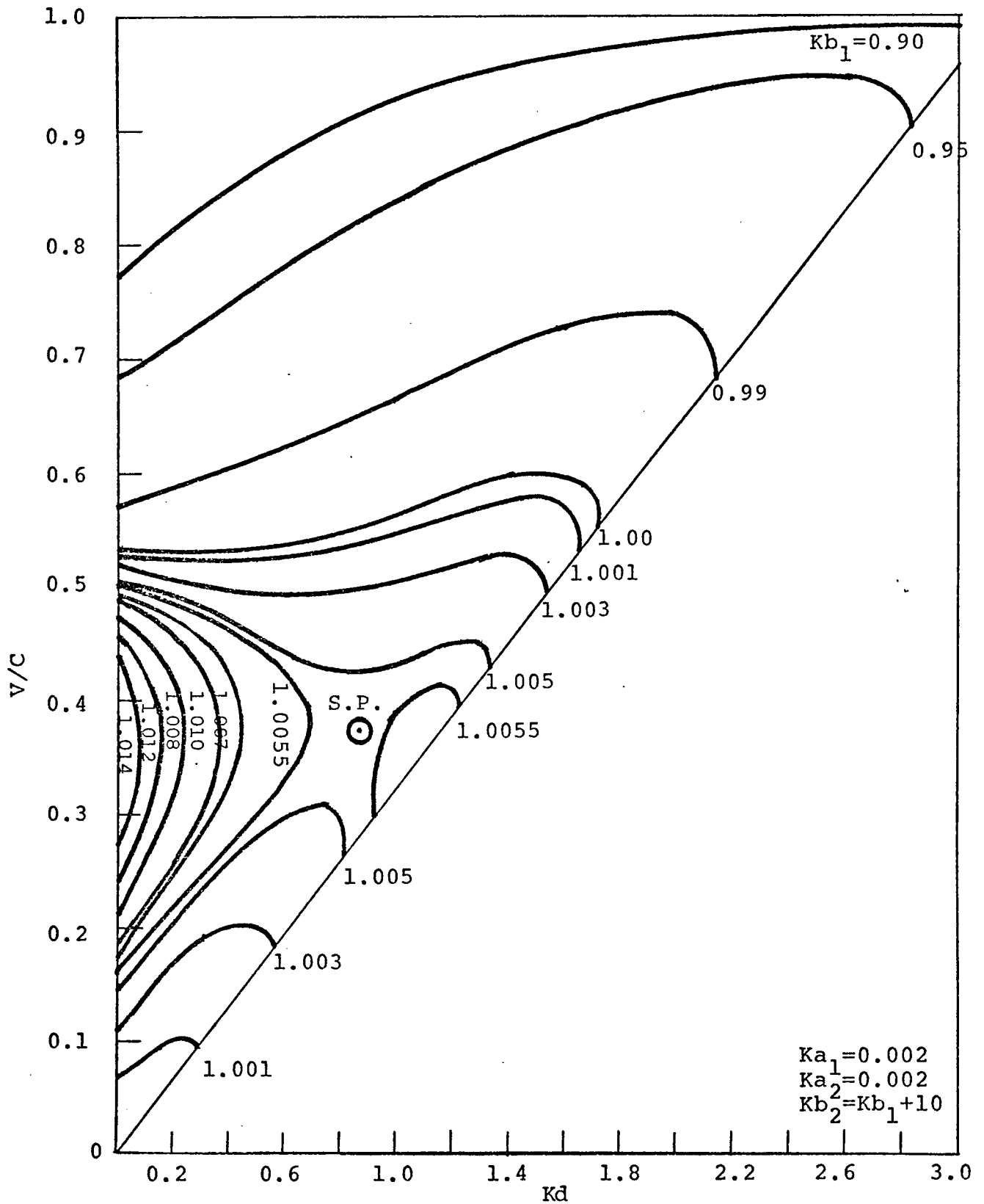


Fig. 3.8 Contour diagram showing phase velocity versus spacing near cutoff of the isolated array.

## CHAPTER 4

THE INFINITELY LONG YAGI ARRAY  
OF CONCENTRIC LOOPS--EXPERIMENT

## 4.1 EXPERIMENTAL OBJECTIVES

The experiment described in this chapter has a three-fold purpose. First, propagating waves are excited in two distinct passbands on the periodic structure of concentric circular loops. Using the surface-wave resonator method, the phase velocities are measured and compared with theoretically determined values. Second, propagation characteristics are examined in the light of measured amplitude and phase patterns at representative frequencies in the pass- and stop-bands. Third, a data fitting program is developed and used to ascertain the presence or absence of dual waves. Near-field data corresponding to resonant frequencies near the end of the second passband are matched and results given.

## 4.2 DESCRIPTION OF EXPERIMENTAL SET-UP

A block diagram of the experimental set-up is shown in Fig. 4.1. Part of the CW signal from the generator was used to drive the electronic frequency counter. The

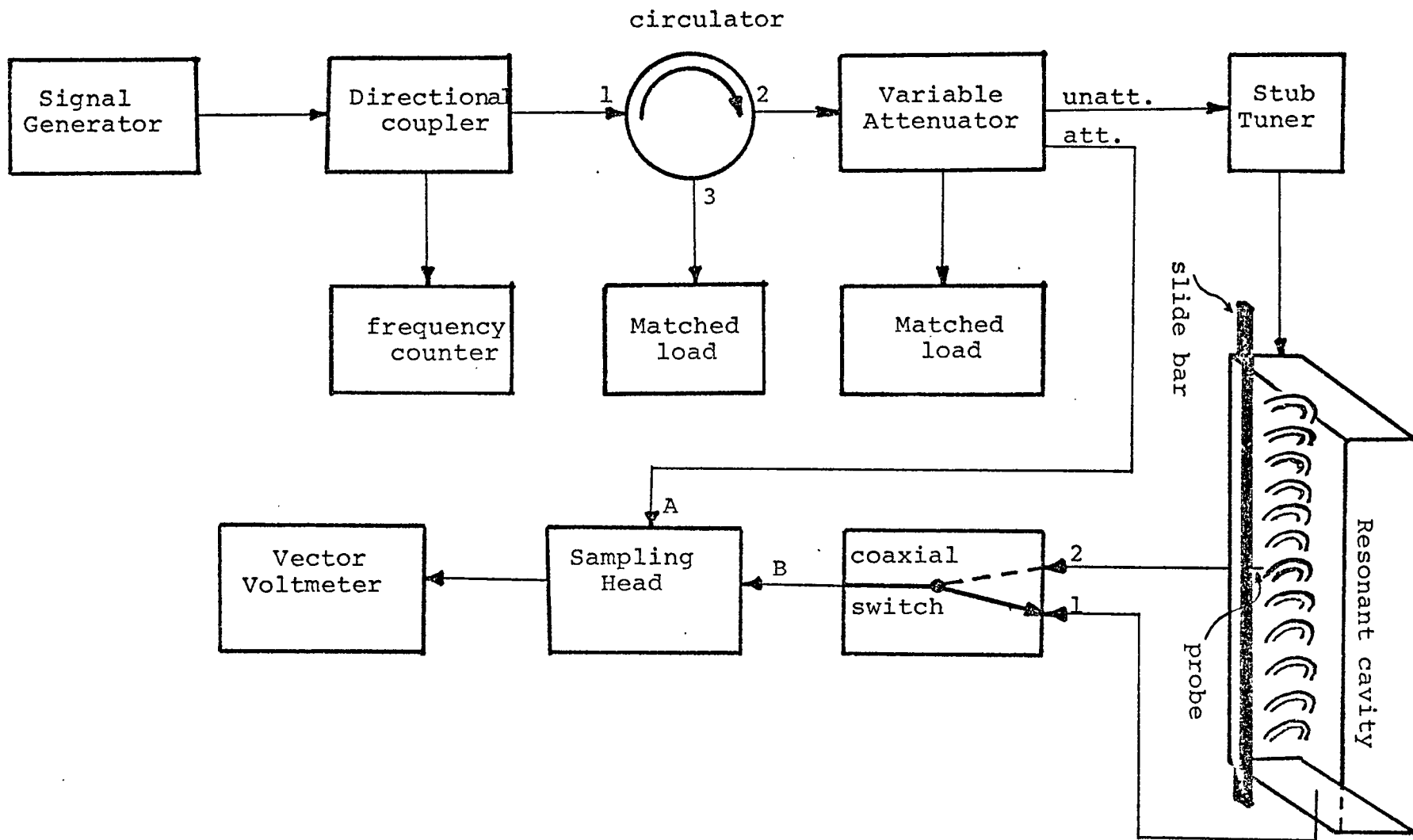


Fig. 4.1 Experimental set-up.

main signal from the directional coupler continued through the circulator which was necessary to prevent reflected waves from reaching the generator or the frequency counter. Past the circulator, the signal was fed to the input of a variable attenuator. The "unattenuated" output was passed through a single-stub tuner to the exciter of the open resonant cavity. The "attenuated" output provided the "reference" signal fed to channel "A" of the sampling head. The coaxial switch selected either the signal picked up by the probe alongside the array, or that of a receiving antenna mounted on the end reflector of the cavity. The signal chosen by the switch served as the "test" signal fed to channel "B" of the sampling head. Finally, the vector voltmeter displayed the amplitude of channel "A" or "B" and their phase difference ( $\phi_B - \phi_A$ ). Note that the isolation between the "attenuated" and "unattenuated" parts of the variable attenuator was maintained at better than 50 dB.

The component parts of the resonant cavity will now be described with some emphasis as to their function and type of construction. A pictorial view of the assembly is shown in Fig. 4.2.

#### 4.2.1 Ground Plane

By the theorem of images, a single conductor over



Fig. 4.2 The resonant cavity

an infinite, perfectly conducting ground plane produces fields identical to those of a single conductor and its image. If the conditions of a plane surface, perfect conductivity, and infinite extent are satisfactorily approximated for the ground plane, very good experimental results can be obtained by the image-plane technique. In addition to simplicity of construction, other advantages of the system are 1) that it is inherently balanced and thus a high degree of electrical symmetry results, and 2) the presence of the ground plane serves as an electrical shield to isolate operator and measuring equipment from the antenna under test [55].

The ground plane used in this investigation was made of 0.635 cm aluminum and measures 61 cm by 126.5 cm. This was of sufficient size over the frequency range of interest. It was made up of three plates, one center plate and two side plates. At the middle of the center plate and all along its length, concentric half-loops of diameters 4.127 cm and 6.667 cm were mounted with the aid of precisely-drilled close tolerance holes. The half-loops were made of circular copper wire of 0.159 cm diameter that was pulled through the holes and made to conform to the shape of a semi-circular steel pipe.

On one side of the center plate, a 0.792 cm strip

had been removed to accommodate a brass rod that carried the E-field probe. The brass rod, of length roughly twice that of the ground plane, was made to travel over two steel bars held in place by phenolic standoffs mounted on the back side of the ground plane. The small section of the two-section center plate (the one not containing the half-loops), adjacent to the brass rod, had been marked in intervals of 0.5 cm to designate the position of the E-field probe.

Finally, adjoining sides of each plate were machined down to half thickness and made to overlap. The overlapping sections were subsequently fastened together by means of 4-40 screws. Also, in order to provide a perfectly plane conducting surface, all seams, holes, and screw heads were filled with conducting silver paint and then carefully smoothed and polished.

#### 4.2.2 Reflector Plates

To form an open surface-wave resonator, two parallel and plane reflector plates were clamped, one on each end, to the image plane. The two plates were made of 0.635 cm aluminum and measured 30.5 cm in height and 61 cm in width. Also, in order to maintain precise boundary conditions, the reflectors were oriented normal to the image plane and smoothly flattened. Finally, the corners between each

reflector and the image plane were filled and sealed with silver conducting paint to insure good electrical conductivity.

#### 4.2.3 Exciter

Excitation of the surface-wave on the periodic structure was accomplished by means of a small square loop antenna mounted on the plane of the front reflector. The antenna was positioned in a vertical plane. Also, its largest dimension extended vertically a distance equal to the spacing between the concentric loops of the array. This is illustrated in Fig. 4.3. Based on near-field calculations of the array, the square loop so oriented served as a reasonably efficient exciter.

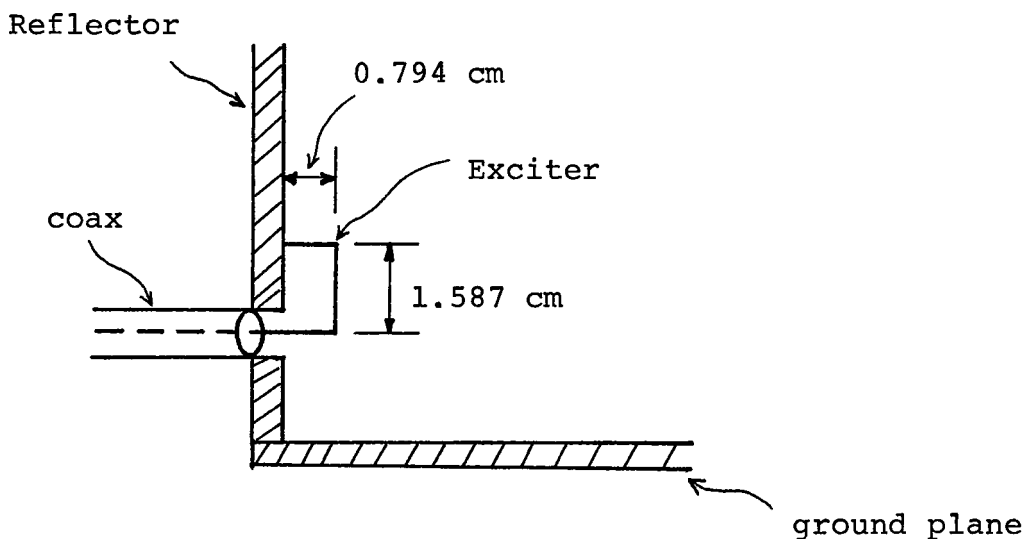


Fig. 4.3. Surface-wave exciter

It is noted that loose coupling to the cavity by the exciter was maintained by restricting the loop length to less than half-wavelength over the frequency range of interest (1-2.4 GHz). This would lead to better resolution in determining the resonant frequencies of the cavity [56]. A similar receiving antenna was attached to the back reflector, and used to monitor cavity resonance.

#### 4.2.4 E-field probe

The probe consisted of a simple extension of the center conductor of a miniature coaxial cable (diameter = 0.2 mm) protruding through a hole in the metal surface of the brass rod. It extended roughly 0.635 cm above the surface of the ground plane. As such, it measured the component of the electric field that was normal to the ground plane. The small size of the probe (less than  $0.1\lambda$ ) was necessary to insure the measurement of the field at a point [57].

### 4.3 PHASE VELOCITY MEASUREMENTS

The phase velocity of the guided wave was determined in the following manner. The coaxial switch was thrown in position 1 to connect the receiving antenna in the end-reflector to the sampling head of the vector voltmeter. Then, resonance of the cavity was obtained by varying the

signal generator frequency until a transmission maximum through the resonator was observed on channel B of the vector voltmeter. The distance between the resonator end plates was accurately measured, and was kept constant throughout the measurements. For every resonance observed, the free-space wavelength was obtained as the ratio of the speed of light to the frequency indicated by the frequency counter. The guided wavelength was determined by dividing the length of the cavity by one half the number of standing wave minima along the resonator axis. To count the number of minima, a cylindrical perturbing obstacle was moved along the array structure. When the obstacle was placed at a position of maximum E-field, it caused a shift in the resonant frequency of the cavity. This was indicated by a dip in the reading of the vector voltmeter. However, when the obstacle was moved to a node in the E-field, the perturbation was minimum and the vector voltmeter reading returned to within 1% of maximum value. The phase velocity of the guided wave was then calculated from the ratio of the wavelength in the cavity, to that in free space.

Phase velocity data were obtained for both the isolated and the concentric arrays. The results are compared with the theoretical values in Figures 4.4 and

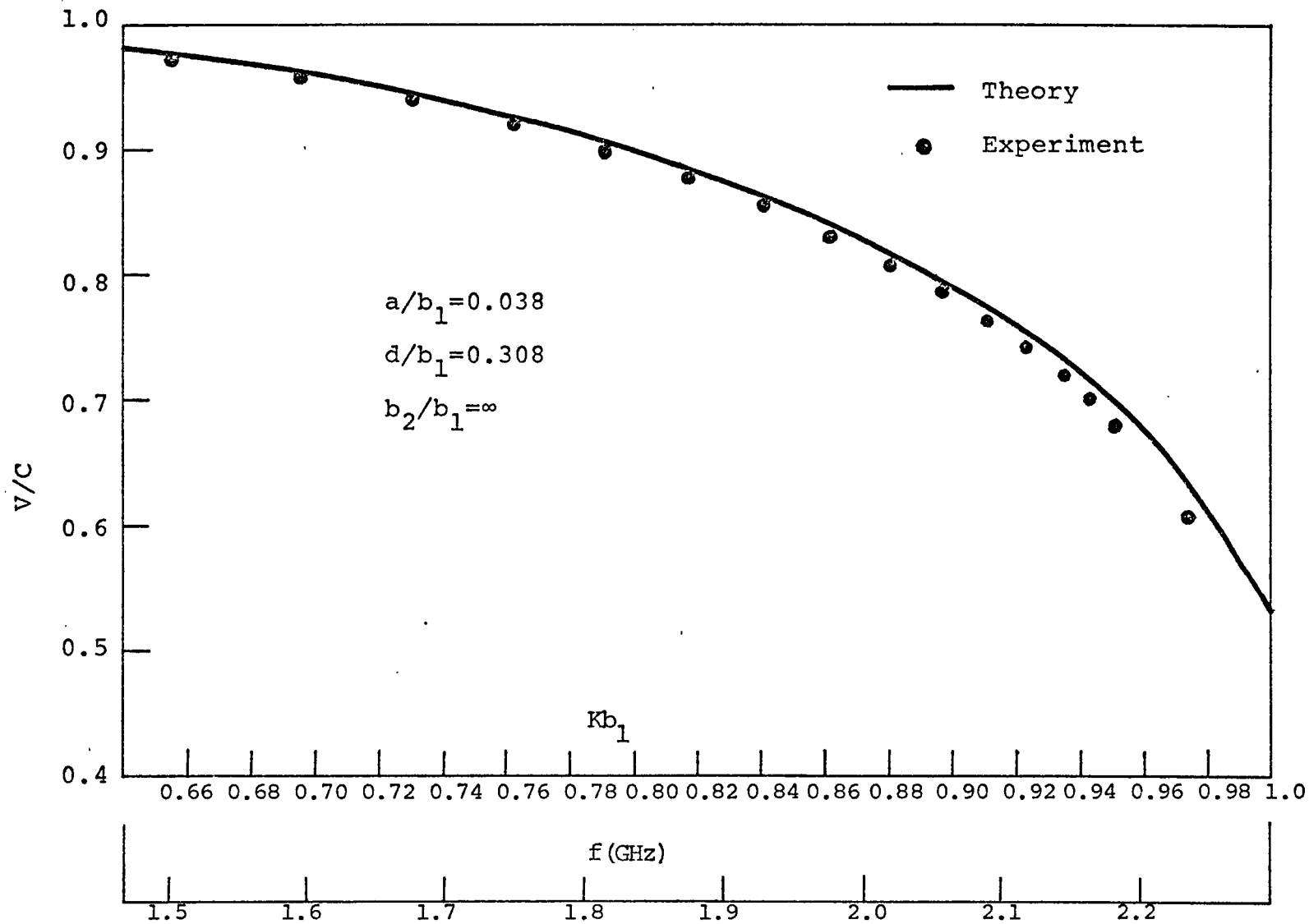


Fig. 4.4 Phase velocity of the propagating wave on the isolated array.

4.5. Note that the data for the isolated array were obtained by removing the outer loop and filling its mounting holes with conducting silver paint.

The experimental results correspond quite closely to the theoretical ones except for the second passband of the concentric array. In this band, the discrepancy between theory and experiment is about one percent in terms of  $Kb_1$ .

#### 4.4 NEAR FIELD MEASUREMENTS

Amplitude and phase patterns corresponding to frequencies in the pass- and stop-bands were obtained by near field measurements of the array. The procedure used was as follows.

- (a) With the coaxial switch thrown in position 1, the signal generator was tuned to a resonant frequency. Resonance was indicated by a peak reading on channel B of the vector voltmeter, and the resonant frequency was read from the frequency counter.
- (b) The coaxial switch was then turned to position 2 to connect the E-field probe to the sampling head.
- (c) The probe was moved to a reference location located about 36 cm from the end reflector. (This is the 90 cm

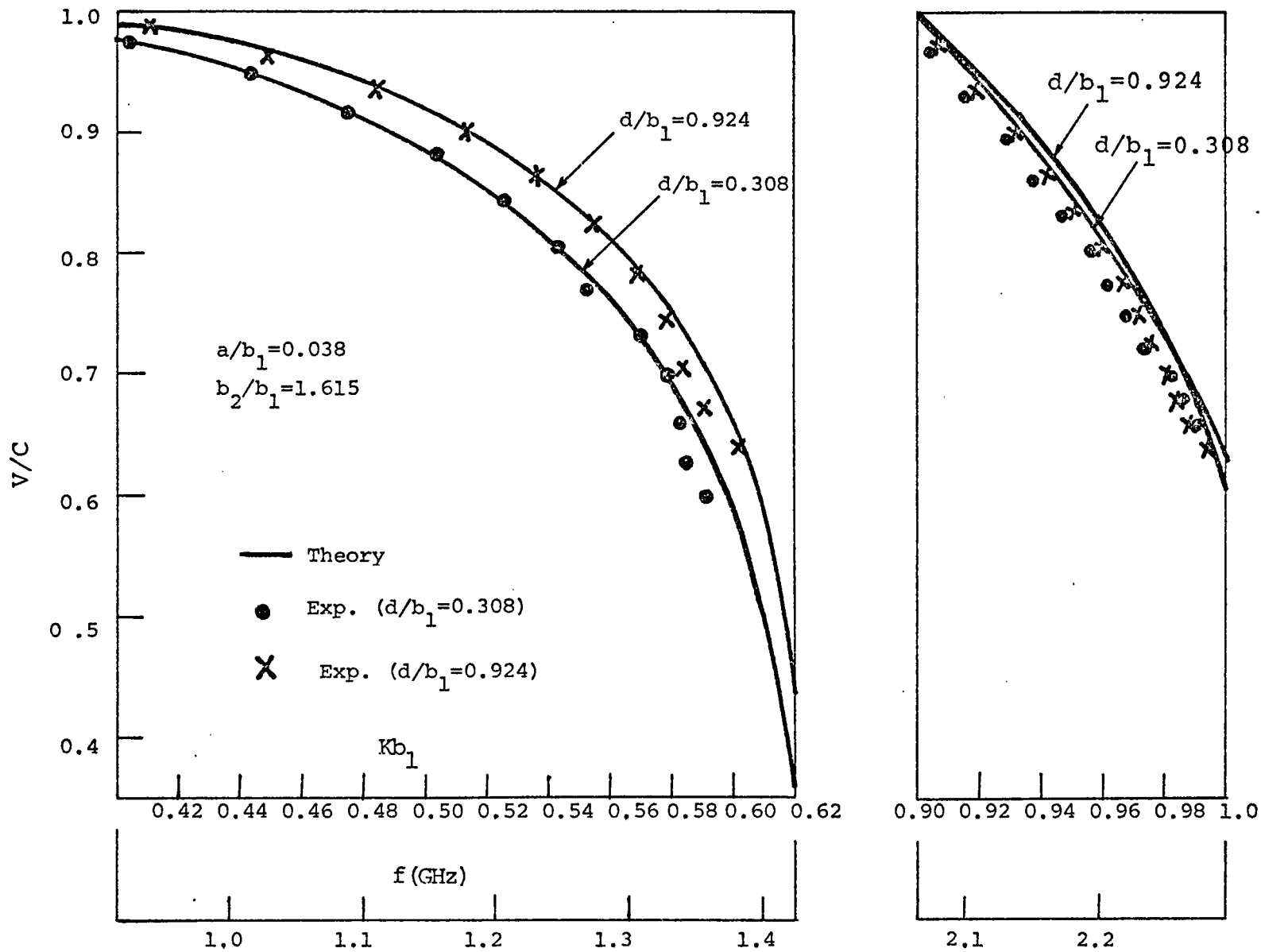


Fig. 4.5 Phase velocity of the propagating wave in the passbands of the concentric array.

point as measured from the front reflector).

(d) The level of the "reference" signal on channel A was set at a convenient level by the variable attenuator.

(e) The vector voltmeter "offset" was then used to set the phase difference ( $\phi_B - \phi_A$ ) to zero ( $\pm 1$  degree).

(f) The first data point at the location  $z=90$  cm, was read from the vector voltmeter where the amplitude was that of channel B, and the phase was read from the phase meter. (Note: the phase of the 90 cm reference point was set to zero in the previous step.)

(g) Thereafter, the slide bar was pulled in increments of 0.5 cm until the final position of 50 cm was reached. At each increment, the amplitude and phase (relative to the 90 cm reference point) were read directly from the vector voltmeter.

Note that the bulk of the data was taken in an area around the center of the cavity and away from the region illuminated by the exciter. This was done in order for the probe to sample the E-field due to the surface wave only, and not the one due to the exciter. In fact, the closest position for which near-field data was taken, was located 50 cm away from the exciting antenna.

Throughout all the near-field measurements, the probe was moved in an axial direction at a constant distance

from the concentric array. This distance was 1.427 cm from the edge of the outer loop, and 2,697 cm from the edge of the inner loop.

In order to estimate the perturbing effect of the probe on the electric field being measured, a piece of wire of roughly the same size as the probe was moved to within 0.5 cm of the measuring probe, in close proximity with the array structure. No change in the measured field intensity was discernable (in other words, the change was below the sensitivity level of the vector voltmeter of -65 dBm) unless the interfering piece of wire actually made contact with the outer loop of the array.

In the first passband, near-field data were taken at three representative resonant frequencies ( $f=1.154$ , 1.328, and 1.358 GHz). The results are plotted in Figs. 4.6, 4.7, and 4.8 respectively. In these plots, amplitude and phase data points are given along with a smooth curve representation.

Examination of the amplitude patterns shows a certain degree of spatial modulation evident in the form of unequal maxima and minima. This phenomenon may be due to the local action of the loop elements on the array near field (the condition of zero tangential E-field), and to any change in the exact transverse distance from

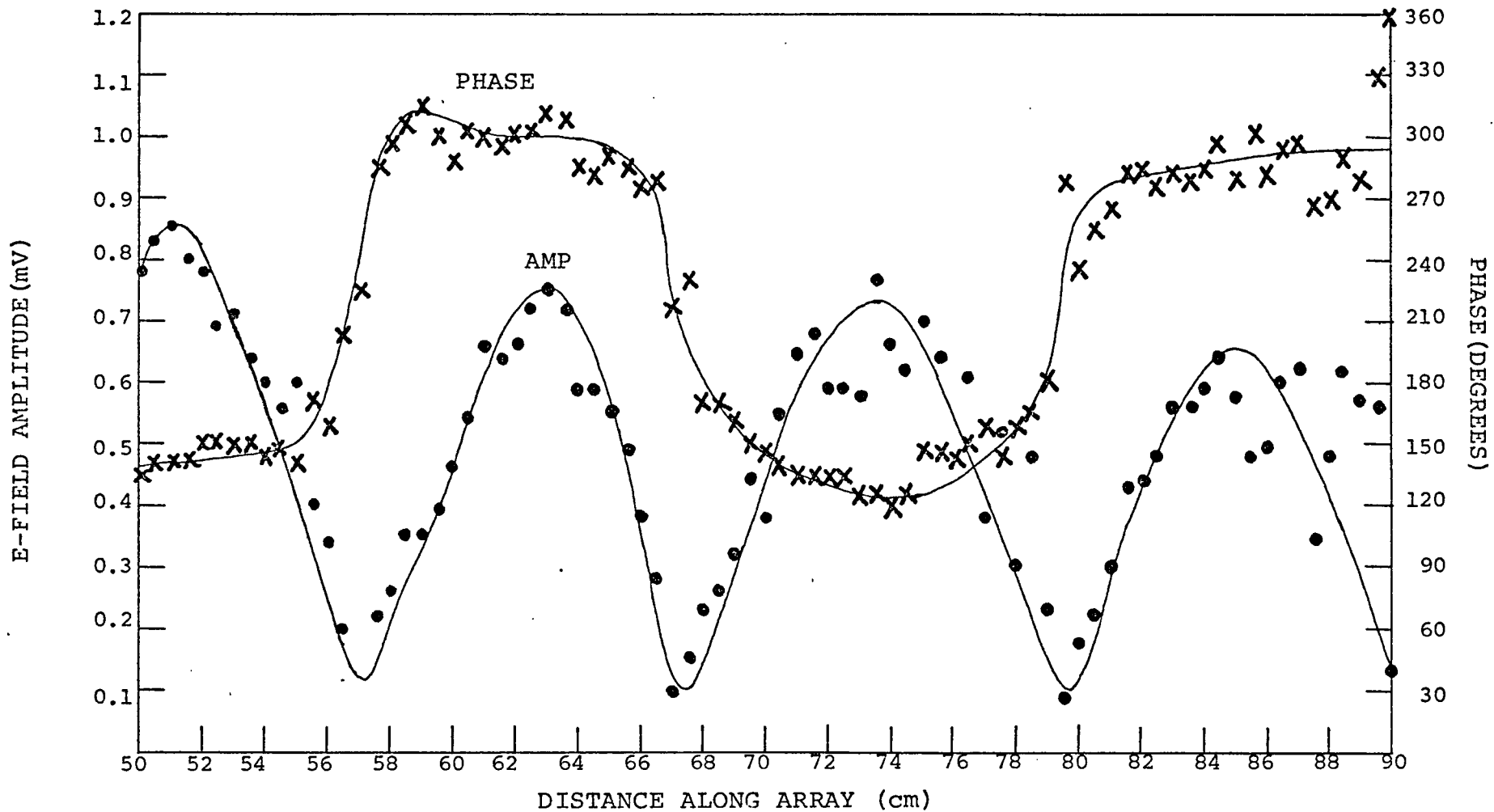


Fig. 4.6 Measured amplitude and phase of near-field of the concentric array.  
 (first passband,  $f=1.154 \text{ GHz}$ ,  $a/b_1=0.038$ ,  $d/b_1=0.308$ ,  $b_2/b_1=1.615$ )

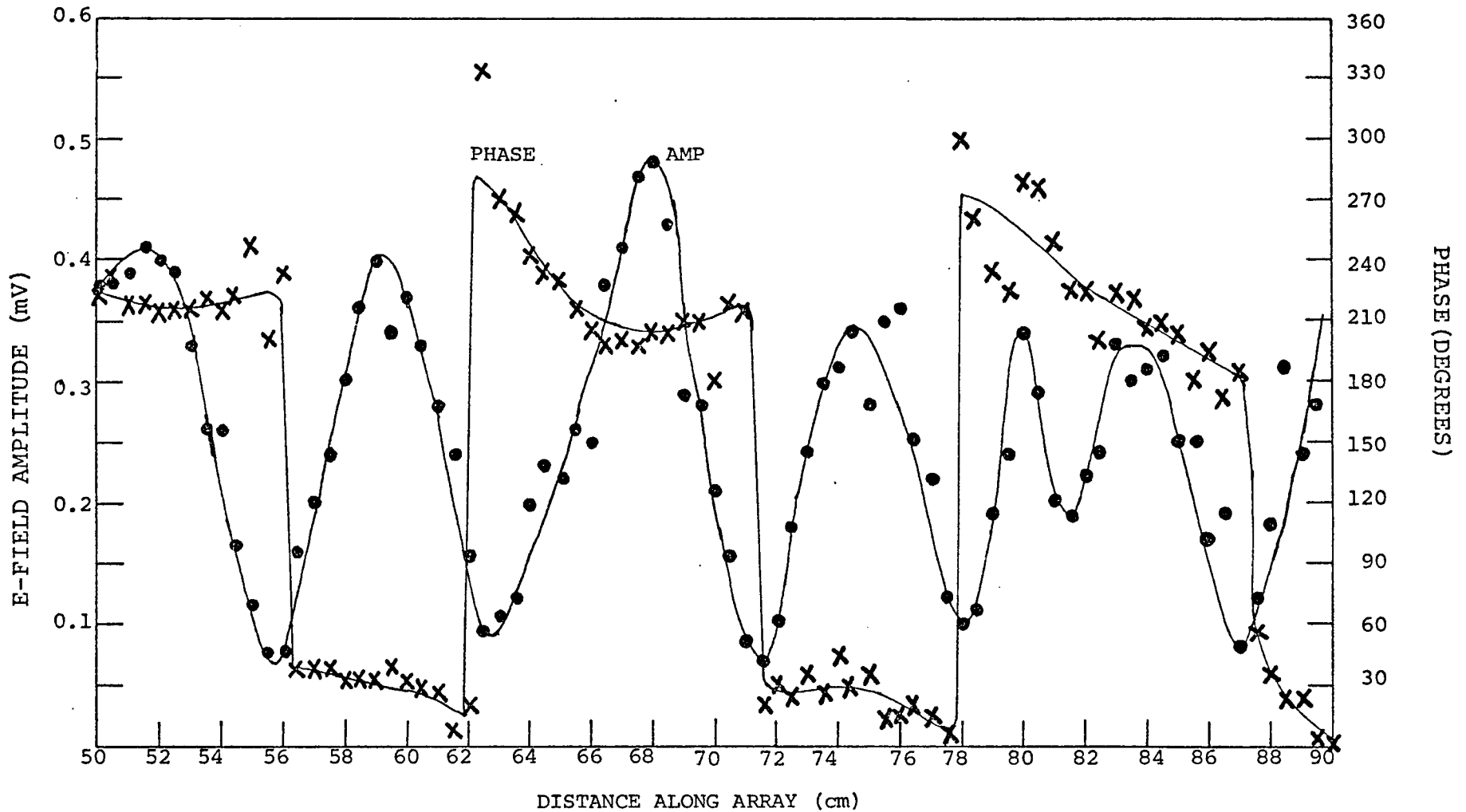


Fig. 4.7 Measured amplitude and phase of near-field of the concentric array.  
 (First passband,  $f=1.328$  GHz,  $a/b_1=0.038$ ,  $d/b_1=0.308$ ,  $b_2/b_1=1.615$ ).

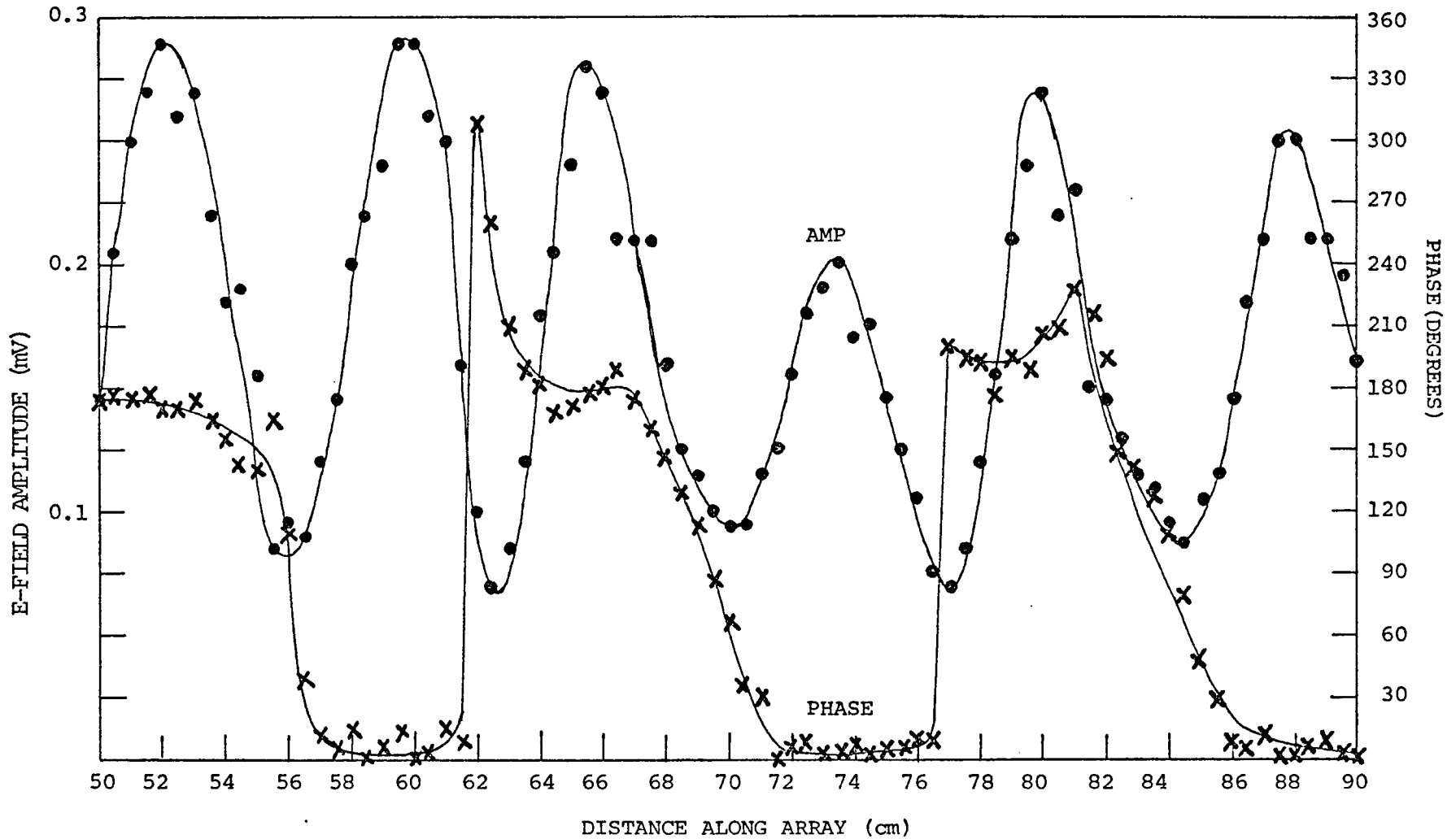


Fig. 4.8 Measured amplitude and phase of near-field of the concentric array. (First pass-band,  $f=1.358$  GHz,  $a/b_1=0.038$ ,  $d/b_1=0.308$ ,  $b_2/b_1=1.615$ ).

probe to array as the probe is moved. Due to exponential decay, a slight change in the probe transverse distance can result in considerable variation in detected levels. Also, an oscillatory behavior is noted in the amplitude patterns for the frequencies  $f=1.154$  GHz, and  $f=1.328$  GHz in the region between 80 and 90 centimeters. This behavior may be caused by a drift in the generator signal frequency, or a slight change in the resonant frequency of the cavity. In any case, this behavior takes the form of an end-effect, that is, as the probe nears the far end of the cavity. Also, the fact that there were gaps between the sliding bar and the adjoining sections of the ground plane may be another possible source of error. Nevertheless, in general, the amplitude patterns of the first passband represent surface waves that are well trapped by the guiding structure.

On the other hand, the phase patterns of the first passband are well behaved. The sharp transitions of  $\pm 180^\circ$  at every half guide wavelength, indicate relatively pure standing waveforms.

In the stopband region, located between the two passbands, the wave is a leaky one that loses energy by radiation as it travels along the structure. However, the attenuation due to radiation decreases gradually as the

frequency increases toward the second passband. In fact, the wave becomes reasonably trapped in a narrow region located right before the transition into the second passband. In this region, the amplitude distribution is neither a pure standing wave nor a pure traveling wave. As a result, it is difficult to ascertain a value for the propagation constant of the wave ( $\beta=2\pi/\lambda_g$  where  $\lambda_g$  is the guided wavelength). Note that it is characteristic of the concentric array of loops to exhibit this behavior at the point where the phase velocity undergoes a change from fast to slow. Typical patterns at a frequency in this region are shown in Fig. 4.9 with  $f=2.029$  GHz. The unequal spacings between successive minima or maxima coupled with the almost linear phase variations are evidence of the existence of evanescent waves.

In the second passband, near-field data were taken at one frequency near the lower end of the band ( $f=2.07$  GHz), and at two frequencies close to the higher end ( $f=2.206$  GHz and  $f=2.220$  GHz). Results are plotted in Figures 4.10, 4.11, and 4.12, respectively. Inspection of the amplitude patterns shows a severe spatial modulation that becomes periodic in the case of Fig. 4.11. On the other hand, the phase plots indicate quite well a surface-wave propagation with the exception of Fig. 4.12. In this case,

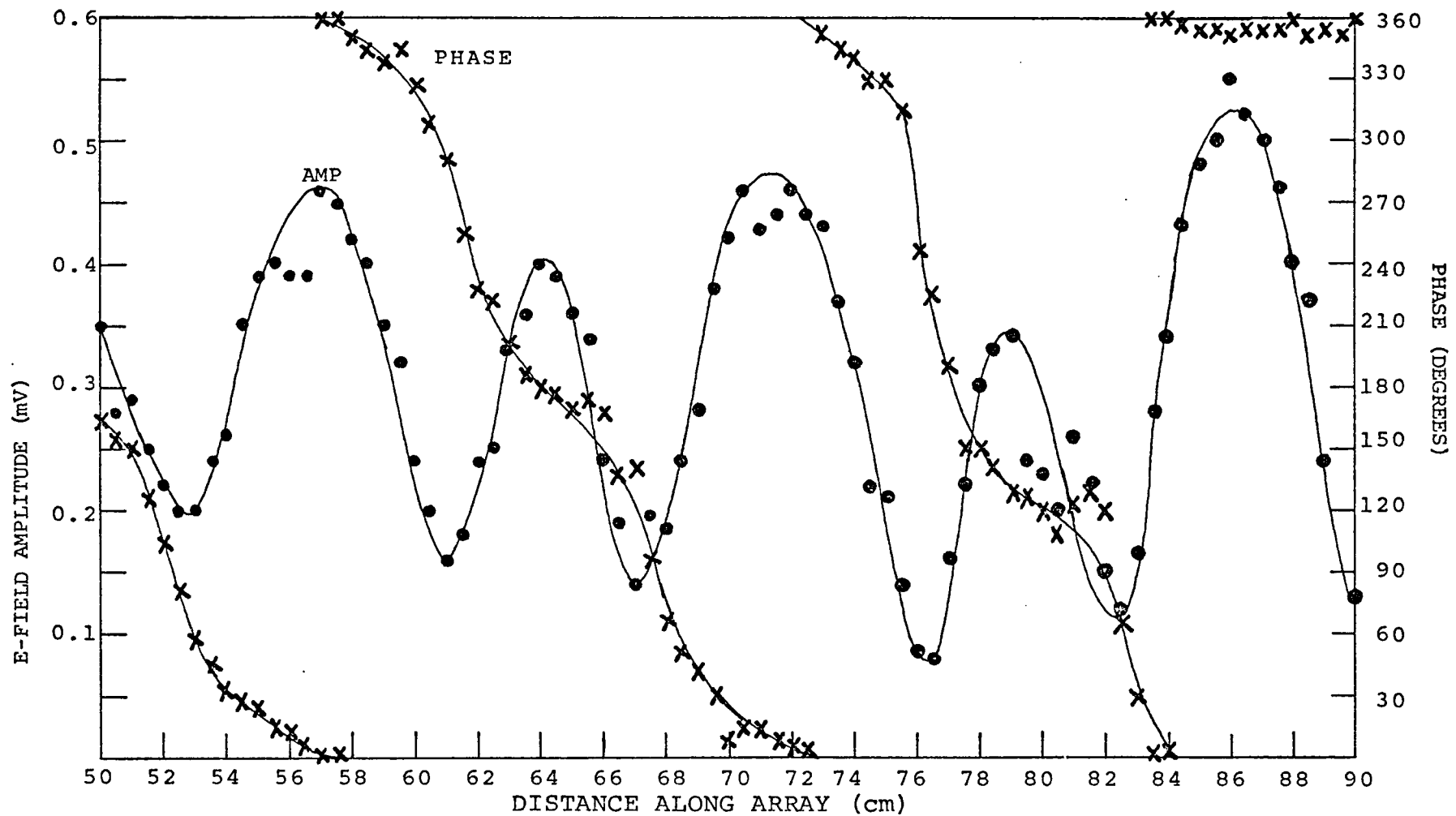


Fig. 4.9 Measured amplitude and phase of near-field of the concentric array.  
 (Stopband,  $f=2.029$  GHz,  $a/b_1=0.038$ ,  $d/b_1=0.308$ ,  $b_2/b_1=1.615$ ).

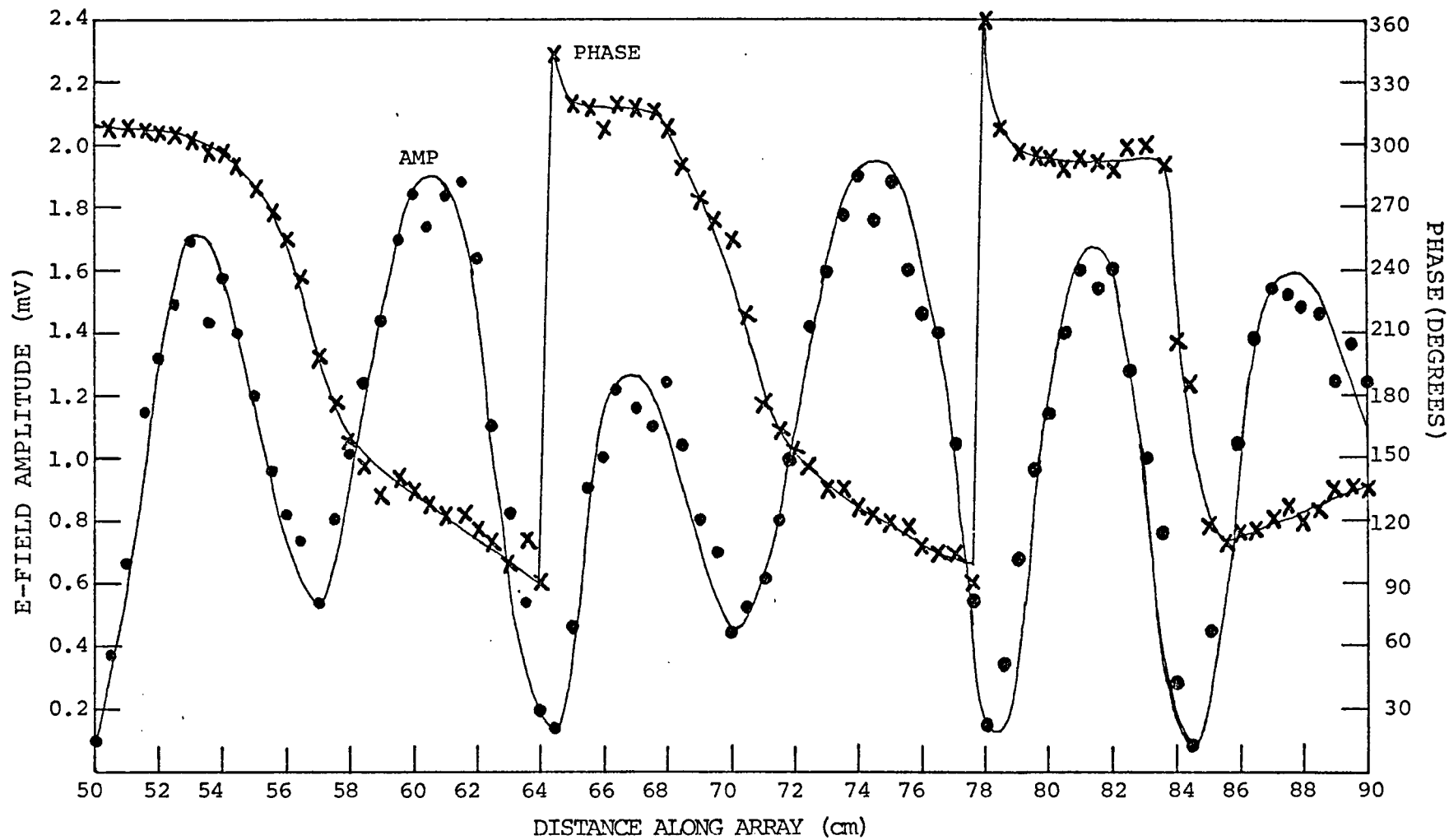


Fig. 4.10 Measured amplitude and phase of near-field of the concentric array (second passband.  $f=2.07$  GHz,  $a/b_1=0.038$ ,  $d/b_1=0.308$ ,  $b_2/b_1=1.615$ ).

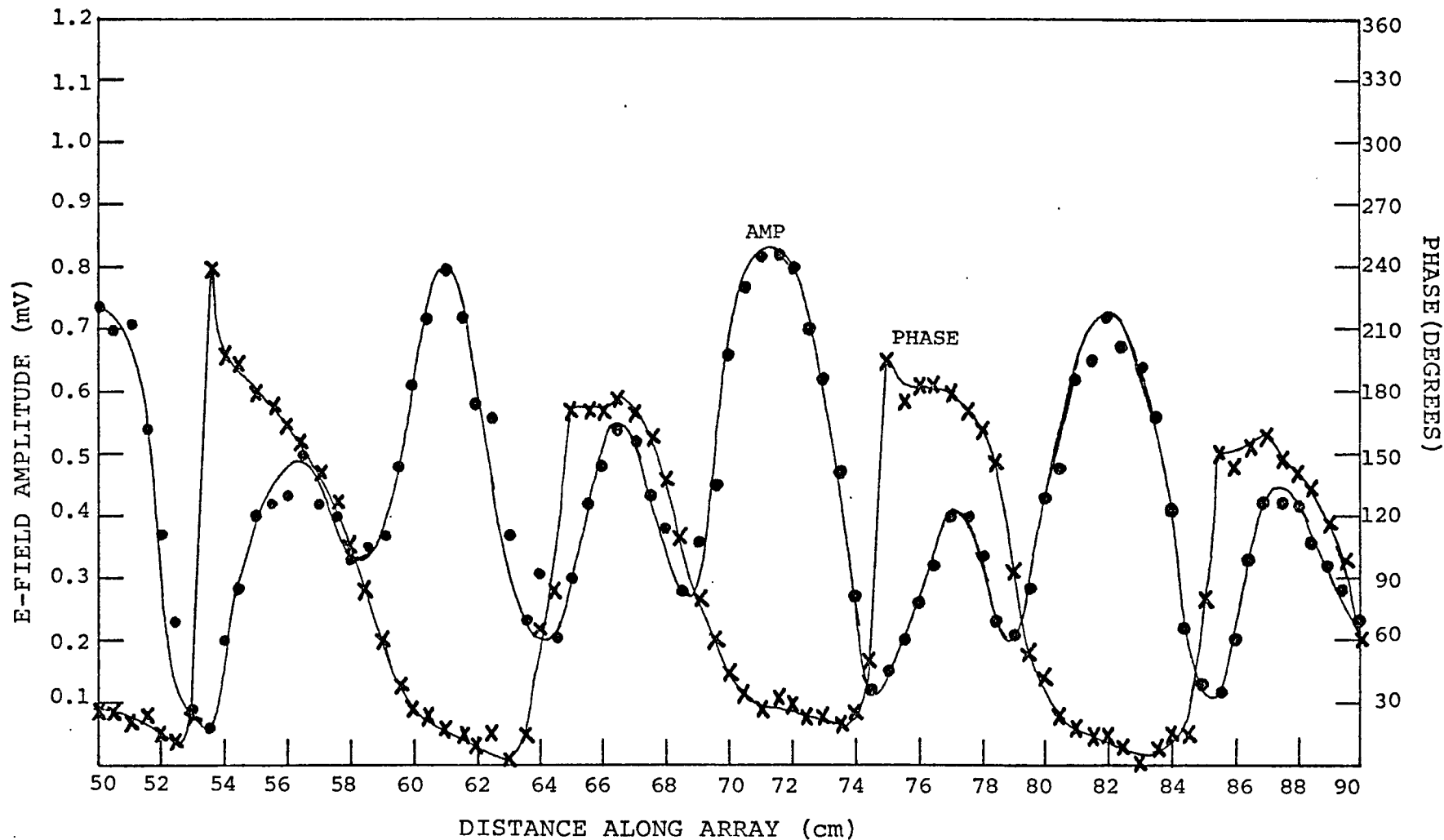


Fig. 4.11 Measured amplitude and phase of near-field of the concentric array.  
 (Second passband,  $f=2.206$  GHz,  $a/b_1=0.038$ ,  $d/b_1=0.308$ ,  $b_2/b_1=1.615$ ).

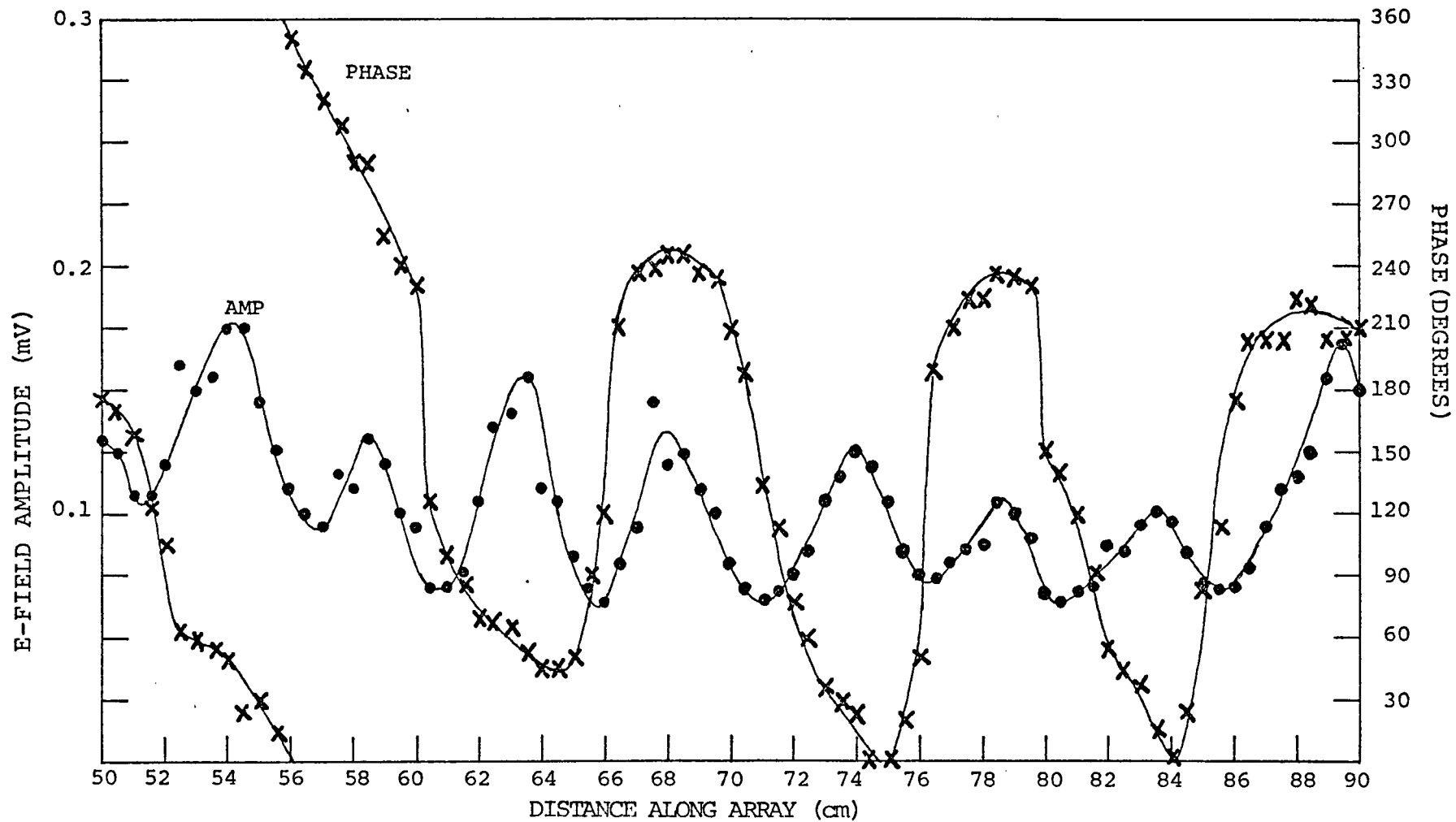


Fig. 4.12 Measured amplitude and phase of near-field of the concentric array. (second passband,  $f=2.22$  GHz,  $a/b_1=0.038$ ,  $d/b_1=0.308$ ,  $b_2/b_1=1.615$ ).

the phase pattern is more erratic due to low signal level which resulted in marginal operation of the vector voltmeter. (Signals on the order of 0.1 mv are slightly higher than the 0.075 mv noise level of the voltmeter).

#### 4.5 DUAL WAVE BAND

With a fixed exciter, and in the immediate vicinity of cutoff of either passband, it becomes exceedingly difficult to deliver enough power to the structure for adequate signal detection [58]. This is particularly true near the cutoff end of the second passband where the dual-wave phenomenon was shown to occur. It was also shown (sec. 3.5) that the two waves have unequal phase velocities and opposite directions of propagation. As a result, the oppositely directed power flows of the two waves induce a sharp decrease in resultant forward power flow, and in turn only negligible signal levels are available for sampling by the probe. Moreover, strong signal levels are extremely vital in this case, because of the necessity to fit the experimental data with two propagation constants.

To remedy this situation, a microwave power amplifier was inserted between the generator and the directional coupler (Fig. 4.1) in order to boost the generator power

output to one watt. Then, near-field data at four resonant frequencies toward the end of the second passband were obtained.

The remainder of this section is devoted to the description of the matching program used to fit the data to two propagation constants. Also, an analysis of the ensuing results is given.

#### 4.5.1 Data fitting program

It is desired to determine the parameters in the equation  $f(z)=A_1\sin \beta_1z+A_2\sin \beta_2z$  such that the sum of the squared differences between actual and predicted values is minimized. The constants  $A_1$  and  $A_2$  are complex quantities while  $\beta_1$  and  $\beta_2$  are real. The complex equation may be written as two real equations by decomposing complex quantities into real and imaginary parts.

$$f_r = A_{1r} \sin \beta_1 z + A_{2r} \sin \beta_2 z \quad (4.1a)$$

$$f_i = A_{1i} \sin \beta_1 z + A_{2i} \sin \beta_2 z \quad (4.1b)$$

where  $f = f_r + jf_i$ ,  $A_1=A_{1r} + jA_{1i}$ , and  $A_2=A_{2r} + jA_{2i}$ .

Let  $N$  designate the number of data points. The squared difference is given by

$$D = \sum_{n=1}^N (f_{rn} - A_{1r} \sin \beta_1 z_n - A_{2r} \sin \beta_2 z_n)^2 +$$

$$(f_{in} - A_{1i} \sin \beta_1 z_n - A_{2i} \sin \beta_2 z_n)^2 \quad (4.2)$$

Squaring and combining terms yields the result

$$\begin{aligned} D = D_0 + (A_{1r}^2 + A_{1i}^2) S(\beta_1) + (A_{2r}^2 + A_{2i}^2) S(\beta_2) - 2A_{1r} T(\beta_1) \\ - 2A_{2r} T(\beta_2) - 2A_{1i} Q(\beta_1) - 2A_{2i} Q(\beta_2) + 2(A_{1r} A_{2r} + A_{1i} A_{2i}) \\ U(\beta_1, \beta_2) \end{aligned} \quad (4.3)$$

where

$$S(\beta) = \sum_{n=1}^N \sin^2 \beta z_n = \frac{N}{2} - \frac{1}{2} \sum_{n=1}^N \cos(2\beta z_n)$$

$$T(\beta) = \sum_{n=1}^N f_{rn} \sin \beta z_n$$

$$Q(\beta) = \sum_{n=1}^N f_{in} \sin \beta z_n$$

$$U(\beta_1, \beta_2) = \sum_{n=1}^N \sin \beta_1 z_n \sin \beta_2 z_n = S\left[\frac{\beta_1 + \beta_2}{2}\right] - S\left[\frac{\beta_1 - \beta_2}{2}\right]$$

Note the expression for  $D$  is nonlinear in  $\beta_1$  and  $\beta_2$  and linear in the other four parameters. Therefore, it is necessary to fix  $\beta_1$  and  $\beta_2$  and minimize  $D$  in terms of  $A_{1r}$ ,  $A_{2r}$ ,  $A_{1i}$  and  $A_{2i}$ . This is done by taking partial derivatives and setting them equal to zero. Namely,

$$\frac{\partial D}{\partial A_{1r}} = \frac{\partial D}{\partial A_{2r}} = \frac{\partial D}{\partial A_{1i}} = \frac{\partial D}{\partial A_{2i}} = 0 \quad (4.4)$$

The solution of the resulting four equations for the four unknowns yields

$$A_{1r} = \frac{T(\beta_1)S(\beta_2) - T(\beta_2)U(\beta_1, \beta_2)}{S(\beta_1)S(\beta_2) - U^2(\beta_1, \beta_2)} \quad (4.5a)$$

$$A_{2r} = \frac{S(\beta_1)T(\beta_2) - T(\beta_1)U(\beta_1, \beta_2)}{S(\beta_1)S(\beta_2) - U^2(\beta_1, \beta_2)} \quad (4.5b)$$

$$A_{1i} = \frac{Q(\beta_1)S(\beta_2) - Q(\beta_2)U}{S(\beta_1)S(\beta_2) - U^2} \quad (4.5c)$$

$$A_{2i} = \frac{S(\beta_1)Q(\beta_2) - Q(\beta_1)U}{S(\beta_1)S(\beta_2) - U^2} \quad (4.5d)$$

An attempt to minimize the squared difference  $D$  in terms of  $\beta_1$  and  $\beta_2$  by two-dimensional Newton method was not successful due to the large number of local minima. A search technique was later used in which  $\beta_1$  and  $\beta_2$  are varied in their respective ranges with the parameters  $A_{1r}$ ,  $A_{2r}$ ,  $A_{1i}$ ,  $A_{2i}$  and  $D$  evaluated for each pair of values. The calculated values of  $D$  are normalized with respect to the minimum and scaled by a factor of 10 before being displayed in a square array pattern. The variable  $\beta_1$  is incremented from one row to the next and its value for each row is printed on the left hand side

of the pattern. In a similar fashion,  $\beta_2$  is incremented from one column to the next.

#### 4.5.2 Analysis of results

In order to test the ability of the program to converge to the correct solution, two sets of data have been prepared and used to obtain typical test patterns. The first data set is chosen to correspond to a single wave (one propagation constant), and the second data set is selected to conform to a dual-wave (two propagation constants).

The pattern for the first set contains one row and one column of the same order (16) which are made up of relatively low values of  $D$ . This is illustrated in Fig. 4.13. The minimum in the pattern is at the location (27, 16) which corresponds to  $\beta_1=52.52$  and  $\beta_2=66.73$ . The weighting of  $\beta_1$  is determined by the magnitude of the coefficient  $A_1$  and the weighting of  $\beta_2$  is specified by the magnitude of  $A_2$ . Therefore, patterns for  $|A_1|^2$  and  $|A_2|^2$  (suitably scaled so that the maximum value is equal to 99) are given in Figs. 4.14 and 4.15 for comparison. At the array location (27, 16), corresponding to the minimum squared difference  $D$ , the values of  $|A_1|^2$  and  $|A_2|^2$  are 17 and 0 respectively. Hence,  $\beta_1$  corresponds to the dominant wave and  $\beta_2$  may be neglected. It follows that  $\beta=\beta_1=52.52$ .







The pattern for the second set of data is shown in Fig. 4.16. It indicates a minimum at the array location (14, 7) which corresponds to  $\beta_1=53.15$  and  $\beta_2=57.42$ . Since  $|A_1|^2$  and  $|A_2|^2$  are of the same order of magnitude ( $|A_1|^2=98$ ,  $|A_2|^2=64$ ), the two waves are equally dominant.

In the light of the above test patterns, one can now analyze those patterns corresponding to the four resonant frequencies which are located at the end of the second passband.

The data obtained at the frequency  $f=2.220$  GHz is plotted in Fig. 4.17. The resulting pattern of the squared difference is shown in Fig. 4.18. The row and column of order 8 are seen to contain relatively low values of  $D$ . Note that the value of  $D$  at the array location (8,8) is of the same order of magnitude as the minimum at (8,4). Also, the coefficients  $A_1$  and  $A_2$  at (8,4) are of the same order of magnitude ( $|A_1|^2=28$ ,  $|A_2|^2=89$ ). Therefore, the location (8,8) is selected as a solution where  $\beta_1=\beta_2=62.02$ . This corresponds to a normalized phase velocity of 0.749 which is exactly equal to the one obtained by the resonator method (Fig. 4.5).

The data obtained at the frequency  $f=2.25$  GHz is plotted in Fig. 4.19. The corresponding squared difference pattern is displayed in Fig. 4.20. The row and column of order 13 contain only low values of  $D$ . Note that the



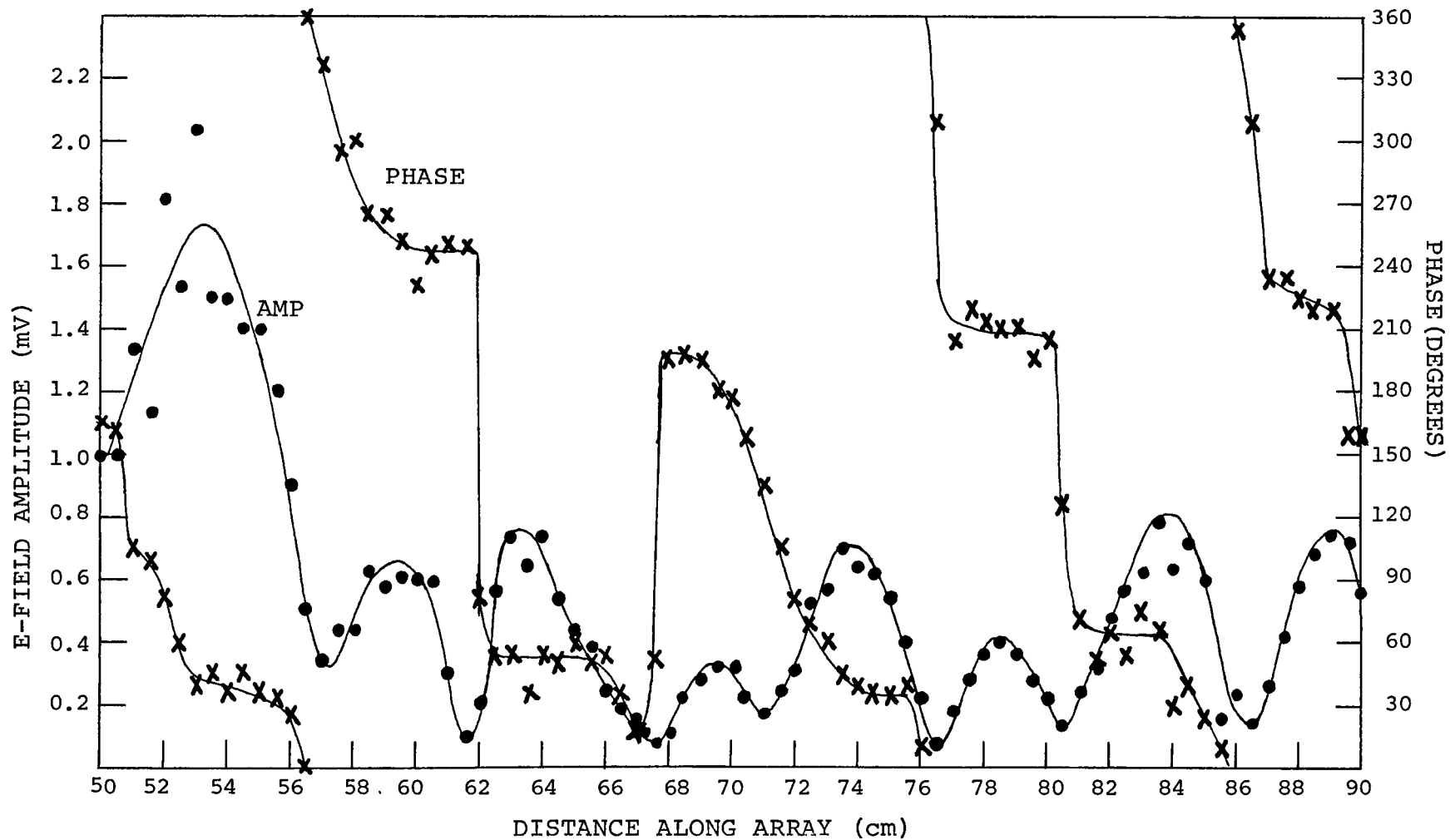


Fig. 4.17 Measured amplitude and phase of near-field of the concentric array. (Second passband,  $f=2.22$  GHz,  $a/b_1=0.038$ ,  $d/b_1=0.308$ ,  $b_2/b_1=1.615$ ).



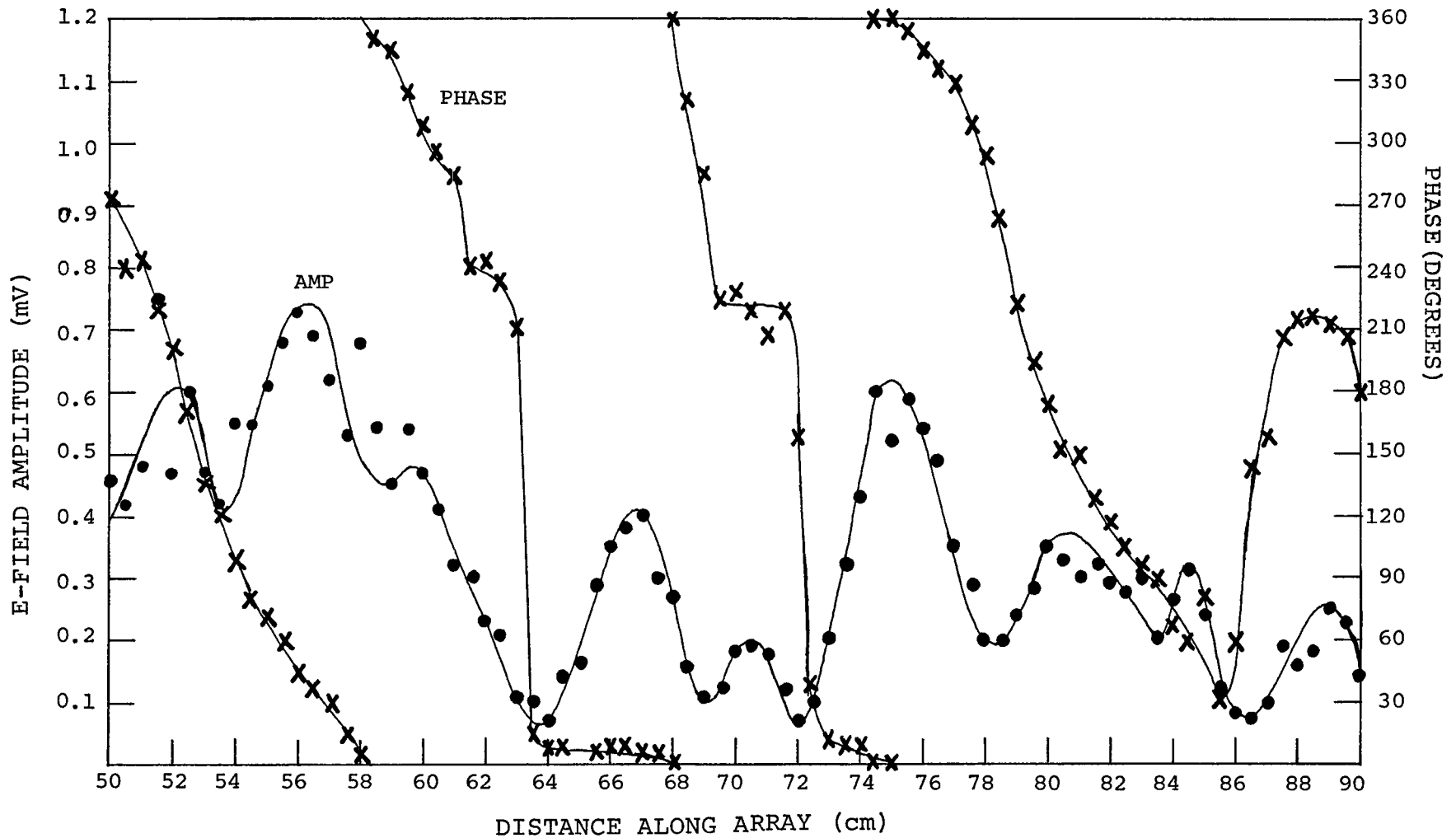


Fig. 4.19 Measured amplitude and phase of near-field of the concentric array.  
 (Second passband,  $f=2.25$  GHz,  $a/b_1=0.038$ ,  $d/b_1=0.308$ ,  $b_2/b_1=1.615$ ).



value of  $D$  at the array location (13, 13) is of the same order of magnitude as the minimum located at (13,10). Moreover, the coefficients  $A_1$  and  $A_2$  at (13,10) are of the same order of magnitude ( $|A_1|^2=27$ ,  $|A_2|^2=36$ ). Therefore, the location (13,13) is selected as a solution with  $\beta_1=\beta_2=68.60$ . In terms of the normalized phase velocity, a  $\beta$  of 68.60 corresponds to  $v/c$  of 0.686 which differs by .017 from that obtained by the resonator method.

The data obtained at the frequency  $f=2.263$  GHz is plotted in Fig. 4.21. The resulting pattern is given in Fig. 4.22. In this case one can identify row 14 and column 14 as having predominantly low values of  $D$ . Note that the value of  $D$  at the array location (14,14) is of the same order of magnitude as the minimum positioned at (15,9). On the other hand, the coefficients  $A_1$  and  $A_2$  at (15,9) have roughly equal magnitudes ( $|A_1|^2=21$ ,  $|A_2|^2=29$ ). Then, the location (14,14) is taken as the solution where  $\beta_1=\beta_2=70.27$ . The corresponding phase velocity is equal to 0.674 which differs by .008 from the one obtained by resonant methods.

Finally, the data obtained at the frequency  $f=2.276$  GHz is plotted in Fig. 4.23. The pattern is displayed in Fig. 4.24. A careful scanning of the square array reveals that all the printed values of  $D$  have the

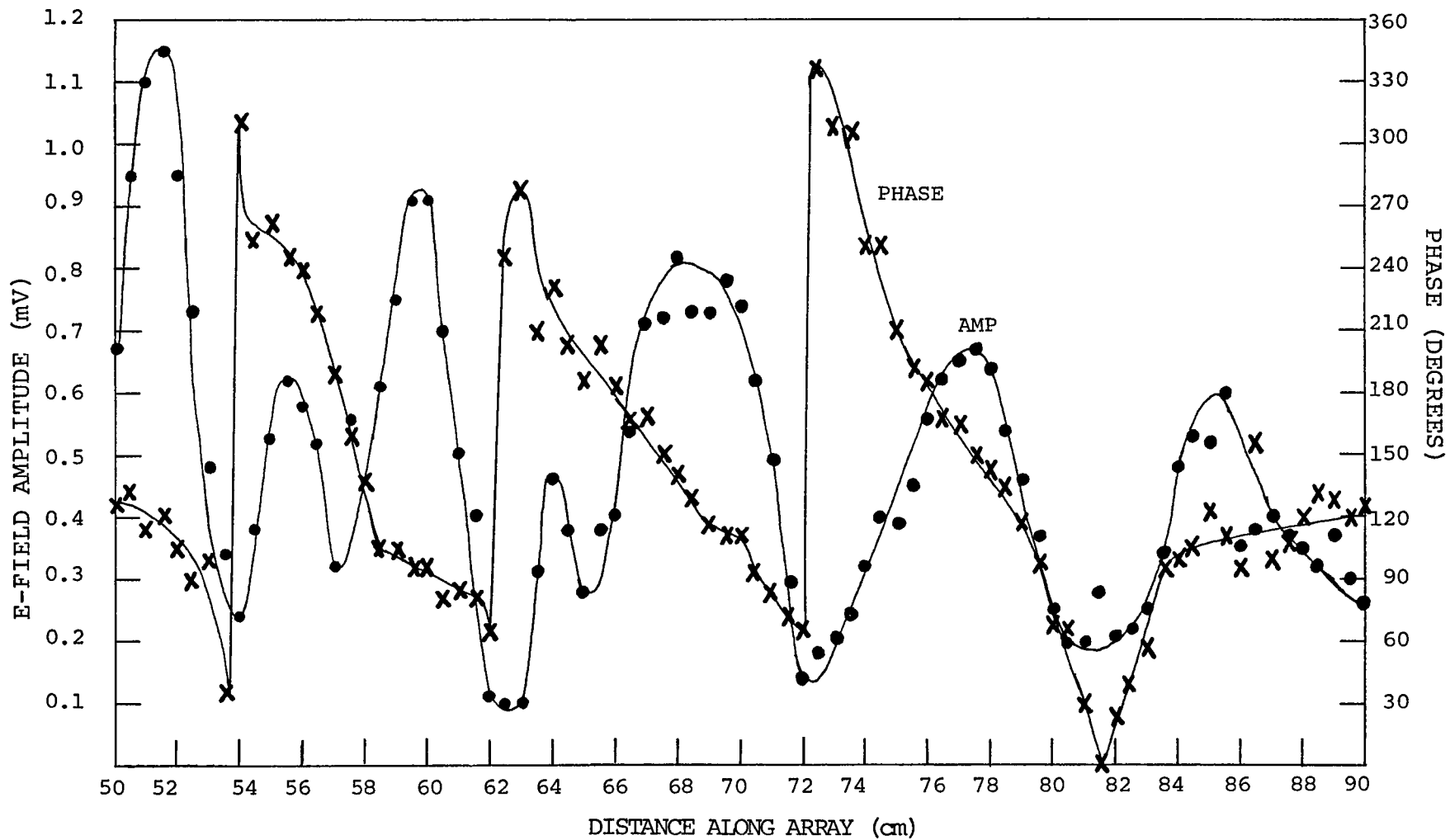


Fig. 4.21 Measured amplitude and phase of near-field of the concentric array.  
 (Second passband,  $f=2.263$  GHz,  $a/b_1=0.038$ ,  $d/b_1=0.308$ ,  $b_2/b_1=1.615$ ).

10.0	8	56.57	5	7	8	7	4	4	7	7	3	4	9	6	5	9	9	8	9	10	9	9	9	9	9	9	9	9	10	10	10	9	1C	1C	10	10	1C
1.0	7	57.43	4	6	8	6	3	3	8	7	3	5	9	6	5	9	9	8	1C	1C	1C	9	1C	9	9	10	9	10	10	10	10	10	10	10	10	10	10
2.0	9	58.32	5	3	8	6	3	1	7	6	1	3	8	5	4	8	8	7	8	9	9	8	8	8	8	8	8	9	9	9	9	9	9	9	9	9	9
3.0	7	59.23	5	4	5	6	2	1	5	6	0	1	7	4	3	6	6	6	7	7	7	7	7	7	6	7	6	7	7	7	7	7	7	7	7	7	7
4.0	6	60.18	5	5	5	6	3	2	4	6	1	1	6	4	2	6	6	5	7	7	7	7	7	6	6	6	6	6	6	6	6	6	6	6	6	6	6
5.0	5	61.15	8	5	5	5	4	4	5	6	3	3	7	5	3	7	6	6	7	7	7	7	7	7	7	7	7	7	7	7	7	7	7	7	7	7	7
6.0	3	62.16	5	8	5	5	3	2	7	6	2	4	8	5	4	7	7	6	8	8	8	8	8	8	8	7	8	7	8	8	8	8	8	8	8	8	8
7.0	8	63.20	5	5	8	4	2	0	6	6	1	2	8	5	3	7	7	6	8	8	8	8	8	8	8	8	8	7	8	7	8	8	8	8	8	8	8
8.0	6	64.28	5	5	4	7	2	1	1	7	1	0	5	4	1	6	6	5	6	7	7	6	6	5	6	6	6	6	6	6	6	6	6	6	6	6	6
9.0	3	65.40	4	3	2	2	5	2	2	3	3	1	3	4	1	3	4	3	4	4	4	4	4	4	4	4	4	4	4	4	4	4	4	4	4	4	4
10.0	1	66.55	4	2	0	1	2	5	3	2	1	4	4	3	3	4	4	3	4	5	4	4	4	4	4	4	4	4	4	4	4	4	4	4	4	4	4
11.0	7	67.75	5	7	6	1	2	3	8	2	1	0	8	4	3	8	7	6	8	8	8	7	8	7	7	7	7	7	7	7	7	7	7	7	7	7	7
12.0	6	68.98	6	6	6	7	3	2	7	7	1	0	2	6	2	4	7	5	7	7	7	7	7	7	7	6	7	6	7	7	7	7	7	7	7	7	7
13.0	1	70.27	3	2	1	1	3	1	1	1	3	1	1	2	2	1	2	2	2	3	3	3	3	3	3	2	3	2	3	3	3	3	3	3	3	3	3
14.0	3	71.60	3	4	2	0	1	4	0	0	1	5	3	3	4	5	4	5	5	4	4	5	4	4	4	4	4	4	4	4	4	4	4	4	4	4	4
15.0	8	72.99	7	8	8	5	3	4	8	2	1	3	9	4	4	7	8	7	5	9	9	9	9	9	8	9	8	9	9	9	9	9	9	9	9	9	9
16.0	5	74.43	5	5	5	4	4	3	4	6	2	3	4	7	4	3	5	6	3	6	6	6	6	6	5	7	5	7	7	7	7	7	6	7	7	6	7
17.0	4	75.93	3	4	3	1	1	3	3	2	2	4	4	4	5	5	5	5	5	4	5	4	5	5	5	5	5	5	5	5	5	5	5	5	5	5	5
18.0	8	77.49	7	7	7	6	3	4	8	4	1	5	7	3	5	9	8	8	9	9	9	9	9	9	8	9	9	9	9	9	9	9	9	9	9	9	9
19.0	8	79.12	6	7	7	6	4	4	7	7	2	5	8	5	5	8	9	8	6	9	9	8	9	9	8	9	8	9	8	9	8	8	8	8	8	8	8
20.0	7	80.81	6	6	6	5	3	3	6	5	2	4	7	6	5	8	8	8	7	8	7	7	8	7	8	8	8	8	8	8	8	8	8	8	8	8	8
21.0	8	82.58	7	8	8	6	4	4	8	7	2	5	9	3	5	9	6	8	10	10	9	10	9	9	8	9	9	10	10	10	10	10	10	10	10	10	10
22.0	9	84.43	7	8	8	7	4	5	8	7	3	5	9	6	4	9	9	7	1C	1C	10	8	1C	9	9	10	9	10	10	10	10	10	10	10	10	10	10
23.0	9	86.36	7	8	8	7	4	4	8	7	3	4	9	6	5	9	9	8	9	10	10	9	7	9	8	9	9	10	10	10	10	10	10	10	10	10	10
24.0	8	88.39	7	8	8	6	4	4	7	7	3	4	9	6	4	9	8	7	1C	8	9	1C	9	9	9	9	9	9	10	10	10	10	10	10	10	10	10
25.0	8	90.51	7	8	8	6	4	4	8	7	3	5	9	6	5	9	9	7	5	1C	7	9	1C	9	8	9	9	9	10	10	10	10	10	10	10	10	10
26.0	8	92.73	7	8	7	6	4	4	7	7	3	4	9	6	5	9	9	8	9	9	9	9	9	9	10	8	1C	8	9	9	9	1C	1C	9	1C	1C	
27.0	8	95.07	6	7	7	5	3	4	7	6	2	4	8	5	5	8	8	7	8	9	8	9	8	9	9	9	9	9	9	9	9	9	9	9	9	9	9
28.0	8	97.53	7	8	8	6	4	4	7	7	3	4	9	7	5	9	9	8	9	10	9	9	9	10	9	10	8	10	9	10	10	10	10	10	10	10	
29.0	8	100.12	7	7	7	6	4	4	7	6	2	4	8	5	5	9	8	8	9	9	9	9	8	9	8	9	9	9	9	9	9	9	9	9	9	9	9
30.0	9	102.85	7	8	8	6	4	4	8	7	3	4	9	7	5	9	9	8	1C	10	10	9	9	9	9	10	9	10	9	10	10	10	10	10	10	10	10
31.0	9	105.73	7	8	8	7	4	5	8	7	3	5	9	7	5	9	9	8	1C	1C	10	10	9	9	9	9	9	10	10	10	10	10	10	10	10	10	10
32.0	9	108.78	7	8	8	7	4	4	8	7	3	5	9	7	5	9	9	8	1C	10	10	10	10	9	9	9	9	10	10	10	10	10	10	10	10	10	10
33.0	9	112.61	7	8	8	7	4	5	8	7	3	5	9	7	5	9	9	8	1C	10	10	10	10	9	9	9	10	10	10	10	10	10	10	10	10	10	10
34.0	9	115.44	7	8	8	7	4	5	8	7	3	5	9	7	5	9	9	8	1C	10	10	10	10	9	9	9	10	10	10	10	10	10	10	10	10	10	10
35.0	9	119.09	7	8	8	7	4	5	8	7	3	5	9	7	5	9	9	8	1C	1C	1C	1C	10	9	1C	9	10	10	10	10	10	10	10	10	10	10	10
36.0	9	122.97	8	8	8	7	5	5	8	7	3	5	9	7	5	9	9	8	1C	1C	10	1C	1C	10	9	10	9	10	10	10	10	10	10	10	10	10	10
37.0	9	127.12	8	8	8	7	5	5	8	7	3	5	9	7	5	9	9	8	10	10	10	10	10	9	10	9	10	10	10	10	10	10	10	10	10	10	10
38.0	9	131.55	7	8	8	7	4	4	8	7	3	5	9	6	5	9	9	8	1C	10	10	9	1C	9	9	10	9	10	10	10	10	10	10	10	10	10	10
39.0	9	136.31	7	8	8	7	4	4	8	7	3	5	9	7	5	9	9	8	1C	10	1C	1C	1C	9	9	10	9	10	10	10	10	10	10	10	10	10	10
40.0	9	141.42	7	8	8	7	4	5	8	7	3	5	9	7	5	9	9	8	1C	10	10	10	10	9	9	10	9	10	10	10	10	10	10	10	10	10	10
10.0	10	147.7	7	8	8	7	4	5	8	7	3	5	9	7	5	9	9	8	1C	10	10	10	10	9	9	10	9	10	10	10	10	10	10	10	10	10	

Fig. 4.22 Squared difference pattern corresponding to F=2.263 GHz.

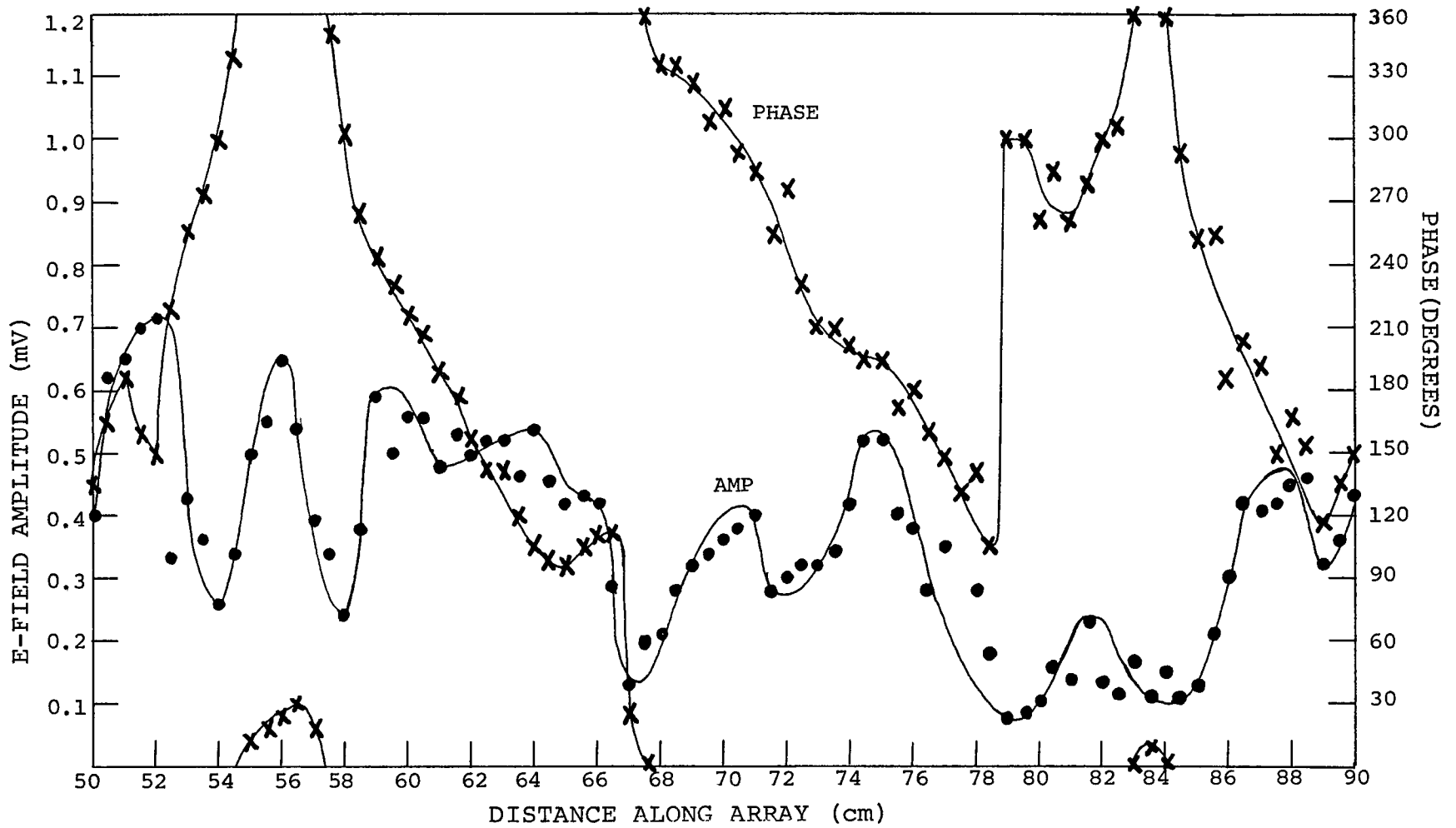


Fig. 4.23 Measured amplitude and phase of near-field of the concentric array.  
 (Second passband,  $f=2.276$  GHz,  $a/b_1=0.038$ ,  $d/b_1=0.308$ ,  $b_2/b_1=1.615$ ).



same order of magnitude. The reason for this behavior may be attributed to the large noise content of the data set at this frequency. Therefore, a reliable solution cannot be obtained in this case.

In conclusion, the experiment was successful in verifying the existence of pass- and stop-bands, and in determining the phase velocities of the propagating waves with good accuracy. However, it did not detect the dual-wave phenomenon. The lack of detection may be attributed to one of two reasons. 1) The theoretical bandwidth of two percent of the dual-wave band may be too small to accommodate a resonant frequency. 2) Even if a resonant frequency does fall in this band, the two opposing waves act to make detection difficult especially in a region bordering on cutoff.

## CHAPTER 5

THE INFINITELY LONG YAGI ARRAY OF  
COAXIALLY-DISPLACED LOOPS

## 5.1 MOTIVATION

It was shown in Chapter 3 that an infinitely long Yagi array of concentric loops can support a propagating wave in two distinct passbands. When the frequency of excitation is within one of the passbands, the structure behaves as a surface-waveguide that may be used to transfer energy from one point to another.

Hence, from a waveguiding point of view, it seems reasonable to expect the propagation characteristics to be unaffected by an axial translation of the inner array, relative to the outer one, or vice-versa. In other words, an axial shift of the inner loop from the plane of the outer loop should not result in any change in the range of the passbands, or in the phase velocities of the propagating waves in these bands.

In this chapter, it is shown that this is actually the case, except for some minor differences. The technique detailed in chapter 3 is employed to derive a dispersion relation for the new array of coaxially displaced

loops. Then, the dispersion relation is solved numerically for the phase velocity of the propagating wave for a typical set of array parameters. Finally, the results obtained are tabulated for comparison with those found for the concentric array.

## 5.2 DERIVATION OF THE DISPERSION RELATION

The infinitely long Yagi array of coaxially displaced loops is shown in Fig. 5.1, where the parameters ( $a_1$ ,  $a_2$ ,  $b_1$ ,  $b_2$ ,  $S$  and  $d$ ) are defined.

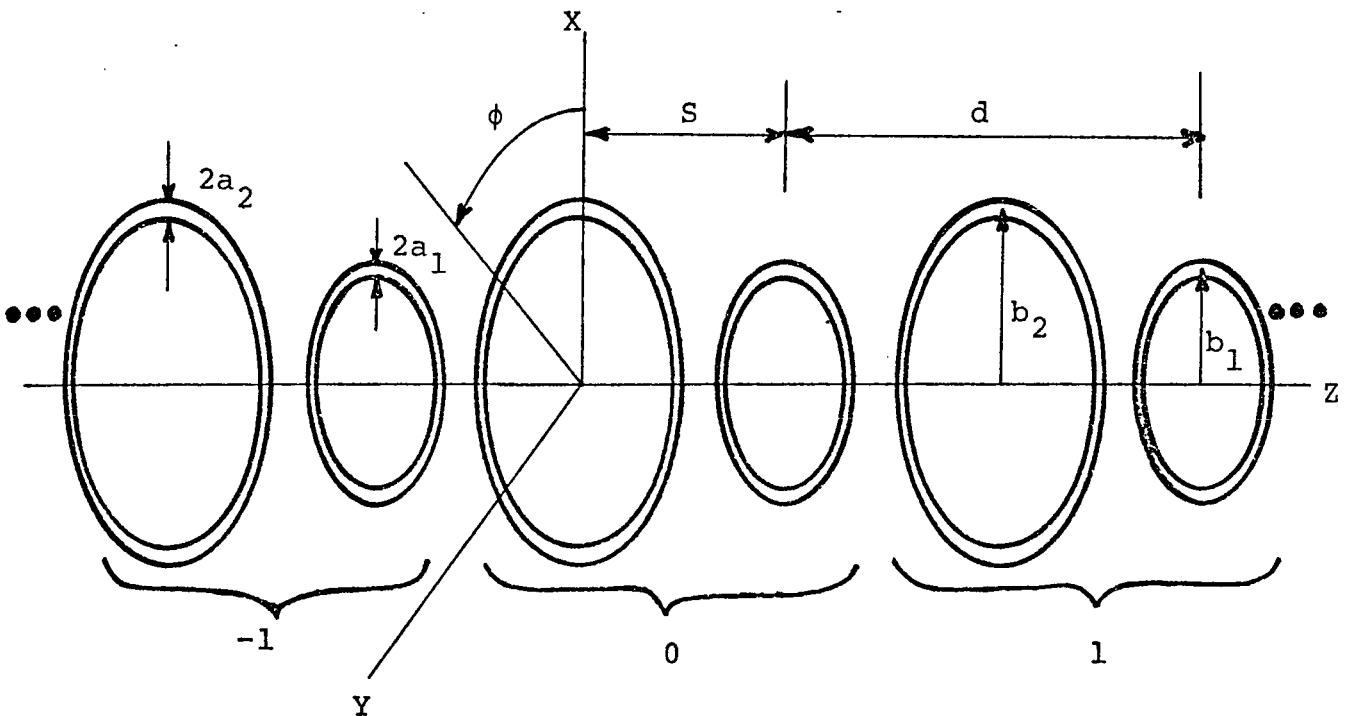


Fig. 5.1 The Yagi array of coaxially displaced loops.

The currents on the two loops of the typical  $n$ th cell are assumed to have the following form

$$I_{1n} = A_1 \cos m\phi e^{-j\beta(S+nd)} \quad (5.1a)$$

$$I_{2n} = A_2 \cos m\phi e^{-jn\beta d} \quad (5.1b)$$

where  $I_{1n}$  and  $I_{2n}$  are the currents on the small and large loop respectively.

A dispersion relation is obtained by setting the tangential component of the electric field equal to zero on the surfaces of the elements contained in the zeroth cell. Thus, let  $P_1(\theta_1, \phi)$  and  $P_2(\theta_2, \phi)$  be two field points located arbitrarily at some angle  $\phi$  on the surfaces of the small and large loop of the zeroth cell. Also, let  $P'_1(\theta'_1, \phi')$  and  $P'_2(\theta'_2, \phi')$  be two source points located arbitrarily at some angle  $\phi'$  on the surfaces of the small and large loop of the typical  $n$ th cell. This is illustrated graphically in Fig. 5.2.

Mathematically speaking, the dispersion relation is obtained by setting  $E_{\phi_1} = E_{\phi_{11}} + E_{\phi_{12}}$ , and  $E_{\phi_2} = E_{\phi_{21}} + E_{\phi_{22}}$  equal to zero. The field components  $E_{\phi_{11}}$ ,  $E_{\phi_{12}}$ ,  $E_{\phi_{21}}$ , and  $E_{\phi_{22}}$ , are dependent on the distances  $R_{n_{11}}$ ,  $R_{n_{12}}$ ,  $R_{n_{21}}$ , and  $R_{n_{22}}$  respectively as explained in Chapter 3. Hence, an

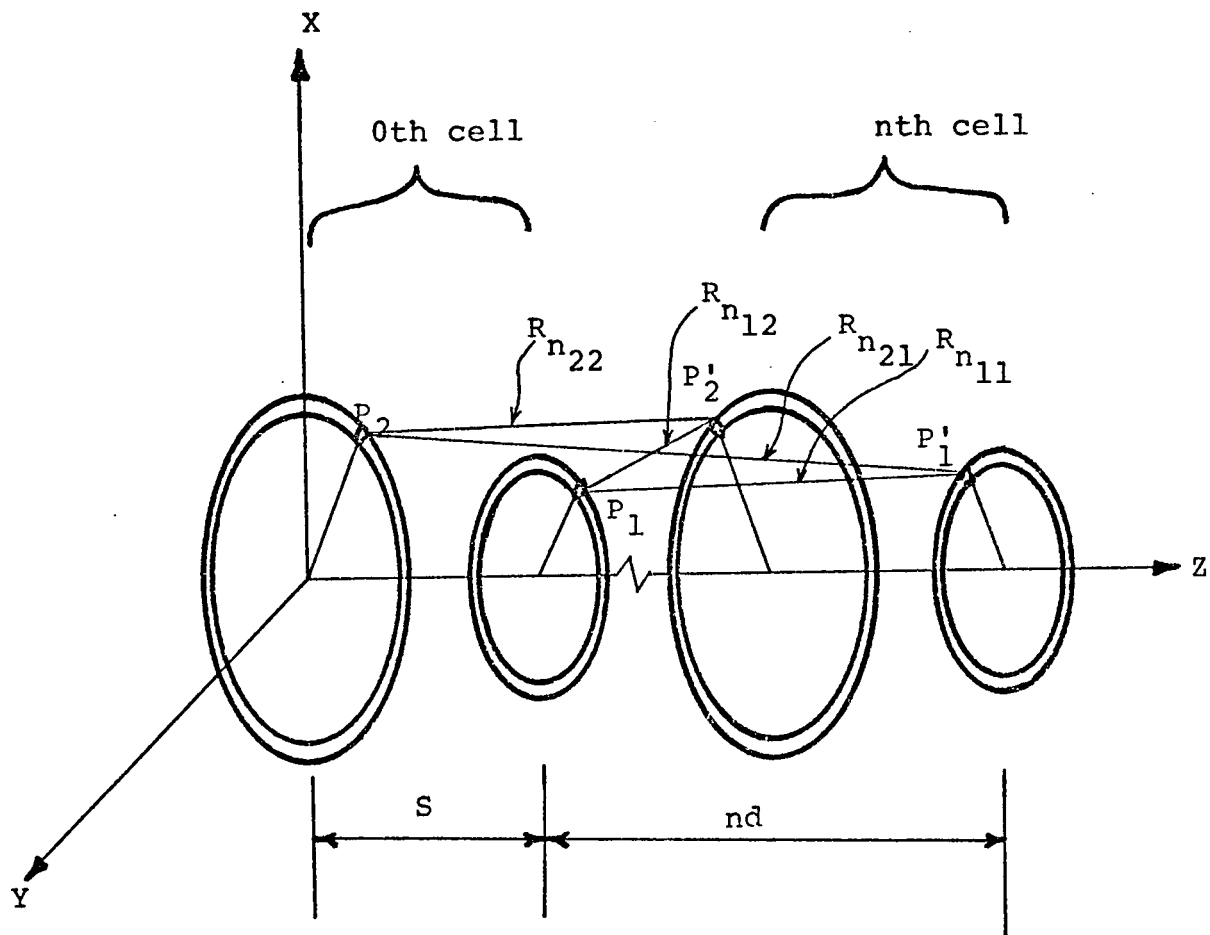


Fig. 5.2 Typical field and source points with associated distances.

evaluation of the  $R'_n$  is necessary before any field computations can be made.

### 5.2.1 Evaluation of the $R'_n$ 's

The expressions for  $R_{n11}$  and  $R_{n22}$  are identical to those obtained in Chapter 3 for the concentric array.

Namely,

$$R_{n11}^2 = 4b_1^2 \sin^2 [(\phi - \phi')/2] + 4a_1^2 \sin^2 [(\theta_1 - \theta'_1)/2] + n^2 d^2 \quad (5.2)$$

$$R_{n22}^2 = 4b_2^2 \sin^2 [(\phi - \phi')/2] + 4a_2^2 \sin^2 [(\theta_2 - \theta'_2)/2] + n^2 d^2 \quad (5.3)$$

with the conditions

$$a_1 \ll b_1; \quad 4a_1 \ll d; \quad a_2 \ll b_2; \quad 4a_2 \ll d \quad (5.4)$$

However, the expressions for  $R_{n12}$  and  $R_{n21}$  are not as obvious. Thus, a detailed derivation of  $R_{n21}$  will be made. Then,  $R_{n12}$  will be obtained by inspection of the result for  $R_{n21}$ .

$R_{n21}$  is defined by

$$R_{n21}^2 = |\vec{r}_{02} - \vec{r}'_{n1}|^2 \quad (5.5)$$

where  $\vec{r}_{02} = x_2 \hat{x} + y_2 \hat{y} + z_2 \hat{z}$  and  $\vec{r}'_{n1} = x'_1 \hat{x} + y'_1 \hat{y} + z'_1 \hat{z}$   
with components given as

$$x_2 = (b_2 - a_2 \cos \theta_2) \cos \phi \quad (5.6a)$$

$$y_2 = (b_2 - a_2 \cos \theta_2) \sin \phi \quad (5.6b)$$

$$z_2 = a_2 \sin \theta_2 \quad (5.6c)$$

and,

$$x'_1 = (b_1 - a_1 \cos \theta'_1) \cos \phi' \quad (5.7a)$$

$$y'_1 = (b_1 - a_1 \cos \theta'_1) \sin \phi' \quad (5.7b)$$

$$z'_1 = nd + s + a_1 \sin \theta'_1 \quad (5.7c)$$

Using (5.6) and (5.7) in (5.5), the expression for  $R_{n21}$   
becomes

$$\begin{aligned} R_{n21}^2 &= [(b_2 - a_2 \cos \theta_2) \cos \phi - (b_1 - a_1 \cos \theta'_1) \cos \phi']^2 \\ &\quad + [(b_2 - a_2 \cos \theta_2) \sin \phi - (b_1 - a_1 \cos \theta'_1) \sin \phi']^2 \\ &\quad + [a_2 \sin \theta_2 - nd - s - a_1 \sin \theta'_1]^2 \quad (5.8) \end{aligned}$$

Following the same steps used to simplify the expression  
for  $R_{n21}$  in section 3.2.3, one may reduce (5.8) to obtain

$$R_{n_{21}}^2 = (b_2 - b_1)^2 + 4 b_1 b_2 \sin^2 [(\phi - \phi')/2] + (nd + S)^2 - 2S(a_2 \sin \theta_2 - a_1 \sin \theta_1') \quad (5.9)$$

subject to the conditions

$$2(a_1 + a_2) \ll d; \quad 2(a_1 + a_2) \ll b_2 - b_1; \quad (a_1/b_1) + (a_2/b_2) \ll 1 \quad (5.10)$$

As shown in Appendix D, the last term in equation (5.9) may be neglected provided the parameter  $S$  satisfies the inequality

$$0 \leq S \leq d/2 \quad (5.11)$$

Then, the expression for  $R_{n_{21}}$  reduces to

$$R_{n_{21}}^2 = (b_2 - b_1)^2 + 4 b_1 b_2 \sin^2 [(\phi - \phi')/2] + (nd + S)^2 \quad (5.12)$$

Finally, the expression for  $R_{n_{12}}$  may be obtained from (5.12) upon replacing  $S$  by  $-S$ . This yields

$$R_{n_{12}}^2 = (b_2 - b_1)^2 + 4 b_1 b_2 \sin^2 [(\phi - \phi')/2] + (nd - S)^2 \quad (5.13)$$

which is valid subject to the conditions of (5.10) and (5.11).

### 5.2.2 Evaluation of the field components

$E_{\phi_{11}}$  for the array of coaxially displaced loops may be obtained from that for the array of concentric loops (Eq. 3.58) upon replacing  $A_1 \cos m\phi$  by  $A_1 \cos m\phi e^{-j\beta S}$ . that is

$$E_{\phi_{11}} = \frac{jA_1 \eta_0 K b_1 \cos m\phi e^{-j\beta S}}{d} \sum_n \left\{ \left( \frac{m\beta_n}{K b_1 \gamma_n} \right)^2 I_m(\gamma_n b_1) K_m(\gamma_n b_1) \right. \\ \left. + I'_m(\gamma_n b_1) K'_m(\gamma_n b_1) \right\} S(2\gamma_n a_1) \quad (5.14)$$

However,  $E_{\phi_{22}}$  is exactly the same as the one for the concentric array (Eq. 3.59). Namely,

$$E_{\phi_{22}} = \frac{jA_2 \eta_0 K b_2 \cos m\phi}{d} \sum_n \left\{ \left( \frac{m\beta_n}{K b_2 \gamma_n} \right)^2 I_m(\gamma_n b_2) K_m(\gamma_n b_2) \right. \\ \left. + I'_m(\gamma_n b_2) K'_m(\gamma_n b_2) \right\} S(2\gamma_n a_2) \quad (5.15)$$

In order to determine  $E_{\phi_{21}}$ , it is necessary to study the expression for its Kernel  $W_{21}(\phi - \phi')$  given by

$$W_{21}(\phi - \phi') = \frac{1}{2\pi} \int_{-\pi}^{\pi} d\theta'_1 \sum_{n=-\infty}^{+\infty} e^{-j\beta(nd+s)} \frac{e^{-jKR_{n21}}}{R_{n21}} \quad (5.16)$$

By decomposing  $R_{n21}$  into two parts, the expression for the Kernel becomes

$$W_{21}(\phi-\phi') = \frac{1}{2\pi} \int_{-\pi}^{\pi} d\theta'_1 \sum_{n=-\infty}^{+\infty} e^{-j\beta(nd+S)} \frac{e^{-jK\sqrt{(nd+S)^2+A^2}}}{\sqrt{(nd+S)^2+A^2}} \quad (5.17)$$

where  $A^2 = (b_2 - b_1)^2 + 4b_1b_2 \sin^2 [(\phi - \phi')/2]$ .

An equivalent representation to (5.17) may be obtained by invoking another form of the Poisson's summation formula [51].

$$\sum_{n=-\infty}^{+\infty} f(S+nd) = \frac{1}{d} \sum_{m=-\infty}^{+\infty} e^{j \frac{2\pi m S}{d}} F\left(\frac{2\pi m}{d}\right) \quad (5.18)$$

where  $F$  denotes the exponential Fourier transform of the function  $f$ . Using (5.18) along with the definition of Fourier transform in (5.17) the Kernel may be written as

$$W_{21}(\phi-\phi') = \frac{1}{2\pi} \int_{-\pi}^{\pi} d\theta'_1 \left\{ \frac{1}{d} \sum_{m=-\infty}^{+\infty} e^{j \frac{2\pi m S}{d}} \int_{-\infty}^{+\infty} e^{-jt(\beta + \frac{2\pi m}{d})} \frac{e^{-jK\sqrt{A^2 + t^2}}}{\sqrt{A^2 + t^2}} dt \right\} \quad (5.19)$$

Substituting  $\beta_m = \beta + 2\pi m/d$ , and integrating the indefinite integral in (5.19), yields

$$W_{21}(\phi-\phi') = \frac{1}{\pi d} \int_{-\pi}^{\pi} d\theta'_1 \sum_{n=-\infty}^{+\infty} e^{j \frac{2\pi n S}{d}} K_0(A\gamma_n) \quad (5.20)$$

where  $\gamma_n^2 = \beta_n^2 - K^2$ , and  $K_0$  is the modified Bessel function.

From section 3.2.7,  $E_{\phi 21}$  is given by

$$E_{\phi 21} = \frac{-jA_1}{4\pi\omega\epsilon_0 b_2} \left\{ -m^2 \int_{-\pi}^{\pi} d\phi' \cos m\phi' W_{21}(\phi-\phi') \right. \\ \left. + K^2 b_1 b_2 \int_{-\pi}^{\pi} d\phi' \cos(\phi-\phi') \cos m\phi' W_{21}(\phi-\phi') \right\} \quad (5.21)$$

By replacing the Kernel  $W_{21}(\phi-\phi')$  with its value from (5.20) into (5.21), and following the same steps as in 3.2.7, the final expression for  $E_{\phi 21}$  results.

$$E_{\phi 21} = \frac{jA_1 \eta_0 K b_1 \cos m\phi}{d} \sum_n e^{j \frac{2\pi n S}{d}} \left\{ \left( \frac{m\beta_n}{K b_0 \gamma_n} \right)^2 I_m(\gamma_n b_1) \right. \\ \left. K_m(\gamma_n b_2) + I_m'(\gamma_n b_1) K_m'(\gamma_n b_2) \right\} \quad (5.22)$$

where  $b_0 = b_1 b_2$ .

Finally, the field component  $E_{\phi 12}$  has the following Kernel

$$W_{12}(\phi-\phi') = \frac{1}{2\pi} \int_{-\pi}^{\pi} d\theta'_2 \sum_{n=-\infty}^{+\infty} e^{-j\beta n d} \frac{e^{-jKR_{n12}}}{R_{n12}} \quad (5.23)$$

Using  $R_{n12}^2 = A^2 + (nd-S)^2$ , and factoring  $e^{-j\beta S}$  yields

$$W_{12}(\phi-\phi') = \frac{e^{-j\beta S}}{2\pi} \int_{-\pi}^{\pi} d\theta'_2 \sum_{n=-\infty}^{+\infty} e^{-j\beta(nd-S)} \frac{e^{-jK\sqrt{(nd-S)^2+A^2}}}{\sqrt{(nd-S)^2+A^2}} \quad (5.24)$$

Applying Poisson's summation formula to (5.24), the Kernel becomes

$$W_{12}(\phi-\phi') = \frac{e^{-j\beta S}}{\pi d} \int_{-\pi}^{\pi} d\theta'_2 \sum_{n=-\infty}^{+\infty} e^{-j\frac{2\pi n S}{d}} K_0(A\gamma_n) \quad (5.25)$$

From section 3.2.8,  $E_{\phi_{12}}$  is given by

$$E_{\phi_{12}} = \frac{-jA_2}{4\pi\omega\epsilon_0 b_1} \left\{ -m^2 \int_{-\pi}^{\pi} d\phi' \cos m\phi' W_{12}(\phi-\phi') \right. \\ \left. + K^2 b_1 b_2 \int_{-\pi}^{\pi} d\phi' \cos(\phi-\phi') \cos m\phi' W_{12}(\phi-\phi') \right\} \quad (5.26)$$

By replacing  $W_{12}(\phi-\phi')$  with its value from (5.25), and following the usual procedure, the final expression for  $E_{\phi_{12}}$  results.

$$E_{\phi_{12}} = \frac{jA_2 \eta_0 K b_2 \cos m\phi e^{-j\beta S}}{d} \sum_n e^{-j\frac{2\pi n S}{d}} \left\{ \left( \frac{m\beta_n}{K b_0 \gamma_n} \right)^2 I_m(\gamma_n b_1) \right. \\ \left. K_m(\gamma_n b_2) + I'_m(\gamma_n b_1) K'_m(\gamma_n b_2) \right\} \quad (5.27)$$

### 5.2.3 Dispersion relation

Setting  $E_{\phi_1} = E_{\phi_2} = 0$  for all values of  $\phi$  yields two simultaneous equations for the unknown current amplitudes.

$$b_1 A_1 \cos m\phi(T_{11}) + b_2 A_2 \cos m\phi(T_{12}) = 0 \quad (5.28a)$$

$$b_1 A_1 \cos m\phi(T_{21}) + b_2 A_2 \cos m\phi(T_{22}) = 0 \quad (5.28b)$$

where

$$T_{11} = \sum_n \left[ \frac{m\beta_n}{Kb_1\gamma_n} \right]^2 \left[ I_m(\gamma_n b_1) K_m(\gamma_n b_1) + I'_m(\gamma_n b_1) K'_m(\gamma_n b_1) \right] S(2\gamma_n a_1) \quad (5.29a)$$

$$T_{22} = \sum_n \left[ \frac{m\beta_n}{Kb_2\gamma_n} \right]^2 \left[ I_m(\gamma_n b_2) K_m(\gamma_n b_2) + I'_m(\gamma_n b_2) K'_m(\gamma_n b_2) \right] S(2\gamma_n a_2) \quad (5.29b)$$

$$T_{12} = \sum_n \left[ \frac{m\beta_n}{Kb_o\gamma_n} \right]^2 \left[ I_m(\gamma_n b_1) K_m(\gamma_n b_2) + I'_m(\gamma_n b_1) K'_m(\gamma_n b_2) \right] e^{-j\frac{2\pi n S}{d}} \quad (5.29c)$$

$$T_{21} = \sum_n \left[ \frac{m\beta_n}{Kb_o\gamma_n} \right]^2 \left[ I_m(\gamma_n b_1) K_m(\gamma_n b_2) + I'_m(\gamma_n b_1) K'_m(\gamma_n b_2) \right] e^{j\frac{2\pi n S}{d}} \quad (5.29d)$$

For a nontrivial solution, the determinant of the coefficients in (5.29) must be zero; namely,

$$T_{11}T_{22} - T_{12}T_{21} = 0 \quad (5.30)$$

Equation (5.30) is the required dispersion relation. Also, the ratio of the current amplitudes is given by

$$\frac{A_1}{A_2} = - \begin{pmatrix} b_2 \\ b_1 \end{pmatrix} \begin{pmatrix} T_{12} \\ T_{11} \end{pmatrix} \quad (5.31)$$

### 5.3 NUMERICAL RESULTS

Since the series  $T_{12}$  and  $T_{21}$  in (5.30) are complex conjugates, their product is a real number, and hence the determinant is a real-valued function of the phase delay  $\Phi$ . Thus, the computer program described in section 3.3 may be used, with appropriate modifications, to obtain solutions for equation (5.30).

It is noteworthy to indicate that the only difference between the dispersion relation for the array of coaxially displaced loops, and that of the concentric array of loops, is the existence of phase factors in the series  $T_{12}$  and  $T_{21}$ . However, these factors do not contribute to the  $n=0$  terms of the two series. Since the fundamental term ( $n=0$ ) of each series is dominant over most of the passbands, it is expected that no significant change in phase velocity of the propagating wave would result when the loops of a concentric array are axially displaced. This fact has been verified with an array having the parameters

( $a/b_1=0.01$ ,  $d/b_1=0.25$ , and  $b_2/b_1=1.25$ ) whose loops have been displaced an amount  $S=d/2$ . The results for both the concentric and the displaced arrays are given in Table XI for comparison.

Near the ends of the passbands, the fundamental term can no longer be considered the dominant term, and a slight difference between the phase velocities exists. For example, in the first passband, a difference appears in the frequency range between  $Kb_1=0.78$  and  $Kb_1=0.80$ . However, in the second passband, a difference exists in the range between  $Kb_1=0.98$  and  $Kb_1=1.02$ . In any case, the change in phase velocity is small and may be neglected.

Finally, it should be noted that the analysis presented in this chapter is valid for any amount of displacement. In fact, if in Fig. 5.1 the small loops were displaced in the negative  $z$ -direction instead, the dispersion relation of equation (5.30) would still hold. Actually, a displacement to the left results in an interchange of the expressions for  $R_{n12}$  and  $R_{n21}$ , which indicates an interchange in the expressions for  $T_{12}$  and  $T_{21}$ . Hence, the theory derived above is valid for any relative displacement between the inner and outer loops. This is obviously the case since the parameter  $S$  can vary over one full period ( $-d/2 \leq S \leq d/2$ ).

TABLE XI

Normalized phase velocity of  $m=1$  mode $(a/b_1=0.01, d/b_1=0.25, b_2/b_1=1.25, S/d=0.5)$ 

$Kb_1$	Displaced	Concentric
————— first passband —————		
0.50	0.9867	0.9867
0.52	0.9814	0.9814
0.54	0.9738	0.9738
0.56	0.9655	0.9655
0.58	0.9542	0.9542
0.60	0.9405	0.9405
0.62	0.9247	0.9247
0.64	0.9064	0.9064
0.66	0.8842	0.8842
0.68	0.8575	0.8575
0.70	0.8261	0.8261
0.71	0.8075	0.8075
0.72	0.7875	0.7875
0.73	0.7640	0.7640
0.74	0.7378	0.7378
0.75	0.7071	0.7071
0.76	0.6702	0.6702
0.77	0.6249	0.6249
0.78	0.5657	0.5653
0.79	0.4781	0.4777
0.80	0.2796	0.2777
————— second passband —————		
0.95	0.9747	0.9747
0.96	0.9250	0.9250
0.97	0.8712	0.8712

TABLE XI (cont'd)

0.98	0.8172	0.8177
0.99	0.7616	0.7621
1.00	0.7011	0.7015
1.002	0.6880	0.6884
1.002	0.1210	0.1198
1.004	0.6740	0.6743
1.004	0.1594	0.1588
1.006	0.6596	0.6599
1.006	0.1883	0.1877
1.008	0.6442	0.6488
1.008	0.2139	0.2134
1.010	0.6277	0.6284
1.010	0.2380	0.2375
1.012	0.6102	0.6104
1.012	0.2618	0.2613
1.014	0.5904	0.5909
1.014	0.2865	0.2860
1.016	0.5676	0.5684
1.016	0.3133	0.3127
1.018	0.5399	0.5408
1.018	0.3445	0.3437
1.020	0.4998	0.5011
1.020	0.3875	0.3864

## CHAPTER 6

## DISCUSSION OF POSSIBLE APPLICATIONS

## 6.1 AN OVERVIEW

The purpose of this chapter is to present an account of possible applications of the periodic structure of circular loops and variations thereof. The presentation is intended to illustrate the useful features and properties of the structure, and their potential application in the design of practical devices.

The usefulness of any open periodic structure stems from its ability to propagate a low-loss slow surface-wave in one, two, or more passbands. In the case of the periodic structure of circular loops and its derivatives, the property of slow wave propagation can take on added dimensions resulting in new and varied applications. For example, its applicability to the design of Yagi antennas, surface waveguides, microwave filters, TWT interaction circuits, and open resonators is discussed in the next section. Whenever possible, a description of existing hardware that offer a certain degree of resemblance to the loop structure is also included.

## 6.2 AREAS OF POSSIBLE APPLICATION

## 6.2.1 Yagi Antenna

As shown in chapter 2, a section of an infinitely long Yagi array of single loops may be transformed into a

Yagi antenna by connecting one end to a signal source and terminating the other end in free space. The antenna thus formed has a linearly polarized endfire beam in the first mode, and a linearly polarized conical-shell beam in the second mode. Moreover, its directivity in the first mode of operation is comparable to that of a dipole array of the same length. Also, the radiation characteristics in the two modes are particularly suited to coarse/fine tracking applications. In addition, circular polarization may be realized by proper reactive loading of the array [15].

In the case of the concentric array, a broadband Yagi antenna with an operational bandwidth extending over the pass- and stop- bands may be designed. Obviously, the success of this antenna depends largely on the attenuation experienced by the surface wave in the stop band. Note also that the directivity of such an antenna is lower than that of a single array due to the out-of-phase currents on the inner and outer loops. In any case, a concentric array of circular loops may be a desirable alternative when a tradeoff between gain and bandwidth can be tolerated.

A new and important feature that may be used to advantage in Yagi antenna design, is discussed in Chapter 5. It is shown there that the phase velocity of the propagating wave and the amplitudes of the loop currents remain un-

changed under an arbitrary relative displacement of inner to outer loops. This means that the gain of the Yagi antenna is not a function of the relative displacement. However, the shift in phase between the currents of the displaced loops, is directly proportional to the amount of displacement. This fact may be used as an independent control to achieve limited beam steering and/or desirable pattern shaping. Hence, a Yagi antenna formed by coupled arrays of coaxial loops, enjoys the advantages of large bandwidth and pattern controllability at the expense of some reduction in gain.

#### 6.2.2 Surface Waveguide

In Japan, open-structure surface waveguides have been the subject of numerous investigations directed toward their application in railway traffic control. A typical railway radar system consists of surface waveguides placed along the track and a train-mounted radar transceiver. The output from the radar transmitter is coupled to the waveguide, and is propagated along the guide as a surface wave. Some portion of the wave energy is reflected by the discontinuities of the guide itself or of the surrounding space of the guide. This system is regarded as a kind of one-dimensional radar system. It has the function of locating the preceding trains on the track, and the obstacles

near the guide. The radar system gathers such information as the distance to the preceding trains, and their relative speeds. This information, together with such data as the speed and the position of the train itself, can be used to achieve automatic train control [59].

The surface waveguides installed along the tracks must have a strong and stable structure to withstand wind pressure, vibration, temperature change, and all kinds of weather. An array of half-loops arranged over an image plane is a continuous self-supporting structure that is well suited for this purpose. In fact, it is more than a substitute for the corrugated metal surfaces now in use. Also, if wideband operation is desired, the concentric array of half-loops may be used instead.

Unlike the cylindrical or coaxial waveguide, the field pattern of the propagating mode on the array structure of circular loops may not be classified as a TE or TM mode. For example, the loop array has the same transverse current ( $\cos \phi$ ) as a  $TE_{11}$  mode of a cylindrical waveguide, but lacks its axial current. On the other hand, the  $TE_{01}$  mode of a cylindrical waveguide has the same property of zero axial current as the propagating mode on the loop array, however it differs greatly in its transverse current. In the former, the transverse current is uniform, while in

the latter, it is cosinusoidal. Moreover, near-field calculations made on the loop array suggest that a hybrid designation (HE or EH) is more appropriate to describe its propagating mode.

A structure that bears some resemblance to the loop array was investigated recently at the University of Limoges, France [60]. This is the open-ring line structure shown in Fig. 6.1. The mode that propagates on such a

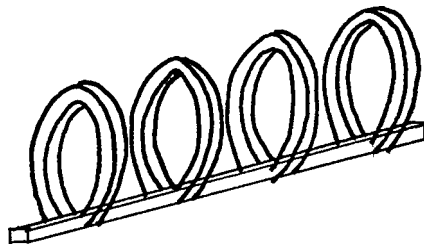


Fig. 6.1. The open-ring line structure.

structure was found to be an  $HE_{11}$  hybrid dipolar mode. The line, made of aluminum alloy, had an attenuation of less than 5dB per kilometer at frequencies below 1.8 GHz. Also, the attenuation in the line was found to be relatively insensitive to the thickness and width of the rod, or of the rings.

Propagation of the hybrid dipolar mode  $HE_{11}$  has some inherent advantages. First, it consists of single mode transmission all the way down to zero frequency [59]. Second, the surface wave on the line may be readily

launched by means of a tapered transition into a cylindrical waveguide operating in the dominant  $TE_{11}$  mode. Since the field of the exciter is identical to a part of the surface-wave field, the surface wave may be launched with reasonable efficiency. One disadvantage however, is the possible rotation of polarization at points of surface line defects.

The potential use of periodic structures of circular loops as transmission lines, depends to a large extent upon their attenuation characteristics due to ohmic losses. The attenuation per unit length is expected to be lower than that obtained with the open-ring line. The absence of the axial rod results in zero axial current and hence considerably lower ohmic losses which translate into lower attenuation per unit length. Aside from ohmic losses, there will also be attenuation due to power scattered by deviations from the ideal periodic geometry, and by reflection of the surface wave from existing nearby objects. However, whereas the latter losses can be reduced by greater care in manufacture, and array isolation, the ohmic losses represent a more intrinsic limitation.

### 6.2.3 TWT Interaction Circuit

The function of a traveling-wave-tube interaction circuit is to amplify the RF signal applied to its input by means of interaction between its slow surface-wave, and

the space charge wave of the electron beam. For strong coupling, the phase velocity of the slow-wave circuit must be nearly equal to that of the electron beam. The latter is determined by the voltage  $V$  applied to the electron gun ( $v=5.9 \times 10^5 \sqrt{V}$  m/s). For a typical voltage of 10 KV, the normalized phase velocity of the wave should be about 0.2 ( $v/c \approx 0.2$ ). This velocity is considerably lower than that obtained with the periodic array of circular loops. Hence, the structure of circular loops is unsuitable in its present form as an interaction circuit due to the prohibitively high voltages required. Therefore, ways of making the wave slower are necessary before the loop circuit can be used. This may be done by dielectric loading of the array structure.

The interaction impedance of a periodic slow-wave circuit is a measure of the strength of the axial electric field of a given space harmonic referred to the total power carried by the mode. For the  $K$ th space harmonic, the interaction impedance is given by [50]

$$Z_K = \frac{E_{zK}^2}{2\beta_K^2 P_z} \quad (6.1)$$

It is important to have a high interaction impedance for the fundamental mode ( $K=0$ ), since this means that most of

the power is carried by the fundamental wave and a negligible amount in the space harmonics. This will result in high gain per wavelength and high RF efficiency. Even more important is the necessity to have a low interaction impedance corresponding to the -1 space harmonic wave, since it can result in backward-wave oscillations.

Ordinarily, the interaction circuit in traveling-wave tubes is shielded by a metal conductor. When the circuit is placed inside such a conducting cylinder, there exist fast-wave modes in addition to the surface-wave mode with its slow phase velocity. The slow-wave mode is the operating mode and the fast-wave modes are spurious. For these spurious modes there are well defined cutoff frequencies, the mode with the longest cutoff wavelength corresponding to the  $TE_{11}$  mode of the coaxial line. In millimeter-wave tubes where such spurious modes can exist, a part of the energy from the input circuit is converted to the spurious modes as the surface wave mode is excited. The surface-wave mode interacts with the beam to produce amplification, while the spurious modes propagate through the space surrounding the circuit. At the output terminal, part of the spurious signal is reflected and returns to the input end. A part of the amplified slow-wave mode also is converted to the spurious mode at the output and returns

to the input. At the input these reflected signals interfere with the input signal to produce undesirable effects on the gain-frequency characteristic of the tube [61].

Hence, an ideal interaction circuit is one that has 1) a high interaction impedance for the fundamental wave, 2) a low interaction impedance for the  $-1$  space harmonic wave and, 3) a minimizing effect on the excitation of spurious modes.

Historically, the first structure to be used as an interaction circuit was the helix depicted in Fig. 6.2. The relatively high interaction impedance of the  $-1$  space harmonic makes the helix a useful structure in backward-

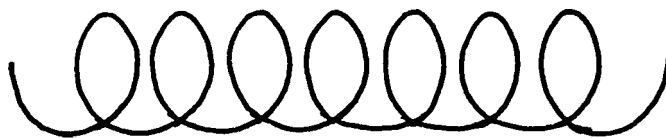


Fig. 6.2. The helical circuit.

wave oscillators. However, this characteristic is disadvantageous in helix-type traveling-wave tube amplifiers. Therefore, the use of deliberately introduced loss that is reciprocal is essential in simple helix-type traveling-wave tube structures. This loss is required in order to avoid regeneration or oscillation resulting from reflections at the helix terminals, as well as to damp oscillations caused

by backward-wave interaction. Unfortunately such loss reduces gain and efficiency, does not always eliminate backward-wave oscillations, and can result in large fluctuations in the gain-frequency characteristic [13]. Also, since the helix is physically continuous in the axial direction, a path for the axial current necessary for the excitation of the higher-order coaxial spurious mode ( $TE_{11}$ ), is provided. So, in order to minimize the excitation of the spurious mode at the input and output ends, and to provide sufficient attenuation for the spurious mode once excited, short section of cutoff guide are usually placed at each end of the tube along with lossy material positioned parallel to the helix. Although this improves the frequency response of the amplifier, it does however reduce the gain appreciably.

As opposed to the helical structure, the ring-bar circuit of Fig. 6.3 consists of equally spaced rings and connecting bars. Compared to the helix, it has a larger

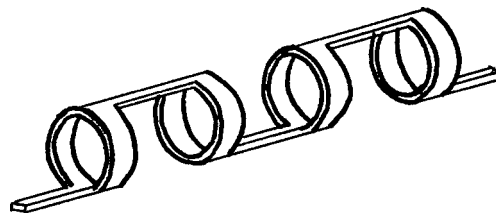


Fig. 6.3. The ring-bar circuit.

phase velocity for a given  $K_b$ , and its dispersion is greater; that is, its group velocity changes more rapidly. In the useful range of  $K_b$  and  $v/c$ , the interaction impedance of the fundamental component of the ring-bar circuit is about twice that for the helix, and the interaction impedance of the space harmonics is reduced by factors of the order of five-to-ten [13]. This results in a marked advantage of the ring-bar circuit over the helix for high power applications. Like the helix, the ring-bar circuit is axially continuous and has no advantage as far as suppression of spurious modes.

The ring-loop structure, first conceived as a low cost replacement for the older ring-bar structure, is shown in Fig. 6.4. The widely spaced thin rings combine with the transmission line effect of the radially-extended loop to maximize energy stored in the desired fundamental, and minimize the energy stored in the  $-1$  space harmonic which causes backward-wave oscillation [62]. This translates into high fundamental interaction impedance, which results in high gain per wavelength and high RF efficiency. On the other hand, the radially extended loops located between successive rings tend to partially suppress the excitation of spurious modes. The latter property results in good gain-frequency characteristics and low harmonic output

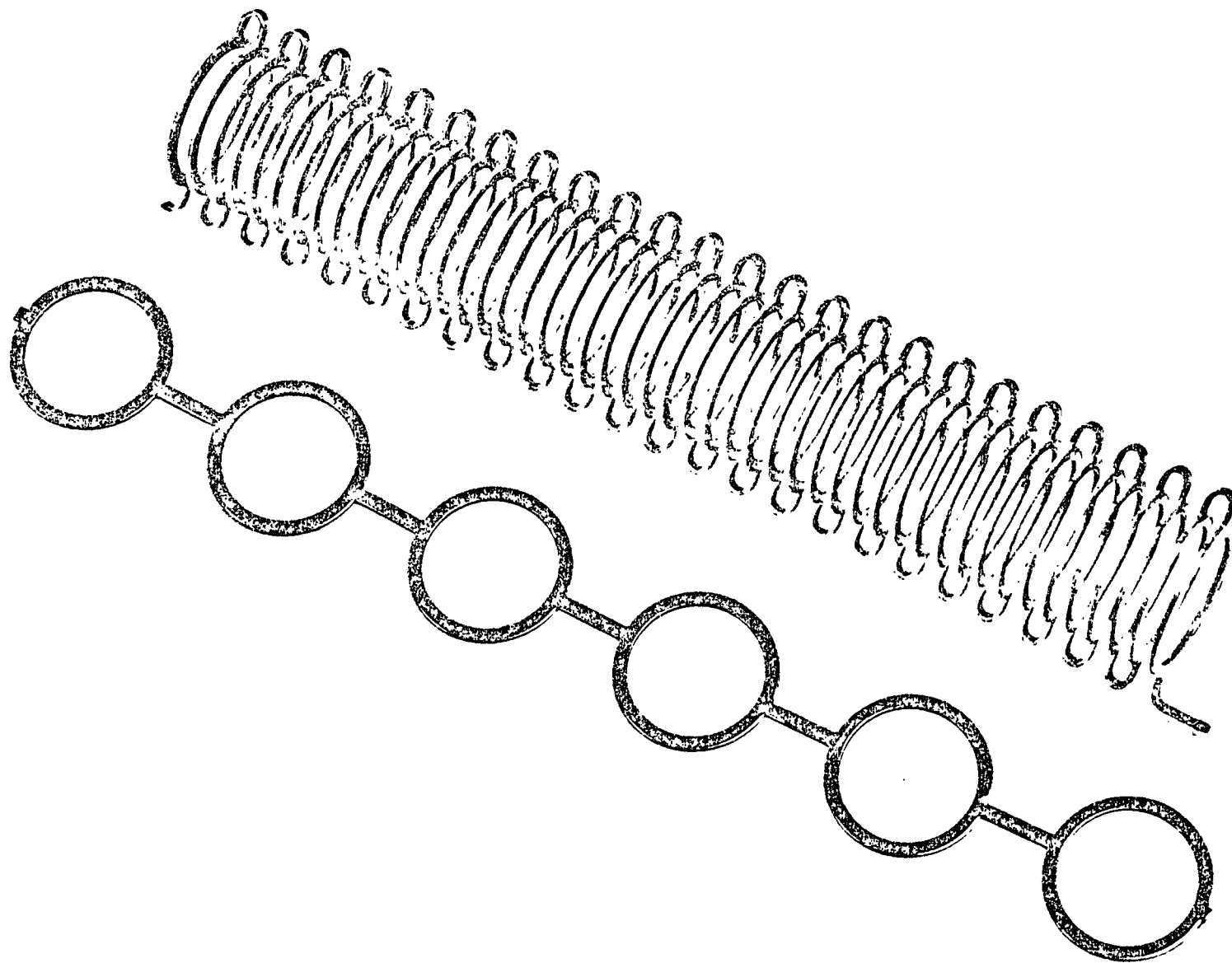


Fig. 6.4. The ring-loop circuit before and after folding.  
(Courtesy of Litton Electron Tube Division).

typically 30 to 35 dB down. The operating voltage of the ring-loop circuit is established by the ring-to-ring spacing. The ring spacing is changed simply by changing the spacers used in folding the circuit. By adjusting the slow wave circuit pitch over wide ranges, it is possible to provide any peak power from one to 10 KW anywhere in x-band, with 8% bandwidth at 65 dB gain [62].

In conclusion, the periodic array of loops is similar to the ring-bar circuit except for the connecting bars, and to the ring-loop circuit except for the folding loops. These extra conducting elements serve to slow the wave down by making the phase delay  $\phi$  between successive rings larger. Thus, the periodic array of loops may be adapted to perform as an interaction circuit with properties far superior to those of the conventional helix. Moreover, in the form of a periodic array of concentric loops, other functions such as power transfer and attenuation may be accomplished. In this case the outer array, located outside the tube, serves to couple energy to and from the inner array located within the tube structure.

#### 6.2.4 Microwave Filter

Microwave filter art is filled with examples of closed periodic structures such as the periodically loaded waveguide and the multicavity resonator. In these struc-

tures, the input impedance becomes reactive in the stopband, resulting in reflection of input power. These filters have in general a mode-dependent filtering characteristic. In an open periodic structure however, the "openness" property permits the use of the forbidden region (stopband) to achieve filtering. This allows the realization of frequency-dependent, rather than mode-dependent, filters which are well matched in both pass and stop bands [63].

The ability of the open periodic structure of concentric loops to sustain the same propagating mode in two distinct passbands makes this structure unique, as far as the author is aware, in its application to filtering. A dual-band (or band-reject) filter may be designed using a section of the periodic array of concentric loops. The structure would be physically enclosed by a conducting shield to prevent radio interference. Its "openness" would be realized by the use of an absorptive liner within the outer conducting shell of the assembly. Within the passbands, the insertion loss may be kept at a minimum by careful design of matched transitions from a coaxial line to the loop array structure. Some of the insertion loss will be due to the proximity of the absorber to the structure, and the rest due to reflections at the input and output ends.

Finally, this type of filter design has certain inherent disadvantages. For example, the attenuation rate in the stopband depends on the absorber shape, location, and material, and on the overall length of the filter structure. Also, the problem of direct radiation from input to output in the stopband may not be completely eliminated.

#### 6.2.5 Open-structure Resonator

A high  $Q$  ( $>1000$ ) open-structure resonator may be formed by terminating a section of the periodic array of copper loops by two large, parallel, and flat reflectors. Efficient cavity coupling may be made by a probe in the case of the isolated array, and by a loop (or two probes) in the case of the concentric array. Open resonators of this type have been used as diagnostic devices to study the properties of plasma-like media.

## CHAPTER 7

## CONCLUSION

Wave propagation on the infinitely long Yagi array of concentric circular loops has been analyzed. For the same propagating mode, the concentric array exhibits two disjoint passbands separated by a stopband. The first passband corresponds to the near resonance of the outer loop, while the second passband corresponds to the near resonance of the inner loop. The width of each of the pass-and stop-bands is a function of the ratio of radii  $b_2/b_1$ . Currents on the inner and outer loops are generally  $180^\circ$  out of phase with amplitudes in the ratio 2:1 or larger depending on frequency.

The theoretically determined phase velocities were verified quite well by experimental measurement. However, the experiment failed to detect the dual-wave behavior that takes place near the end of the second passband.

It was also shown that the propagation characteristics of the concentric array of loops are unaffected by an arbitrary displacement between inner and outer loops. The only change appears as a phase shift in the currents

of the displaced loops. This phase shift is directly proportional to the amount of displacement. The latter property may be used to achieve desired pattern shaping and/or beam steering of Yagi antennas.

When the outer loop is removed to infinity, the concentric array reduces to an isolated array of single loops with one passband per mode. The phase velocities of the propagating waves on the isolated array were used to obtain optimum design parameters for the Yagi antenna of circular loops. In the first mode of operation, the Yagi antenna of circular loops radiates mainly in the endfire direction, and in the second mode, the radiation is in a conical shell pattern. This type of antenna is extremely well suited for coarse/fine tracking applications.

The Yagi array of concentric loops and its derivatives may have other practical applications. They may be transformed into broadband Yagi antennas, low-loss surface waveguides, highly efficient TWT interaction circuits, microwave filters with unique properties, and high-Q open structure resonators.

As a way of motivation for future research in the general area of the Yagi array of loops, it is reasonable to point out few, still unresolved, research problems.

(1) Evaluation of the ohmic loss per unit length on the periodic structure of circular loops. This para-

meter is needed when the array is used as a surface waveguide.

(2) Analysis of the loaded array of circular loops. Resistive loading may lead to band broadening and pattern shaping, and reactive loading may result in circular polarization.

(3) Experimental study of the far-field pattern of the concentric array of circular loops throughout the frequency range covering the pass-and stop-bands. The objective here is to determine the feasibility of this structure as a broadband antenna.

In summary, this study has revealed significant facts concerning the analysis and applications of the infinitely long Yagi array of concentric loops and its variations. It is felt that this work will help to fill the need for a systematic and elaborate investigation into the usefulness of these and other related structures. Furthermore, a short but direct path leading to more innovative and exciting research into the area, has also been proposed.

## REFERENCES

- [1] E. Hallen, "Theoretical Investigation Into Transmitting and Receiving Qualities of Antennae," *Nova Acta Uppsala*, Vol. 4, pp. 1-44, 1938.
- [2] J. E. Storer, "Impedance of Thin-wire Loop Antennas," *Trans. AIEE (Communication and Electronics)*, Vol. 75, pp. 606, November 1956.
- [3] T. T. Wu, "Theory of Thin Circular Loop Antennas," *J. Math. Phys.*, Vol. 3, pp. 1301-1304, November-December 1962.
- [4] K. Iizuka, "The Circular Loop Antenna Multiloaded With Positive and Negative Resistors," *IEEE Trans. Antennas and Propagation*, Vol. AP-13, pp. 7-20, January 1965.
- [5] R. L. Fante, J. J. Otazo, and J. T. Mayhan, "The Near Field of the Loop Antenna," *Radio Science*, Vol. 4, No. 8, pp. 697-701, August 1969.
- [6] R.W.P. King, "The Shunt-driven Circular Loop Antenna," *IEEE Trans. Antennas and Propagation*, Vol. AP-19, pp. 692-694, September 1971.
- [7] S. Adachi and Y. Mushiake, "Theoretical Formulation for Circular Loop Antennas by Integral Equation Method," *Report of the Research Inst. of Electrical Communications, Tohoku University, Sendai, Japan*, Vol. 9, No. 1, pp. 9-18, 1957.

- [8] \_\_\_\_\_, "Studies of large circular loop antennas," Report of the Research Inst. of Electrical Communications, Tohoku University, Sendai, Japan, Vol. 9, No. 2, pp.79-103, 1957.
- [9] A. Baghdasarian and D.J. Angelakos, "Scattering from Conducting Loops and Solution of Circular Loop Antennas by Numerical Methods," Proc. IEEE, Vol. 53, No. 8, pp. 818-822, August 1965.
- [10] N. Inagaki, T. Sekiguchi, and S. Ito, "A Theory of a Loop Antenna," Electronics and Communication in Japan, Vol. 53-B, No. 3, pp. 62-70, March 1970.
- [11] T. Kasahara, S. Adachi, and Y. Mushiake, "Calculation of the Impedances of Impedance-terminated Loop Antennas by the EMF Method," Electronics and Communication in Japan, Vol. 52-B, No. 3, pp. 73-80, March 1969.
- [12] R. E. Collin and F. J. Zucker, Eds., Antenna Theory, Parts I and II, New York; McGraw-Hill, 1969.
- [13] S. Sensiper, "Electromagnetic Wave Propagation on Helical Structures (A Review and Survey of Recent Progress)," Proc. IRE, Vol. 43, No. 2, p. 156, February 1955.
- [14] R. D. Kodis, L. C. Shen, and T. T. Wu, "Theory of Electromagnetic Wave Propagation on Array of Circular Loops," Private Communication.

- [15] M. Yamazawa, N. Inagaki, and T. Sekiguchi, "Analysis Method and Characteristics of Waves Propagating on an Infinite Array of Circular Loop Antennas," *Electronics and Communication in Japan*, Vol. 56-B, No. 5, pp. 76-82, May 1973.
- [16] J. R. Townes, "A User's Guide to PLTJRT," Technical Report, University of Missouri, August 1970.
- [17] J. E. Lindsay, "A Parasitic End-fire Array of Circular Loop Elements," *IEEE Trans. Antennas and Propagation*, Vol. AP-15, pp. 697-698, September 1967.
- [18] K. Iizuka, R.W.P. King, and C. W. Harrison, Jr., "Self- and Mutual Admittances of Two Identical Circular Loop Antennas in a Conducting Medium and in Air," *IEEE Trans. Antennas and Propagation*, Vol. AP-14, pp. 440-450, July 1966.
- [19] H. W. Ehrenspeck and H. Poehler, "A New Method for Obtaining Maximum Gain from Yagi Antennas," *IRE Trans. on Antennas and Propagation*, Vol. AP-7, pp. 379-386, October 1959.
- [20] D. L. Seugupta, "On the Phase Velocity of Wave Propagation Along an Infinite Yagi Structure," *IRE Trans. on Antennas and Propagation*, Vol. AP-7, pp. 234-239, July 1959.
- [21] \_\_\_\_\_, "On Uniform and Linearly Tapered Long Yagi Antennas," *IRE Trans. on Antennas and Propagation*,

- Vol. AP-8, pp. 11-17, January 1960.
- [22] F. Serracchioli and C. A. Levis, "The Calculated Phase Velocity of Long End-fire Uniform Dipole Arrays," IRE Trans. on Antennas and Propagation, Vol. AP-7, pp. S424-S434, July 1959.
- [23] J. Shefer, "Periodic Cylinder Arrays As Transmission Lines," IEEE Trans. on Microwave Theory and Techniques, Vol. MTT-11, pp. 55-61, January 1963.
- [24] R. J. Mailloux, "Antenna and Wave Theories of Infinite Yagi-Uda Arrays," IEEE Trans. on Antennas and Propagation, Vol. AP-13, pp. 499-506, July 1965.
- [25] \_\_\_\_\_, "Excitation of a Surface Wave Along an Infinite Yagi-Uda Array," IEEE Trans. on Antenna and Propagation, Vol. AP-13, pp. 719-724, September 1965.
- [26] \_\_\_\_\_, "The Long Yagi-Uda Array," IEEE Trans. on Antennas and Propagation, Vol. AP-14, pp. 128-137, March 1966.
- [27] E. R. Nagelberg and J. Shefer, "Dispersion Characteristics of an Array of Parasitic Linear Elements," IEEE Trans. on Microwave Theory and Techniques, Vol. MTT-14, pp. 391-396, August 1966.
- [28] G. A. Thiele, "Analysis of Yagi-Uda Type Antennas," IEEE Trans. on Antennas and Propagation, Vol. AP-17, pp. 24-31, January 1969.

- [29] L. C. Shen, "Possible New Applications of Periodic Linear Arrays," IEEE Trans. on Antennas and Propagation, Vol. AP-18, pp. 698-699, September 1970.
- [30] \_\_\_\_\_, "Numerical Analysis of Wave Propagation on a Periodic Linear Array," IEEE Trans. on Antennas and Propagation, Vol. AP-19, pp. 289-292, March 1971.
- [31] \_\_\_\_\_, "Characteristics of Propagating Waves on Yagi-Uda Structure," IEEE Trans. on Microwave Theory and Techniques, Vol. MTT-19, pp. 536-542, June 1971.
- [32] \_\_\_\_\_, "Directivity and Bandwidth of Single-band and Double-band Yagi Arrays," IEEE Trans. on Antennas and Propagation, Vol. AP-20, pp. 778-780, November 1972.
- [33] L. C. Shen, H. D. Cubley, and D. S. Eggers, "Measurement of the Propagating Waves on Yagi-Uda Array," IEEE Trans. on Antennas and Propagation, Vol. AP-19, pp. 776-779, November 1971.
- [34] K. Yoshimura and S. Tokumaru, "Calculated Phase Constant of Coupled Yagi Arrays," Electronics and Communication in Japan, Vol. 54-B, No. 10, pp. 94-100, October 1971.
- [35] D.P.S. Seth and Y. L. Chow, "On Linear Parasitic Array of Dipoles with Reactive Loading," IEEE Trans. on Antennas and Propagation, Vol. AP-21, pp. 286-292, May 1973.

- [36] D. Kajfez, "Nonlinear Optimization Reduces the Side-lobes of Yagi Antenna," IEEE Trans. on Antennas and Propagation, Vol. AP-21, pp. 714-715, September 1973.
- [37] \_\_\_\_\_, "Nonlinear Optimization Extends the Bandwidth of Yagi Antenna," IEEE Trans. on Antennas and Propagation, Vol. AP-23, pp. 287-289, March 1975.
- [38] D. K. Cheng and C. A. Chen, "Optimum Element Spacings for Yagi-Uda Arrays," IEEE Trans. on Antennas and Propagation, Vol. AP-21, pp. 615-623, September 1973.
- [39] \_\_\_\_\_, "Optimum Element Lengths for Yagi-Uda Arrays," IEEE Trans. on Antennas and Propagation, Vol. AP-23, pp. 8-15, January 1975.
- [40] M. Yamazawa, N. Inagaki, and T. Sekiguchi, "Excitation of Surface Wave on Circular-Loop Array," IEEE Trans. on Antennas and Propagation, Vol. AP-19, pp. 433-435, May 1971.
- [41] S. Ito, N. Inagaki, and T. Sekiguchi, "An Investigation of the Array of Circular-loop Antennas," IEEE Trans. on Antennas and Propagation, Vol. AP-19, pp. 469-476 July 1971.
- [42] J. Appel-Hansen, "The Loop Antenna With Director Arrays of Loops and Rods," IEEE Trans. on Antennas and Propagation, Vol. AP-20, pp. 516-517, July 1972.
- [43] L. C. Shen and G. W. Raffoul, "Optimum Design of

- Yagi Array of Loops," IEEE Trans. on Antennas and Propagation, Vol. AP-22, pp. 829-830, November 1974.
- [44] A. Shoamanesh and L. Shafai, "Resonance Effect in Arrays of Circular Loop Antennas," AP-S symposium, University of Illinois at Urbana, June 1975.
- [45] E. Ledinegg, W. Papousek, and H. L. Bruekmann, "Low-frequency Loop Antenna Arrays: Ground Reaction and Mutual Interaction," IEEE Trans. on Antennas and Propagation, Vol. AP-21, pp. 1-8, January 1973.
- [46] R. W. Burton and R.W.P. King, "An Experimental Investigation of Currents on a Yagi Array of Slot Antennas on Planar and Curved Surfaces," IEEE Trans. on Antennas and Propagation, Vol. AP-14, pp. 451-454, July 1966.
- [47] P. S. Bhatnagar, M. Chandhuri, S. P. Kosta, and A. Singh, "A Helical Infinite Yagi Structure," Proceedings of the IEEE, Vol. 59, pp. 289-291, February 1971.
- [48] W. L. Weeks, Antenna Engineering, New York; McGraw-Hill, 1968.
- [49] J. Shefer, "Plane Waves on a Periodic Structure of Circular Disks and Their Application to Surface-wave Antennas," IRE Trans. on Microwave Theory and Techniques, Vol. MTT-10, pp. 585-592, November 1962.

- [50] D. A. Watkins, *Topics in Electromagnetic Theory*, New York; John Wiley & Sons, 1958.
- [51] H. P. Hsu, *Fourier Analysis*, New York; Simon & Schuster, 1970.
- [52] I. S. Gradshteyn and I. M. Ryzhik, *Tables of Integrals, Series and Products*, New York; Academic Press, 1965.
- [53] A. Erdelyi, *Higher Transcendental Functions*, Vol. II, New York; McGraw Hill, 1953.
- [54] M. Abramowitz and I. A. Stegun, *Handbook of Mathematical Functions*, New York; Dover, 1965.
- [55] P. A. Kennedy, "Loop Antenna Measurements," *IRE Trans. on Antennas and Propagation*, Vol. AP-4, pp. 610-618, October 1956.
- [56] S. Ramo, J. R. Whinnery, and T. Van Duzer, *Fields and Waves in Communication Electronics*; John Wiley, & Sons, 1967.
- [57] J. D. Dyson, "Measurement of Near Fields of Antennas and Scatterers," *IEEE Trans. on Antennas and Propagation*, Vol. AP-21, pp. 446-460, July 1973.
- [58] E. K. Damon, "The Near Fields of Long End-fire Dipole Arrays," *IRE Trans. on Antennas and Propagation*, Vol. AP-10, pp. 511-523, September 1962.
- [59] L. Young, *Advances in Microwaves*, Vol. IV, New York; Academic Press, 1969.

- [60] Editor, "Open-ring Waveguide Holds Down Losses,"  
Electronic Design (International Report), Vol. 21,  
p. 100, October 1975.
- [61] K. Ayaki, "Spurious-mode Effects on Performance of  
the Helix-type Traveling-wave Amplifier," Electronics  
and Communications in Japan, Vol. 48, No. 5, pp. 54-60,  
May 1965.
- [62] R. M. Phillips, "High Power Ring-loop Traveling-wave  
Tubes for Advanced Radar," Microwave System News,  
pp. 47-49, February/March 1975.
- [63] C. K. Birdsall, and R. W. White, "Experiments with  
the Forbidden regions of Open Periodic Structures:  
Application to Absorptive Filters," IEEE Transactions  
on Microwave Theory and Techniques, Vol. MTT-12,  
pp. 197-202, March 1964.

## APPENDIX A

Consider the following recurrence relations for the modified Bessel functions [54]

$$I_{m-1} - I_{m+1} = \frac{2m}{x} I_m \quad (\text{A.1})$$

$$K_{m+1} - K_{m-1} = \frac{2m}{y} K_m \quad (\text{A.2})$$

$$I_{m-1} + I_{m+1} = 2I'_m \quad (\text{A.3})$$

$$K_{m-1} + K_{m+1} = -2K'_m \quad (\text{A.4})$$

where  $x$  and  $y$  are the arguments of the Bessel functions  $I$  and  $K$  respectively and their derivatives. Multiplying (A.1) times (A.2) and (A.3) times (A.4) and adding the results, yields

$$K_{m+1}I_{m+1} + K_{m-1}I_{m-1} = - \left( \frac{2m^2}{xy} I_m K_m + 2K'_m I'_m \right) \quad (\text{A.5})$$

## APPENDIX B

Reference [54] gives a series representation on page 498 for the Struve function  $S(x)$  with large argument, as

$$S(x) = I_0(x) - \Pi_0(x) = \frac{1}{\pi} \sum_{K=0}^{\infty} \frac{(-1)^K \Gamma(K+\frac{1}{2})}{\Gamma(\frac{1}{2}-K) (x/2)^{2K+1}} \quad (\text{B.1})$$

where

$I_0(x)$  is the modified Bessel function of zero order,

$\Pi_0(x)$  is the modified Struve function; and,

$\Gamma$  is the Gamma function.

Taking the leading term in the series of (B.1), an asymptotic expression for  $S(x)$  for large  $x$ , may be written as

$$S(x) \approx \frac{2}{\pi x} \quad (\text{B.2})$$

The same reference also lists on page 378 limiting values for products of modified Bessel functions as the argument becomes very large.

$$I_m(x) K_m(x) \approx \frac{1}{2x} \quad (\text{B.3a})$$

$$I'_m(x) K'_m(x) \approx -\frac{1}{2x} \quad (\text{B.3b})$$

Applying Equations (B.2) and (B.3) to the expression for  $a_n$  (Eq. 3.68a) and realizing that  $\gamma_n \approx \beta_n \approx 2n\pi/d$  for large index  $n$ , the expression for  $b_n$  results

$$b_n = \left[ \left( \frac{m}{Kb_1} \right)^2 - 1 \right] \frac{d^2}{8\pi^3 b_1 a_1} \left( \frac{1}{n^2} \right) \quad (\text{B.4})$$

Similarly, from the expression for  $c_n$  (Eq. 3.68b), the expression for  $d_n$  follows as

$$d_n = \left[ \left( \frac{m}{Kb_2} \right)^2 - 1 \right] \frac{d^2}{8\pi^3 b_2 a_2} \left( \frac{1}{n^2} \right) \quad (\text{B.5})$$

Finally, the series  $\sum_{n=1}^{\infty} b_n$  and  $\sum_{n=1}^{\infty} d_n$  are readily evaluated to yield

$$\sum_{n=1}^{\infty} b_n = \left[ \left( \frac{m}{Kb_1} \right)^2 - 1 \right] \frac{d^2}{48\pi b_1 a_1} \quad (\text{B.6})$$

$$\sum_{n=1}^{\infty} d_n = \left[ \left( \frac{m}{Kb_2} \right)^2 - 1 \right] \frac{d^2}{48\pi b_2 a_2} \quad (\text{B.7})$$

where  $\sum_{n=1}^{\infty} \left( 1/n^2 \right) = \pi^2/6$  has been used.

## APPENDIX C

In reference [54] page 377, the following asymptotic expressions for the modified Bessel functions of large arguments are found.

$$I_m(x) \approx \frac{e^x}{\sqrt{2\pi x}} \quad (\text{C.1a})$$

$$K_m(\alpha x) \approx \sqrt{\frac{\pi}{2\alpha x}} e^{-\alpha x} \quad (\text{C.1b})$$

$$I'_m(x) \approx \frac{e^x}{\sqrt{2\pi x}} \quad (\text{C.1c})$$

$$K'_m(\alpha x) \approx -\sqrt{\frac{\pi}{2\alpha x}} e^{-\alpha x} \quad (\text{C.1d})$$

Multiplying (C.1a) times (C.1b) and (C.1c) times (C.1d) yields

$$I_m(x) K_m(\alpha x) \approx \frac{e^{x(1-\alpha)}}{2x\sqrt{\alpha}} \quad (\text{C.2a})$$

$$I'_m(x) K'_m(\alpha x) \approx -\frac{e^{x(1-\alpha)}}{2x\sqrt{\alpha}} \quad (\text{C.2b})$$

Let  $h_n$  be the  $n$ th term in the series  $T_{12}$  given in equation 3.63c. Using (C.2) and the fact that  $\gamma_n \approx \beta_n \approx 2n\pi/d$  for large  $n$ , the asymptotic form of  $h_n$  follows as

$$h_n = \left[ \left( \frac{m}{Kb_0} \right)^2 - 1 \right] \frac{d}{4\pi b_1 \sqrt{\alpha}} \frac{e^{-(\alpha-1) \frac{2\pi b_1}{d} |n|}}{|n|} \quad (\text{C.3})$$

where  $\alpha = b_2/b_1 \geq 1$ . As seen from (C.3)  $h_n$  decays as  $e^{-Pn/n}$  for large  $n$  where  $P$  is a positive constant.

## APPENDIX D

The maximum error introduced in the expression for  $R_{n21}^2$  when the last term in (5.9) is neglected, is given by

$$e = \frac{2(a_1+a_2)S}{(b_2-b_1)^2 + (nd+S)^2} \quad (D.1)$$

Case 1:  $S \leq d-S$  or,  $S \leq d/2$

In this case, the error  $e$  has its largest value when  $n=0$ . That is,

$$e_{\max} = \frac{2(a_1+a_2)S}{(b_2-b_1)^2+S^2} \quad (D.2)$$

By differentiating  $e_{\max}$  with respect to  $S$ , and setting the result equal to zero, the value of  $S$  for which  $e_{\max}$  has its largest value is obtained. Namely,

$$S = (b_2-b_1) \quad (D.3)$$

Using (D.3) in (D.2), the largest possible value for  $e_{\max}$  results

$$\text{Max } \{e_{\max}\} = \frac{a_1+a_2}{b_2-b_1} \ll 1 \quad (D.4)$$

where one of the inequalities of equation (5.1?) has been used.

Case 2:  $S > d - S$  or,  $S > d/2$

Now the error  $e$  has its largest value when  $n = -1$ . That is,

$$e_{\max} = \frac{2(a_1 + a_2)S}{(b_2 - b_1)^2 + (S - d)^2} \quad (\text{D.5})$$

Since the derivative of  $e_{\max}$  with respect to  $S$  is positive,  $e_{\max}$  is an increasing function of  $S$ . Hence, it attains its largest value when  $S$  is equal to  $d$ . Then,

$$\text{Max } \{e_{\max}\} = \frac{2(a_1 + a_2)d}{(b_2 - b_1)^2} \quad (\text{D.6})$$

Since the maximum error in the first case (Eq. D.4) is negligible, and the one in the second case (Eq. D.6) is appreciable, it follows that the last term of equation (5.9) is insignificant, provided the following inequality holds.

$$0 \leq S \leq d/2 \quad (\text{D.7})$$